RICE UNIVERSITY

Mie and Finite-Element Simulations of the Optical and Plasmonic Properties of Micro- and Nanostructures

by

Ying Samuel Hu

A Thesis Submitted
in Partial Fulfillment of the
Requirements for the Degree

Doctor of Philosophy

Approved, Thesis Committee:

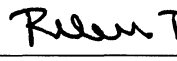

Rebekah A. Drezek, Chair
Professor of Bioengineering
Professor of Electrical and Computer Engineering

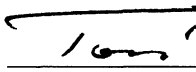

Tomasz S. Tkaczyk
Assistant Professor of Bioengineering
Assistant Professor of Electrical and Computer Engineering

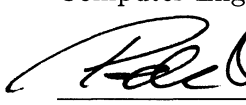

Peter J. Nordlander
Professor of Physics and Astronomy
Professor of Electrical and Computer Engineering

Houston, Texas

August, 2011

ABSTRACT

Mie and Finite-Element Simulations of the Optical and Plasmonic Properties of Micro- and Nanostructures

by

Ying Samuel Hu

A Mie-based code is developed for multilayer concentric spheres. The code is used in conjunction with a finite-element package to investigate the plasmonic and optical properties of micro- and nanostructures. For plasmonic nanostructures, gold-silica-gold multilayer nanoshells are computationally investigated. A plasmon hybridization theory is used to interpret the optical tunability. The interaction between the plasmon modes on the inner core and the outer shell results in dual resonances. The low-energy dipole mode is red-shifted by reducing the spacing (*i.e.*, the intermediate silica layer) between the core and the shell. This extra tunability allows the plasmon resonance of a multilayer nanoshell to be tuned to the near-infrared region from a visible silica-gold nanoshell whose gold shell cannot be further reduced in thickness. For multilayer nanoshells with reduced geometrical symmetry (*i.e.*, the inner core is offset from the center), modes of different orders interact. The mixed interaction introduces the dipolar (bright) characteristic into the higher-order (dark) modes and improves their coupling efficiency to the excitation light. The excitation of the dark modes attenuates and red-shifts the dipole mode and gives it higher-order characteristics.

For non-plasmonic structures, simulations have demonstrated that multilayered structures can either reduce or enhance the scattering of light. By adding an anti-

reflection layer to a microsphere made of a high-index material, the scattering force can be dramatically reduced. The reduced scattering allows optical trapping of high-index particles. Additionally, the improved trapping is not largely sensitive to the refractive index or the thickness of the coating. The technique has the practical potential to lower the requirement on the numerical aperture of the microscope objectives, making possible the integration of the imaging and optical trapping systems.

While the anti-reflection coating reduces scattering, the photothermal bubble (PTB) generated by gold nanoparticles by and large enhances the scattering of light. Transient PTBs are generated by super-heating gold nanoparticles with short laser pulses. Mie-based simulations predict that the scattering of PTBs strongly depends on the transient environment immediately surrounding the nanoparticles. A scattering enhancement of two-to-four orders of magnitude from PBT is demonstrated from both calculations and experiments.

Lastly, the near-field coupling between different plasmonic structures for surface-enhanced Raman scattering is investigated. A gold-coated silicon-germanium nanocone substrate has been fabricated and characterized. Finite-element simulations reveal that individual nanocones generate strong tip enhancement with axially polarized light (*i.e.*, light polarized along the vertical axis of the nanocone) while the enhancement from transversely polarized light (*i.e.*, light polarized in the plane of the substrate) is relatively weak. By simply filling the valleys between nanocones with plasmonic gold nanoparticles, the performance of the substrate is improved with in-plane excitation. Simulations reveal strong coupling between nanoparticles and adjacent nanocones with transverse exactions. An over one order-of-magnitude improvement has been experimentally observed.

Contents

Illustrations

Tables

Chapter 1

Research synopsis

The combination of nanotechnology and optical-based biomedical applications offers both non-invasitivity and targeting efficacy. Computational nanophotonics elucidate experimental observations as well as provide insight into the design of nanoparticles that may warrant novel biomedical applications. This thesis work focuses on the fundamental understanding of the interaction between light and structures of micro- and nanoscale in a broad range of applications. The work investigates different projects in which micro- and nanostructures can either enhance or diminish the scattering of light. Coupled with Mie and finite-element calculations, the study uses a plasmon hybridization theory to understand the plasmonic tunability of gold-based nanoparticles. Also investigated is inelastic scattering enhanced by the near-field enhancement of nanostructures.

First outlined is the main structure of the thesis. Mathematical details of the Mie theory for concentric multilayer spheres are presented in Appendix A. This Mie code is used to compute the optical properties of gold nanoparticles (AuNPs) and silica-gold core-shell nanoshells (AuNSs) in Chapter 2, concentric gold-silica-gold multilayer nanoshells (MNS) in Chapter 3, anti-reflection-coated spheres in Chapter 6 and photothermal bubbles (PTB) in Chapter 7. Synthesis of multilayer nanoshells is breifly outlined in Chapter 4. For calculating structures with asymmetric and non-spherical shapes, a finite-element simulation package COMSOL Multiphysics is used. Details of constructing geometries, calculating and post-processing results in COMSOL v3.5a

are presented in Appendix B. COMSOL is used compute the plasmonic properties of offset MNS in Chapter 5 and electromagnetic enhancement between nanocones and nanoparticles for surface-enhanced Raman scattering (SERS) in Chapter 8. The chapters are arranged in the order from the studies of plasmonic structures to non-plasmonic structures, and lastly to plasmonic structures again but for near-field properties.

While the topics cover a wide range of applications, these subjects complement each other in a few ways that consolidate our understanding of the interaction between light and micro- and nanostructures. First, both plasmonic and non-plasmonic structures are investigated. Plasmonic gold nanoparticles are perhaps the most investigated subjects in nanophotonics. Incident light excites surface plasmons that can alter the optical cross-sections of the nanoparticles. Here I investigate a more composite nanoshell structure in which a gold core is embedded into a silica-gold core-shell nanoshell, named multilayer nanoshell (MNS). Yet the structure of MNS is simple enough for us to understand new plasmonic properties as well as the effect from symmetry breaking using a plasmon hybridization theory. I take advantage of the convenient Mie code to also investigate non-plasmonic spherical structures with multiple layers. I show that by manipulating the coating of dielectric spheres, we can reduce scattering in optical trapping and enhance the trapping efficiency. I also show that secondary structures, such as photothermal bubbles (PTB) generated by plasmonic nanoparticles can dramatically enhance scattering. Here lies the second tie between the subjects in that I demonstrate manipulations of micro- and nanostructures that can either enhance or diminish the scattering of light. The PTB project directly compares the scattering efficiency between gold nanoparticles (plasmonic structures) and air bubbles (non-plasmonic structures). I realize that despite the benefit of plasmon

resonance of gold nanoparticles, their scattering efficiency trails air bubbles that are much larger in size. The third perspective is that I study both elastic and inelastic scattering. In elastic scattering, where the kinetic energy of the incident light is conserved, the scattered light is collected at the wavelength of the incident light. The energy conservation is assumed for all chapters except the last one. In the last chapter, I investigate the near-field coupling between plasmonic nanostructures for surface-enhanced Raman scattering.

This thesis work would not be made possible without the generous support from my thesis advisor Rebekah Drezek. The work is unique in a sense that it is a result of a wide range of collaborations with people from different departments at Rice University as well as different institutes. I would like to especially thank Peter Nordlander from the Physics Department at Rice for resourceful discussions on plasmon hybridizations, Timo Nieminen from the Physics Department at The University of Queensland for the didactic assistance on the Mie code, and Hyuck Choo at Lawrence Berkeley National Laboratory for both mentorship and friendship. I would like to thank Mary Ann Leung at Krell Institute for assistance on the DOE CSGF fellowship and practicums, Jim Schuck and Jeff Neaton for accommodating my first practicum at the Lawrence Berkeley National Laboratory, Dmitri Lapotko from Rice for the photothermal bubble project, Stuart Long and David Jackson from the University of Houston for continuous support of my professional development. I am fortunate to work with great colleagues at Rice, including Mark Knight in ECE, Seunghyun Lee in chemistry, Mark Pierce in BioE. Also many thanks to Venky Nammalvar, and other lab members that make progress with me every day: Lissett Bickford and Nastassja Lewinski. Last, I am deeply thankful to my parents for witnessing and sharing what I have achieved in my life.

Chapter 2

Plasmonic properties of gold nanoparticles and silica-gold core-shell nanoshells

Gold-based nanoparticles possess plasmonic properties due to surface plasmon resonances. Surface plasmon resonance is an oscillation of an incompressible electron gas on the interface between a metal and a dielectric material. For spherical gold nanoparticles (AuNPs), the electrons on the gold surface can be excited by light. The oscillation of the surface electrons alters the interference pattern of the scattered light and renders the optical cross-section of the nanoparticle several times larger than its physical cross-section. For silica-gold core-shell nanoshells (AuNSs), two surface plasmons can be excited: one on the interface between silica and gold, and the other on the interface between gold and the surrounding medium (*i.e.* water). The interaction between the two plasmon modes makes AuNSs tunable from visible to the near-infrared (NIR) region. The combined biocompatibility of gold and tunable plasmonic properties make AuNSs a popular candidate for contrast imaging agents and photothermal therapy agents [Hirsch et al., 2006, Gobin et al., 2007]. In this chapter, we will discuss the calculation of the optical properties of AuNPs and AuNSs using Mie theory. A plasmon hybridization theory will be introduced to understand the tunable optical properties.

2.1 Background on calculating the optical spectra

2.1.1 Extinction, scattering and absorption

The amount of optical energy being removed from the incident light by a gold nanoparticle is defined as its extinction property. Because light carries both energy and momentum (*i.e.* direction-dependent), the removal of the incident energy is carried in two ways: 1) conversion of the optical energy into energies of other forms, described by the absorption process, and 2) changing of direction of the incident light, described by the scattering process. Thus, extinction is a combination of absorption and scattering. To quantify these optical properties, extinction, absorption and scattering cross-sections are defined. The absorption cross-section, for instance, is defined as the ratio between the absorbed power by the nanoparticle and the incident light intensity. The scattering cross-section, similarly, is defined as the ratio between the scattered power by the nanoparticle and the incident light intensity. For spherical particles, the scattering and extinction cross-sections can be directly calculated from Mie coefficients. The absorption cross-section is calculated by subtracting the scattering cross-section from the extinction cross-section. Normalized efficiencies, such as extinction, absorption and scattering efficiencies, are calculated as the ratio between the corresponding optical cross-section and the particle's physical cross-section. For more details, refer to Section(A.2).

It should be noted that the extinction cross-section of non-absorbing dielectric particles converges to two instead of unity as the size of the particle becomes larger compared to the wavelength (See Figures A.1 and A.2). This is due to the wave-particle duality of light, known as the extinction paradox. Briefly, both deflection and diffraction contribute to the process of removing energy from the incident light,

resulting in a total removal of twice the amount of energy as in the incident light.

2.1.2 The dielectric function of gold

Nobel metals, such as gold and silver, have dielectric properties that depend on excitation energy. This dependency is characterized by the dielectric function for the bulk material. Interestingly, gold and silver behave more like dielectric materials rather than metals (*i.e.* good electric conductors) at optical frequencies. A classical Drude-Lorentz model can be used to describe the dielectric function of gold (extensive discussions on Drude model can be found in Chapter 2 in Kreibig & Vollmer's book [Kreibig & Vollmer, 1995]). The model contains Drude terms and a summation of Lorentzian terms. The Drude terms describe the free-electron response of the metal that can be characterized by the Drude plasma frequency (ω_p) and a relaxation constant (Γ) that depends on Fermi velocity (v_F) and mean free path of the electron (l). The summation of the Lorentzian terms describes the optical response when interband transitions come into play [Kreibig & Vollmer, 1995]. For gold, this region is above 1.9 eV [Hao & Nordlander, 2007] or below 650 nm. For time-domain computational methods, such as finite-difference time-domain (FDTD) method, the Drude-Lorentz model is important because it provides an analytical form of the dielectric function, which can be transformed into the time domain for simulating realistic materials [Hao & Nordlander, 2007]. For frequency-domain computational methods, such as finite-element method (FEM) and analytical Mie-based theory, an interpolation of the experimental measurements is sufficient.

Almost ubiquitously used for simulating gold nanostructures is the dielectric function obtained from thin-film measurements reported by Johnson and Christy [Johnson & Christy, 1972]. It should be noted that deviations exist between different reports.

Figure 2.1 compares the refractive index r_n of gold from two sources (with the Johnson and Christy date in hollow circles and Lynch and Hunter data [Lynch & Hunter, 1985] in solid circles). For non-magnetic metal, such as gold, the refractive index r_n is related to the dielectric constant ϵ_n by $r_n^2 = \epsilon_n$.

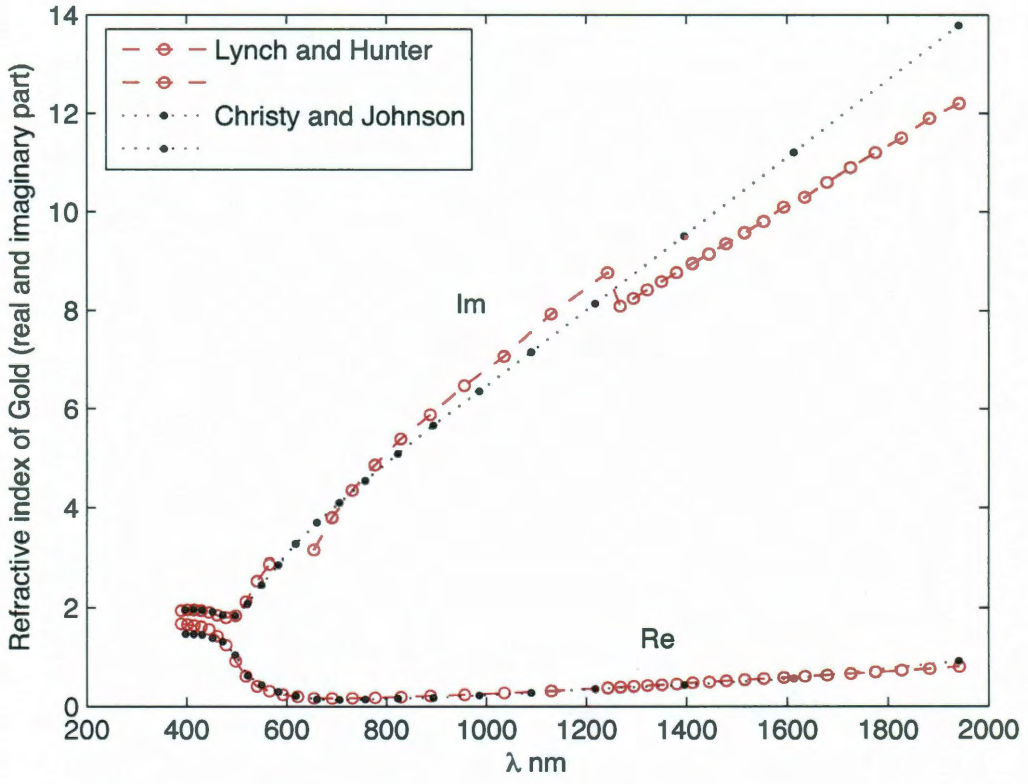

Figure 2.1 : Comparison of the real and imaginary part of the refractive index of gold from Lynch & Hunter (LH) [Lynch & Hunter, 1985] and Johnson & Christy (JC) [Johnson & Christy, 1972].

It can be observed that the major discrepancy comes from the imaginary part. The JC data are continuous whereas the LH data have a discontinuity at ~1300 nm. At wavelengths shorter 1300 nm, the LH data tend to fluctuate around the JC data. The calculated optical spectra of gold nanoparticles are highly sensitive to the values

of the dielectric constants. In addition, the imaginary part of the dielectric function influences the damping of the plasmon resonance. In this thesis work, gold properties from JC are exclusively used.

Intrinsic size effect

It is worth noting that the dielectric function of gold also becomes size dependent when the nanoparticle is smaller than the electron mean free path in the bulk material. Confined electrons impinge upon the surface of the nanoparticle before they traverse the distance of a mean free path (a phenomenon known as surface scattering). An empirical approach replaces the electron mean free path (l) in the Drude model with the limiting dimension of the gold nanoparticle. For instance, for spherical gold nanoparticles, the effective mean free path becomes the diameter of the sphere; and for silica-gold core-shell nanoshells, the effective mean free path is the thickness of the gold shell. Although which number to use and when to use size-corections is highly controversial [Averitt et al., 1997, Khlebtsov et al., 2007, Nehl et al., 2004], the general effect from surface scattering of electrons is a smearing out of the spectrum, as shown in Figure 2.2 for an R40/45 nm (inner/outer radius) core-shell nanoshell. In this thesis work, unless otherwise noted, the intrinsic size effect is not considered.

2.2 Absorption *vs.* scattering

For a nanoparticle in the Rayleigh region (*i.e.* the diameter of the particle $d \ll$ the wavelength λ), the amount of light being absorbed is proportional to the volume of the particle, and thus d^3 for a spherical particle with a diameter of d [van Dijk et al., 2006]. According to Rayleigh scattering for small particles, the scattering intensity is

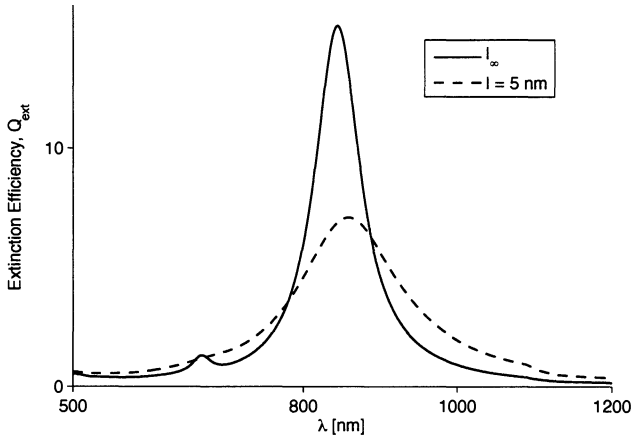

Figure 2.2 : Mie calculation on R40/45 nm nanoshell spectrum using bulk gold properties (l_∞) and size-corrected properties (l = 5 nm).

proportional to d^6/λ^4 [van Dijk et al., 2006]. Thus, we have a simple relationship:

$$abs \propto d^3 \tag{2.1}$$

$$sca \propto d^6. \tag{2.2}$$

When a particle is relatively large (*i.e.*, >100 nm), the scattering efficiency is much stronger than the absorption efficiency. When the particle becomes smaller, the scattering loses its strength much more quickly than absorption, rendering the particle absorption-dominant. Figure 2.3 displays the absorption, scattering, and extinction spectra of 80, 60, and 20 nm gold nanoparticles (AuNPs). Besides the plasmon resonance at around 520 nm, one can observe that the particle gradually becomes absorption-dominant when it becomes smaller. The same trend applied to gold nanoshells (AuNSs).

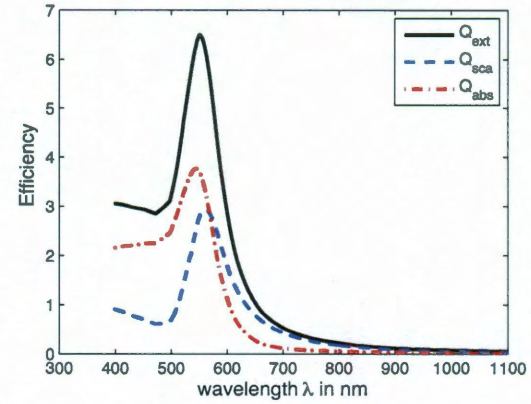

(a)

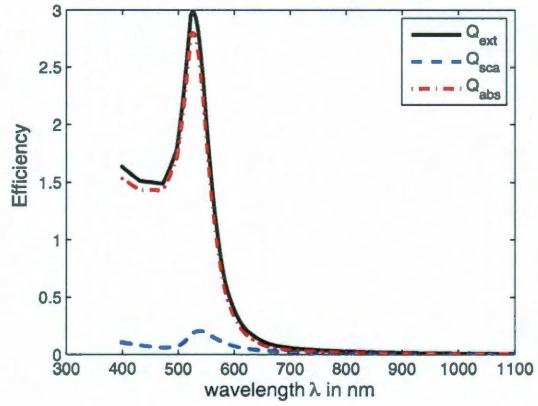

(b)

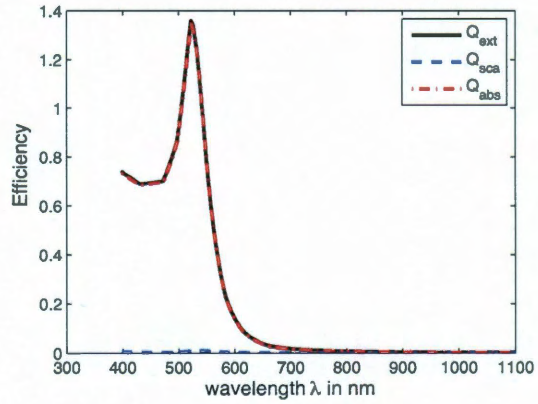

(c)

Figure 2.3 : Extinction efficiency Q_{ext}, absorption efficiency Q_{abs} and scattering efficiency Q_{sca} spectra for gold colloid with (a) d=80nm, (b) d=40nm, and (c) d=20nm. The surrounding medium is water (r_n=1.33).

2.3 Optical tunability of silica-gold core-shell nanoshells

Silica-gold core-shell nanoshells have plasmonic tunability due to the interaction between two surface plasmons. Shown in Figure 2.4 is a plasmon hybridization diagram for the nanoshell. There are two surface plasmon modes on the nanoshell: the sphere mode is the surface plasmon on the interface between the gold shell and the surrounding medium; and the cavity mode is the surface plasmon on the interface between the gold shell and the dielectric core. The interaction between the two modes results in a split of the two modes: a high-energy anti-bonding mode and a low-energy bonding mode. In the bonding mode, the polarizations of the sphere mode and cavity mode are aligned (symmetric); whereas in the anti-bonding mode, the polarizations are opposite to each other (anti-symmetric). Because the amplitude of the resonant peak is proportional to the square of the polarizability of the entire particle, the bonding mode is strongly excited. This is also the mode observed in the vis-NIR spectrum. The anti-bonding mode, in contrast, is highly damped and smeared out by the inter-band transition of electrons.

The strength of interaction between the two modes is determined by their physical separation, namely the thickness of the gold shell. A thinner shell results in greater interaction and further splits out the bonding and anti-bonding mode. This stronger interaction causes a red-shift of the bonding mode (*i.e.* down-shift in energy). Figure 2.3 shows the spectra for nanoshells (NS) with the same outer radius (70 nm) and different thicknesses of the gold layer. A red-shift of the resonant peak (bonding mode) can be observed when the thickness decreases.

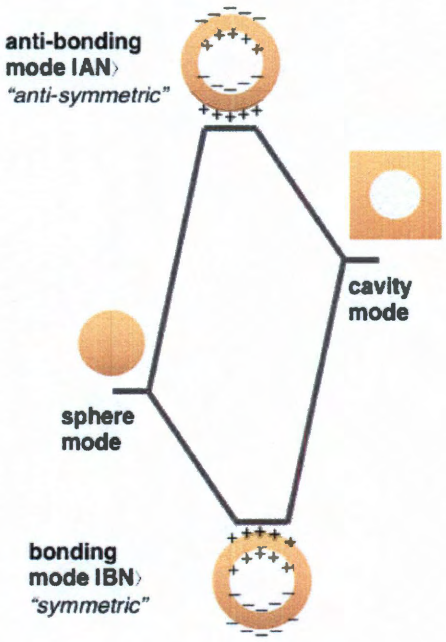

Figure 2.4 : A plasmon hybridization model for core-shell nanoshells. Adapted from [Radloff, 2003].

2.4 Calculations *vs.* experimental measurements

Synthesis of silica-gold nanoshells is described elsewhere in the literature [Oldenburg et al., 1998]. Figure 2.6 shows a transmission electron microscopy (TEM) image of 361-nm nanoshells with NIR resonance. A distribution of the silica-core radius and outer radius can be observed using scanning electron microscopy (SEM) or TEM. The measured spectrum from an ensemble of nanoshells dispersed in water resembles an average of spectra from all nanoshells with different dimensions. In Figure 2.3(a), I superimpose 41 spectra with 10% standard deviation in the size of the silica core for an $R127/142$ nm nanoshell. One can observe a broadening of the dipole resonance at ~800 nm and the smearing out of the quadrupole resonance a ~660 nm. This averaging effect from size dispersion masks the broadening from intrinsic effect of

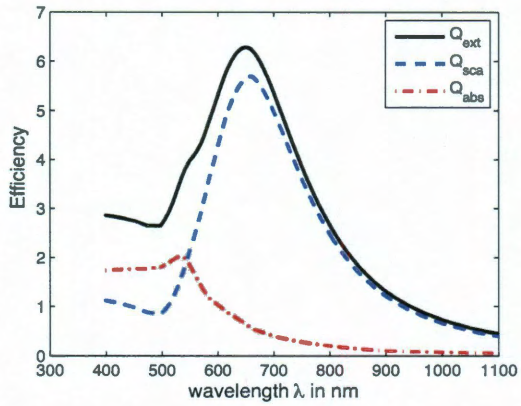

(a)

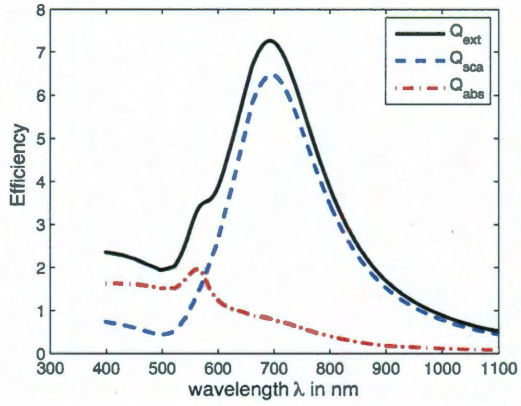

(b)

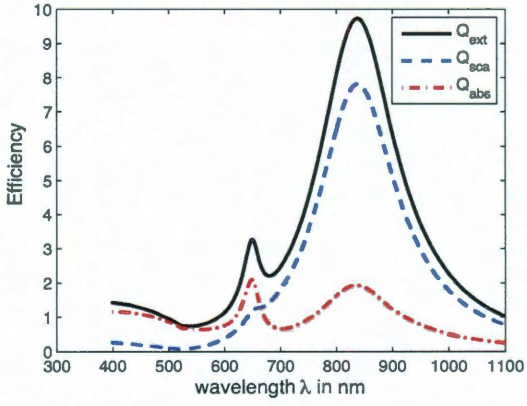

(c)

Figure 2.5 : Optical spectra of gold nanoshells with (a) R=40/70nm, (b) R=50/70nm, and (c) R=60/70nm.The surrounding medium is water (r_n=1.33).

gold (i.e. Figure 2.2). Figure 2.3(b) shows a good agreement between measured spectrum and superimposed spectrum and a good agreement is observed [Bickford et al., 2008b, Hu et al., 2008b]. Both spectra are normalized with respect to the peak value at the dipole resonance. A better fit is expected when the standard deviation in the thickness of the gold shell is also considered.

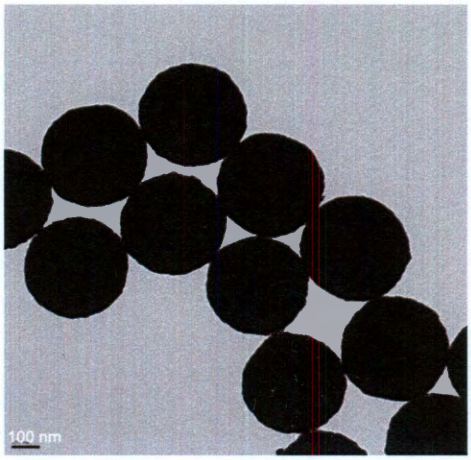

Figure 2.6 : Transmission electron microscopy image of the nanoshells with an average diameter of 361 nm. Scale bar is 100 nm.

2.5 Summary

To sum up, in this chapter, the dielectric function of gold and theoretical concerns regarding surface scattering of electrons are discussed. A rule-of-thumb relationship for the scattering *vs.* absorption ratio with respect to the size of the nanoparticle is outlined. Also shown are calculation results for silica-gold nanoshells and explained their optical tunability using a plasmon hybridization model. Lastly, good agreements between calculations using superposition and experimental measurements have been demonstrated.

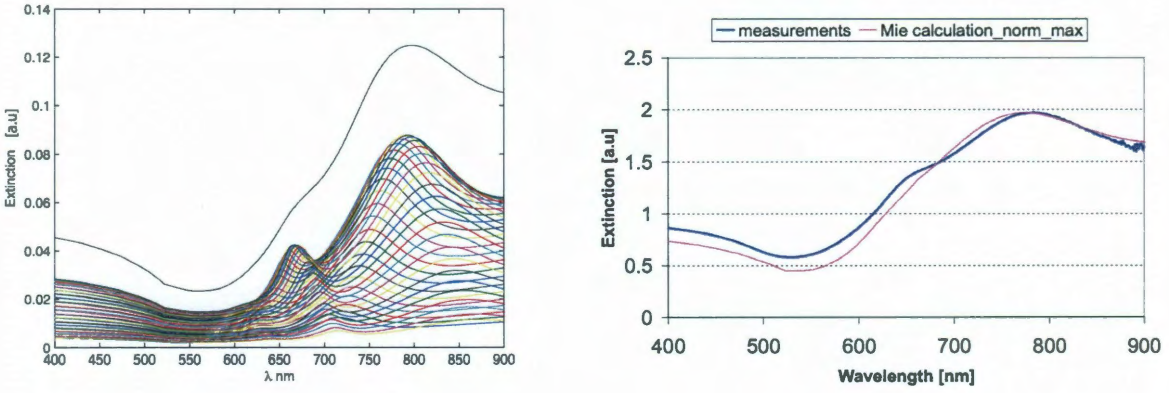

(a) (b)

Figure 2.7 : Mie calculations a) with superposition, b) compared to experimental measurements [Bickford et al., 2008b, Hu et al., 2008b].

Chapter 3

Plasmonic properties of concentric gold-silica-gold multilayer nanoshells *

In this chapter, the spectral and angular radiation properties of gold-silica-gold multilayer nanoshells are investigated using Mie theory for concentric multilayer spheres. The spectral tunability of multilayer nanoshells is explained and characterized by a plasmon hybridization model and a universal scaling principle. A thinner intermediate silica layer, scaled by the size of the particle, red shifts the plasmon resonance. This shift is relatively insensitive to the overall particle size and follows a universal scaling principle with respect to the resonant wavelength of a conventional silica-gold core-shell nanoshell. The extra tunability provided by the inner core further shifts the extinction peak to longer wavelengths, which is difficult to achieve on sub-100 nm silica-gold nanoshells due to the limitations on synthesis of ultrathin gold coatings. Multilayer nanoshells are found to be more absorbing with a larger gold core, a thinner silica layer, and a thinner outer gold shell. Both scattering intensity and angular radiation pattern are found to differ from conventional nanoshells due to spectral modulation from the inner core. Multilayer nanoshells may provide more backscattering at wavelengths where silica-gold core-shell nanoshells predominantly forward scatter.

---

*Adapted from Y. Hu, R. C. Fleming, and R. A. Drezek, Optical properties of gold-silica-gold multilayer nanoshells, *Opt. Express*, **16**(24), 19579-19591, 2008.

3.1 Background on multilayer nanoshells

The human use of gold has been well documented throughout history. Observations have been long made on the unique optical properties of nano-sized particles composed of gold. The rapid development in controlled chemical synthesis and computational modeling has generated an extensive exploration on various gold-related nanostructures, ranging from nanorods [Gulati et al., 2006] and nanostars [Nehl et al., 2006, Hao et al., 2007], to core-shell nanoshells [Averitt et al., 1997, Averitt et al., 1999, Hirsch et al., 2006], nanorice [Wang et al., 2006a], and nanocages [Cang et al., 2005]. Silica-gold core-shell nanoshells have attracted particularly significant research attention due to agile optical tunabilities [Averitt et al., 1997, Prodan & Nordlander, 2003] and absorption and scattering cross sections which can greatly exceed those of organic dyes [Landsman et al., 1976, Loo et al., 2005]. Superior photochemical stability in combination with excellent biocompatibility renders gold nanoshells highly attractive for biomedical imaging and spectroscopy applications, such as optical coherence tomography [Lin et al., 2005a], reflectance spectroscopy [Nammalvar et al., 2007], dark-field and two photon microscopy [Loo et al., 2005, Park et al., 2008, Bickford et al., 2008a]. Gold nanoshells have also been investigated for photothermal therapy and controlled drug release [Lowery et al., 2006b, Bikram et al., 2007].

Extinction spectra of the core-shell nanoshell can be tuned by varying the gold-shell thickness scaled by particle size. The plasmon resonance of gold nanoshells is related to the interaction between plasmons supported on the inner and outer surface of the gold shell. The strength of their interaction is determined by the shell thickness scaled by particle size. As the gold shell decreases in thickness, a stronger plasmon interaction red shifts the resonance peak compared to that of a solid gold particle. This allows the tuning of nanoshell plasmon resonances into the

near-infrared (NIR) region [Oldenburg et al., 1999] where main biological absorption is minimal [Weissleder, 2001]. The universal dependence of red shifts upon shell thicknesses scaled by particle size was reported by Jain *et al* [Jain & El-Sayed, 2007].

Here I examine the optical properties of gold-silica-gold multilayer nanoshells. Figure 3.1. illustrates the structure of multilayer nanoshells and silica-gold core-shell nanoshells. Xia *et al.* were the first to report the synthesis of ~50 nm multilayer nanoshells that may exhibit NIR absorption peaks [Xia et al., 2006]. Coating gold colloid with a thin layer of silica was achieved by a modified Stöber method in which silica growth was preceded by a sodium silicate (active silica) treatment in an aqueous solution with a controlled pH. The outer gold coating was produced similarly to the way conventional nanoshells are made. Due to the use of small gold colloids (~20 nm) and the relative ease of silica coating with various thicknesses, sub-100 nm multilayer nanoshells can be synthesized. While comparable in size with some solid gold spheres, a greater spectral tunability is expected for multilayer nanoshells due to the interaction of plasmons on interfaces between gold and dielectrics. Such nanoshells could also offer a smaller profile than their conventional counterparts, thus provide better vascular permeability and more efficient antibody conjugation owing to the larger surface-to-volume ratio [Xia et al., 2006].

Thus far, the optical properties of the multilayer nanoshell, composed of a metallic core and two alternating dielectric and metallic layers, have been investigated by Chen *et al.* to achieve ultrasharp resonant peaks across the spectrum for multiplexing applications [Chen et al., 2005b]. In the study, the overall diameter of the nanoshell was kept at 10 nm and the layers were tailored with subnanometer precision. The thin layers sparked some controversy over spectral broadening due to the intrinsic size effect on metal properties for nano-sized particle simulations [Khlebtsov & Khlebtsov,

2006].

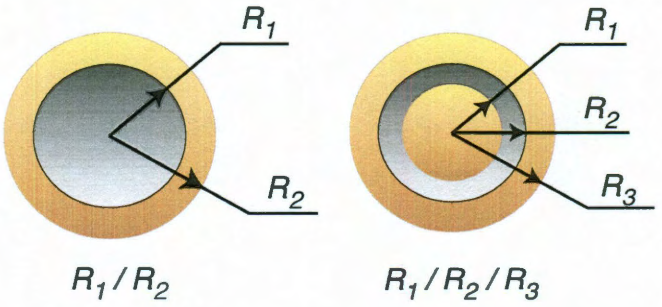

(a) Conventional nanoshell (CNS) (b) Multilayer nanoshell (MNS)

Figure 3.1 : Geometries of (a) silica-gold core-shell conventional nanoshells, and (b) gold-silica-gold multilayer nanoshells.

The goal of this paper is to examine the spectral and angular scattering properties of gold-silica-gold multilayer nanoshells in the size region where successful particle syntheses have been reported and can be achieved based on currently available protocols [Xia et al., 2006, LizMarzan et al., 1996]. The study is based on what has been done on conventional nanoshells, with the objectives of unveiling and understanding the similar and distinct optical properties of multilayer nanoshells, as well as investigating their potential for bioimaging applications.

3.2 Methodology

A Mie-based computation code has been developed to calculate light scattering from concentric spheres [Hu et al., 2008c, Bohren & Huffman, 1983, van de Hulst, 1981]. Boundary conditions at each inter-layer interface are expressed in term of vector spherical wave functions and unknown field coefficients. The tangential electric and magnetic fields are stored as alternating rows for each interface in a square matrix and

the vector of unknown coefficients is resolved by a matrix division. This approach has a substantial computational advantage as it can handle subjects from spheres with stratification to spheres with gradient index profiles. Extinction, scattering and absorption coefficients were calculated based on Mie scattering coefficients obtained from the Mie code. Angular radiation was calculated for unpolarized light using the approach outlined by van de Hulst [van de Hulst, 1981]. Details of the code can be found in [Hu et al., 2008c] and Appendix A.

In this study, plane-wave expansion coefficients are used for illumination. This assumes that particles are located far enough from the light source or that the particles are significantly smaller than the incident beam profile. Other assumptions include that the particles are rigidly spherical and the layers are concentric. It is to be noted that various factors, such as surface topology [Wang et al., 2006c], core eccentricity [Wang et al., 2006] and interparticle distance [Lassiter et al., 2008b] have been reported to affect the nanoshell spectra to various degrees.

For gold properties, data from Cristy and Johnson [Johnson & Christy, 1972] are adapted for the simulation. While the spectral broadening effect from surface scattering in nano-sized particles has been proposed and observed on gold colloids [Kreibig & Vollmer, 1995, Berciaud et al., 2005a], the current literature on intrinsic effects of the core-shell nanoshells has not been able to reach a consensus. Common practice at times adds an additional term to the bulk material dielectric constant to acount for the limited free electron path imposed by the thin gold shell [Averitt et al., 1997]. Others propose that this modification is determined by the core radius to shell thickness ratio [Khlebtsov et al., 2007]. However, it was reported that intrinsic effects were not observed on spectral measurement of single silica-gold nanoshells [Nehl et al., 2004]. In light of controversies over this issue, intrinsic size corrections were not

considered in this study. In addition, I attempt to construct gold layer geometries outside the region where intrinsic effects prevail.

In simulations presented, water is the surrounding medium unless otherwise noted. The dielectric constant for silica was set to 2.04 and that for water was 1.77. The Mie code was validated against published spectral results for gold particles [Jain et al., 2006], silica-gold nanoshells [Jain et al., 2006], and gold-silica-gold-silica nanoshells [Prodan et al., 2003b], as well as angular radiation patterns of silica-gold nanoshells [Fu et al., 2007].

3.3 Spectral properties

3.3.1 Tunability from the inner gold core

In this section, effects from the inner gold core are qualitatively explained by a plasmon hybridization model and quantitatively examined using Mie theory. The goal is to explore the possibilities of synthesizing multilayer nanoshells with enhanced optical properties in the NIR region.

Similar to conventional nanoshells (CNS), multilayer nanoshells (MNS) have tunable optical properties, as explained by a plasmon hybridization theory [Prodan et al., 2003b]. Briefly stated, the tunability of a CNS is attributed to the interaction between plasmons that reside on the outer and inner surface of the gold shell, also known as the sphere and cavity plasmon, shown in the left panel of Figure 3.2. The interaction causes the plasmon to split into a low-energy bonding mode and a high-energy anti-bonding mode. The bonding mode is often visualized by the surface plasmon resonance peak of the nanoshell in the vis-NIR region as in this configuration the polarizations of the cavity and sphere modes are aligned. The anti-bonding mode,

in contrast, has oppositely aligned polarizations and thus mode is heavily damped. The bonding mode can be tuned by varying the ratio of shell thickness to core radius, which essentially tunes the coupling strength between the two plasmons.

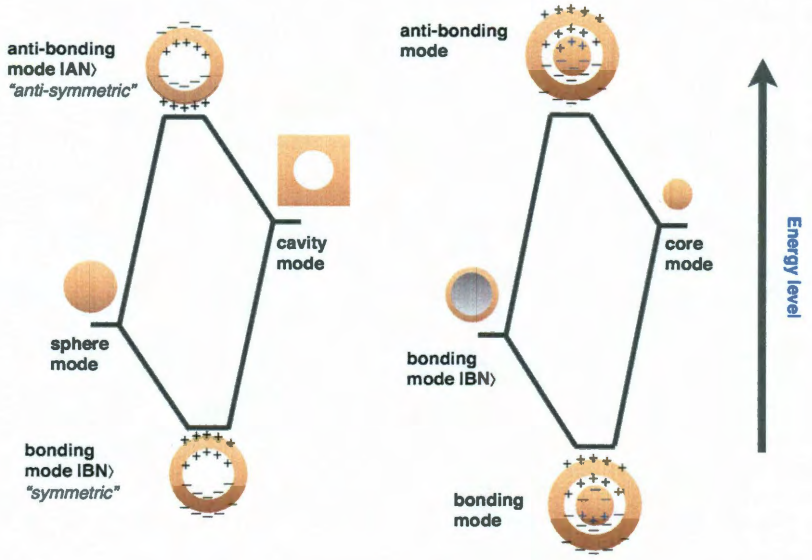

Figure 3.2 : Plasmon hybridization for CNS (left) and MNS(right).

In contrast to CNS, MNS have an extra degree of tunability from the inner gold core. This optical tunability can be understood as an interaction between the CNS bonding mode $|BN\rangle$ and the gold core sphere mode $|rC\rangle$. The interaction results in an anti-symmetric anti-bonding mode and a symmetric bonding mode. The thickness of the intermediate silica layer determines the strength of interaction. An increase in the inner gold core radius on an otherwise fixed geometry will decrease the intermediate silica layer thickness and increase the plasmon interaction. This is accompanied by a red shift of the spectrum that is in agreement with Mie calculation results, shown in Figure 3.3.

The extra tunability introduced by the inner gold core facilitates the synthesis of

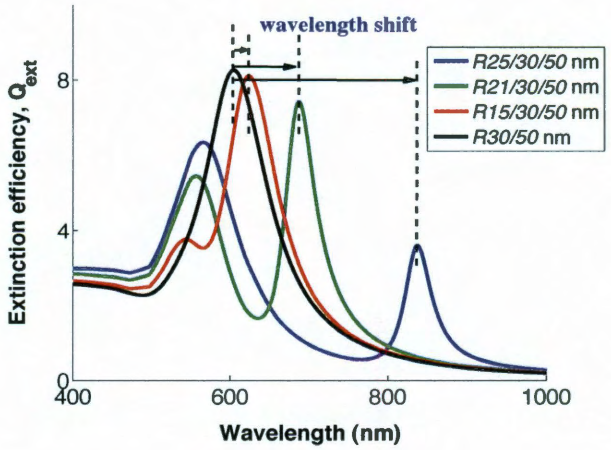

Figure 3.3 : Calculated spectra of CNS and MNS with various inner core radii while the silica and outer radius remain the same. The red shift of MNS from CNS is indicated by lambda shift.

small MNS with NIR extinction peaks. This is not an option for CNS. Near-infrared extinction is difficult to achieve on small CNS because extremely thin outer gold layers are required. The current coating process involves functionalizing the silica core surface with amine groups, then attaching small gold colloids (1–2 nm in size) to form nucleation sites for further reduction of gold to form a continuous layer [Hirsch et al., 2006]. However, for sub-10 nm coats, it is often difficult to achieve even layers and smooth surfaces, both of which are needed to avoid drastic deterioration in the overall integrity of the nanoshell spectrum [Wang et al., 2006c, Wang et al., 2006]. For MNS, these requirements are alleviated because extinction peaks can be further red shifted by having a larger inner gold core with a thin surrounding silica layer. The compromise is a damped peak owing to the increasing plasmon strength associated with the gold core mode $|rC\rangle$.

3.3.2 Universal scaling principle

Given that the plasmon coupling strength is qualitatively determined by the intermediate silica layer thickness, a quantitative analysis is desired to characterize the spectrum signature of MNS with various dimensions. Among recently reported observations is the universal scaling principle, which was first reported for metal particle pairs in which plasmon resonance is red shifted from that of an isolated metal sphere by moving the two particles closer together [Jain et al., 2007]. The shift exhibits a near-exponential decay with increasing interparticle distance. Jain et al. extended this theory to CNS where the gold shell thickness, scaled by particle size, is analogous to the interparticle gap and the two interacting plasmon modes act as a particle pair [Jain & El-Sayed, 2007]. A similar exponential decay is observed independent of the overall nanoshell dimension. While MNS support more than two plasmons, their plasmon resonance is mainly determined by the interaction between the bonding mode of CNS and the sphere mode of the gold core. The CNS anti-bonding mode, however, has a very small dipole moment because the cavity plasmon is oppositely aligned with the sphere mode. For this reason, the CNS anti-bonding mode interaction with the core mode is small and becomes too damped to be visible in the spectra. The coupling strength between the two major-playing modes is determined by the intermediate silica layer thickness, scaled by the overall particle size. With R_2/R_3 ratio kept constant, a universal decaying curve is observed for MNS of different dimensions.

Figure [?] illustrates an exponential decay insensitive to the overall particle size at a constant ratio of $R_2/R_3 = 0.6$. Results (data not shown) indicate that both the R_2/R_3 ratio and the surrounding medium affect the rate of decay. In addition, larger MNS were found to retain the same exponential decay but at slightly different

rates. This can be partially attributed to the fact that multiple resonant peaks start to emerge with broad widths and less well-defined shapes. Nevertheless, the universal scaling principle demonstrates that CNS plasmon resonant peaks can be further red shifted on MNS by reducing the silica layer thickness. For particles retaining their overall dimension and outer shell thickness, this translates to the use of large gold cores with thin silica coatings.

It is worth noting that when t is pushed to the zero limit where $R_1 = R_2$, thus the silica layer thickness approaches zero, the plasmon mode red shifts to zero energy. However, the spectral weight becomes negligible due to the cancellation of the dipole moments of the core and of the shell.

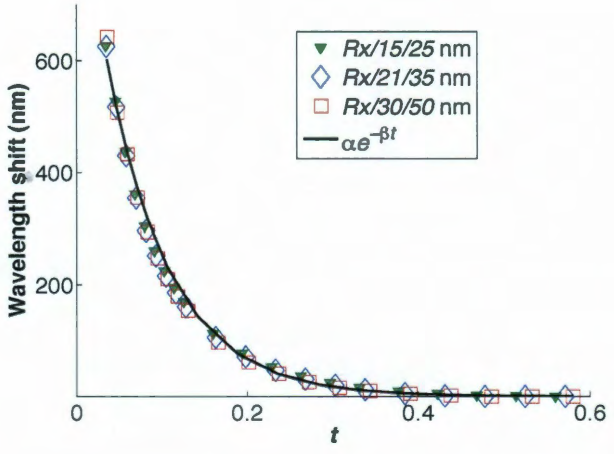

Figure 3.4 : Mie calculation results for wavelength shifts from the MNS $(R_1/R_2/R_3)$ vis-NIR plasmon resonance peak relative to that of CNS (R_2/R_3) with the same silica and outer gold radius versus intermediate silica thickness scaled by particle size of MNS. $t = (R_2 - R_1)/R_3$, $\alpha = 972.43$, $\beta = 13.48$.

3.3.3 Sensitivity to the surrounding medium

The plasmon hybridization model can be used to explain the spectral sensitivity of MNS to the surrounding medium. MNS plasmons are resulted from the hybridization

between CNS bonding modes $|BN\rangle$ and gold core sphere modes $|rC\rangle$, and since $|rC\rangle$ is not in direct contact with the outside, $|BN\rangle$ is the mode mainly affected by the surrounding medium. For instance, an increase in the refrative index of the medium does not directly affect $|rC\rangle$ but red shift $|BN\rangle$, contributing to an overall red shift as demonstrated in Figure 3.3.3. This suggests that MNS may be used as sensors in various sensing applications based on detecting localized surface plasmon resonances (LSPRs).

While CNS and other nanostructure have been studied for sensing applications [Wang et al., 2008, Larsson et al., 2007], MNS may offer some unique opportunities given multiple extinction peaks shifted in a synchronous fashion when the surrounding medium is perturbed. Moreover, the degree of shift of each peak was found to be particle-dependent. Table 3.1 tabulates the wavelength shift for two MNS with an identical size and gold shell thickness. Between the two, MNS2 bears a stronger plasmonic coupling between $|BN\rangle$ and $|rC\rangle$ than MNS1. It can be seen that MNS2 has a larger peak shift at the shorter wavelength and its inter-peak distance decreases with increasing medium indices. The opposite was found for MNS1. Also observed is that the shift of each peak of the MNS approximately adds up to that of the single SPR on an equivalent CNS.

3.3.4 Tunability on scattering and absorption

Rayleigh criteria state that, for particles much smaller than the wavelength, the scattering intensity is proportional to R^6, where R is the particle radius [van Dijk et al., 2006]. However, absorption depends on particle volume, which is proportional to R^3 for a sphere. The higher order dependence on particle size makes scattering more sensitive to size variations than absorption. For instance, at 532 nm, 100 nm solid

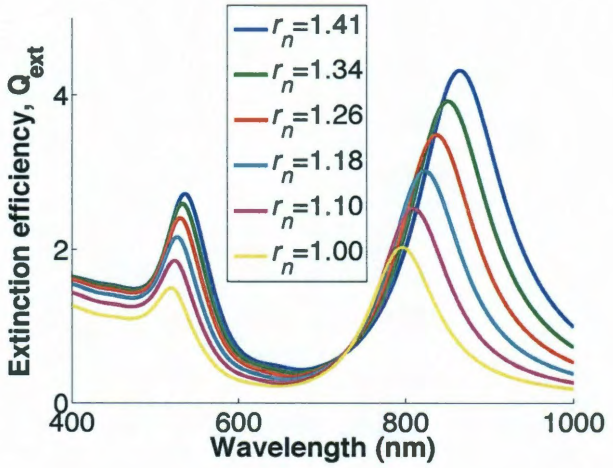

Figure 3.5 : Calculated extinction spectra of $R20/30/35$ nm MNS immersed in various media with distinct refractive indices.

gold spheres have approximately the same absorption and scattering cross sections in water [van Dijk et al., 2006]. Scattering attenuates more drastically than absorption when particle size decreases, rendering gold colloids absorption-dominant. In contrast, increasing particle size enhances scattering much faster than absorption; thus, large particles are mainly scattering-based. For inhomogeneous spheres, such as silica-gold core-shell CNS, it has been demonstrated that the scattering-to-absorption ratio rises with increasing core size or outer shell thickness or both [Lin et al., 2005a]. These observations provide very useful guidelines for synthesizing particles to match either scattering- or absorption-based applications at desired wavelengths [Lowery et al., 2006b, Agrawal et al., 2006].

The scattering and absorption behavior of concentric multilayer spheres can be studied similarly as functions of layer thickness to obtain insight into how changes in each layer affect the overall scattering and absorption. Due to the complexity in displaying results with concurrent variation in each of the three layers, simulations were adapted to geometries in which two layer thicknesses were changed while the

Table 3.1 : Surface plasmon resonance peak shift of $R20/35/50$ nm (MNS1), $R30/35/50$ nm (MNS2), and $R35/50$ nm (CNS) in different dielectric media ($\lambda_{p2} > \lambda_{p1}$).

	p1 shift (nm)		p2 shift (nm)		p2-p1 (nm)		p shift (nm)
refractive index	MNS1	MNS2	MNS1	MNS2	MNS1	MNS2	CNS
1.0	0	0	0	0	110	424	0
1.1	5	8	10	4	115	420	15
1.2	11	20	22	9	121	413	33
1.3	16	37	38	15	132	402	56
1.4	21	53	56	22	145	393	80
1.5	27	68	77	29	160	385	105

third layer remained fixed. Three sets of runs were performed with three combinations of the two variable-layer thicknesses. At each dimension, the extinction, scattering, and absorption spectra were calculated from 400 to 1941 nm. Two plasmon resonance wavelengths λ_{max} were chosen at the extinction maxima. The scattering to extinction ratio was calculated at the longer of the two; the one associated with the MNS mode rather than the gold sphere mode. If only one maximum occurred in the wavelength range, then the calculation was performed at that wavelength. Since the resulting plots illustrate the scattering ratio at the longer plasmon resonant wavelengths, we expect the magnitude of the extinction peak to attenuate as it red shifts and it may become weaker than the resonance at shorter wavelengths.

Inner gold core radius fixed at 10 nm

This inner core radius was chosen based on the first experimental synthesis of MNS [Xia et al., 2006]. Figure 3.6(a) indicates that scattering increases with thicker silica layers or thicker outer gold shells or both. This behavior resembles that reported

for CNS [Lin et al., 2005a]. With a thin silica layer coating (<10 nm) [Xia et al., 2006, LizMarzan et al., 1996, Han et al., 2008], MNS exhibit more absorption than scattering. However, when the silica layer thickness is increased beyond 20 nm, MNS become mainly scattering at practical outer shell thicknesses.

Intermediate silica layer fixed at 10 nm

For these calculations, Figure 3.6(b) shows that the general trend still holds that thicker outer shells produce more scattering; however, the role of the inner gold core is less clear. Below 20 nm, an increase in the core radius slowly increases the scattering-to-extinction ratio, but this trend seems to reverse when the core radius goes above 20 nm. Another set of simulations on 20 nm silica layers (not shown here) indicate minimal effects from the gold core below 10 nm in radius and the scattering-to-extinction ratio became relatively insensitive to further increases in core radius. At thin silica layer thicknesses (<5 nm), MNS behavior is similar to solid gold colloids in that increasing the inner core radius gradually enhances scattering.

Outer shell fixed at 20 nm

Similar to the results in Figures 3.6 and 3.6(b), Figure 3.6(c) displays a profile in which absorption is dominant or equivalent to scattering for thin silica layers (<10 nm). Thicker silica layers (>10 nm) quickly turn MNS into scattering particles, with minimal impact from the inner gold core.

Outer shell and overall size fixed

To elucidate the core effect, the overall diameter and the outer shell thickness were kept fixed. The inner core radius was gradually increased to the point at which

the core made contact with the outer shell. The absorption-to-extinction ratio was obtained at the plasmon resonance, as described above, and results are shown in Figure 3.6(d).

Four different geometries with the same R_1/R_2 ratio are plotted in Figure 3.6(d). As the core radius increases, the absorption component at the plasmon resonance also increases. This is counterintuitive since we expect large gold colloids to exhibit more scattering than absorption. The explanation lies in the interplay between the gold core and other layers of the MNS. For instance, an increasing core size results in a thinner silica coating in this otherwise fixed geometry, and according to Figure 3.6(a)–3.6(c), thinner silica layers produce less scattering; this is consistent with the behavoir in Fig. 5(d). Furthermore, the discontinuities at large R_1/R_2 ratios reflect the region where the silica layer becomes so thin that the MNS resonant wavelengths lie outside the region of interest and the gold colloid resonance dominates. MNS demonstrate strong scattering characteristics associated with solid gold spheres. It can be seen that large particles (i.e. $Rx/80/100$ nm) produce more scattering than small particles (i.e. $Rx/24/30$ nm). Because one of the main advantages of MNS over CNS is their relatively small size owing to the use of small gold cores and the possibility of coating them with thin silica layers, sub-100 nm MNS are perceived as advantageous in absorption applications where NIR extinction is desired.

3.4 Angular radiation properties

To understand scattering enhancement by nanoshells in applications where detection angle and angular acceptance range may differ, angular properties need to be considered. Angular properties are commonly characterized by the overall radiation power and its directivity within certain angular ranges. The former is defined by

the scattering cross section, C_{sca}, and the latter is often described by a single-value parameter: the anisotropy factor g, which is a cosine-weighted average over all values of the scattering angle. The scattering cross section is calculated from the Mie coefficients [van de Hulst, 1981]. The anisotropy factor g is calculated as

$$g = \frac{\int_0^\pi S_{11}(\theta) cos\theta 2\pi sin\theta d\theta}{\int_0^\pi S_{11}(\theta) 2\pi sin\theta d\theta} \tag{3.1}$$

where S_{11} is the angular radiation power of unpolarized light.

For strongly scattering nanoshells (> 200 nm in size), the main extinction peak coincides with the scattering peak where the radiation pattern grows to an overall maximal level. Because MNS and CNS exhibit distinct spectra, as shown in Figure 3.3, drastically different radiation patterns are expected at some wavelengths. Figure 3.7 compares the radiation patterns from MNS and CNS computed as the radiation power normalized to the incident power at one meter from the center of the particle. The radiation power was integrated over all azimuthal angles and plotted in logarithmic form: $\log_{10}(P_{rad}/P_{inc})$. Scattering cross sections are highlighted at selected wavelengths corresponding to the radiation pattern. The overall size and outer shell thickness were chosen so that the corresponding CNS are scattering-dominant.

It can be seen that $R$90/125/140 nm MNS scatters more at 550 nm [Fig. 6(a)], whereas $R$125/140 nm CNS radiates more at 755 nm [Figure 3.7(b)] and 1145 nm [Figure 3.7(c)]. At 1270 nm the two nanoshells scatter approximately the same [Figure 3.7(d)]; this is also indicated by the nearly equivalent scattering cross sections [Figure 3.7(e)]. Although optical cross sections give an overall indication of the radiating power, they do not provide angular properties. For instance, despite an overall stronger radiation at 755 nm, $R$125/140 nm CNS does not project as much power

in the back direction as $R90/125/140$ nm MNS. From the radiation patterns above, it can also be observed that $R125/140$ nm CNS is more forward-scattering (positive g) at shorter wavelengths and becomes isotropic ($g \sim 0$) and slightly back-scattering (negative g) at wavelengths longer than the resonance wavelengths. The $R90/125/140$ nm MNS, however, does not exhibit regularities that can be associated with spectral signatures.

To further consolidate this observation, spectral properties are plotted side by side with the anisotropy factor at different wavelengths for 200 nm CNS and MNS with various layer geometries in Figure 3.8. A well-defined border between large and near-zero g values is found to follow the general trend of CNS spectra. This suggests the plasmon resonant wavelength is a boundary beyond which CNS primarily scatter isotropically. Nevertheless, MNS seem to reach low g values at shorter wavelengths prior to the plasmon resonance. This may indicate a stronger back scattering profile compared to CNS, as already seen in Figure 3.7(b).

3.5 Summary

Both spectral and angular radiation properties of gold-silica-gold multilayer nanoshells have been studied using Mie theory. The plasmon hybridization model was employed to explain the spectral tunability due to inner gold core. While the plasmon coupling strength of CNS is known to be determined by a normalized gold shell thickness, that of the MNS was found to be determined by the normalized intermediate silica layer thickness. A thinner silica layer results in a red shift of the plasmon resonance. Furthermore, the MNS spectral shift from CNS without the gold core is characterized by an exponential curve that was found to be insensitive to the particle size, when the outer shell thickness-to-particle size is fixed. This confirms the universal scaling

principle reported on particle pair systems and silica-gold core-shell CNS. MNS also demonstrate many characteristics that are similar to CNS. For instance, a thicker silica layer and a thinner gold shell both red shift the MNS spectrum (results not shown) and produce more scattering at the plasmon resonance. MNS are sensitive to the external medium and their multiple extinction peaks with deep spectral valleys may prove valuable for improving the sensitivity and specificity of various biosensing and bioimaging modalities.

Scattering patterns from MNS differ from those of CNS due to the spectral modulation induced by the core. Trends in MNS angular radiation patterns are more intricate than those of CNS. While CNS predominantly forward-scatter at wavelengths shorter than the plasmon resonant wavelength, MNS may radiate more in the back and side directions at these wavelengths.

In summary, this study compares the optical properties of composite multilayer structures with those of CNS, whose properties are well understood. Fully exploiting the potential of MNS requires synthetic studies assessing independent control of each layer, morphological and topological features, size dispersity, and protocol repeatability. It is anticipated that such studies will lead to development of multilayer nanoshells, which, in turn, will accelerate the development of new applications.

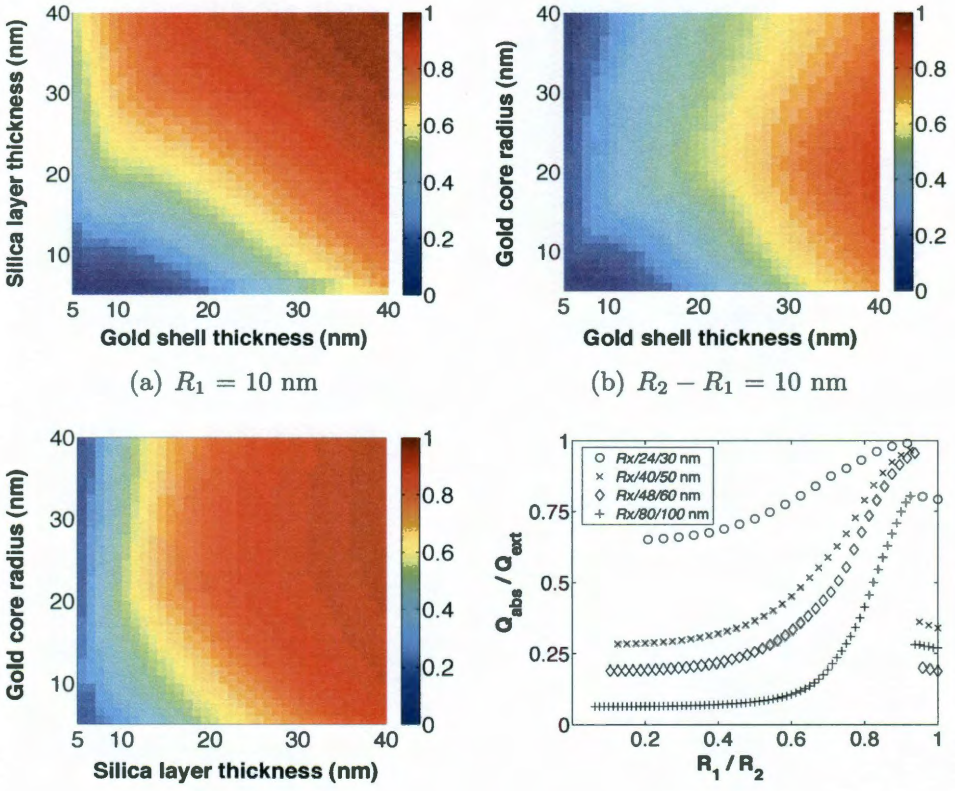

(a) $R_1 = 10$ nm

(b) $R_2 - R_1 = 10$ nm

(c) $R_3 - R_2 = 20$ nm

(d) R_3 fixed

Figure 3.6 : Scattering-to-extinction ratio at plasmonic resonant wavelengths of MNS with (a) inner gold core radius kept at 10 nm and varying the silica and outer gold layer thickness, (b) silica layer thickness kept at 10 nm and varying the inner gold core radius and outer gold layer thickness, (c) outer gold shell kept at 20 nm and varying the inner gold core radius and silica layer thickness. Absorption-to-extinction ratio (d) at plasmonic resonant wavelengths of MNS with the overall diameter and outer gold shell thickness fixed and varying the inner gold core radius and silica layer thickness.

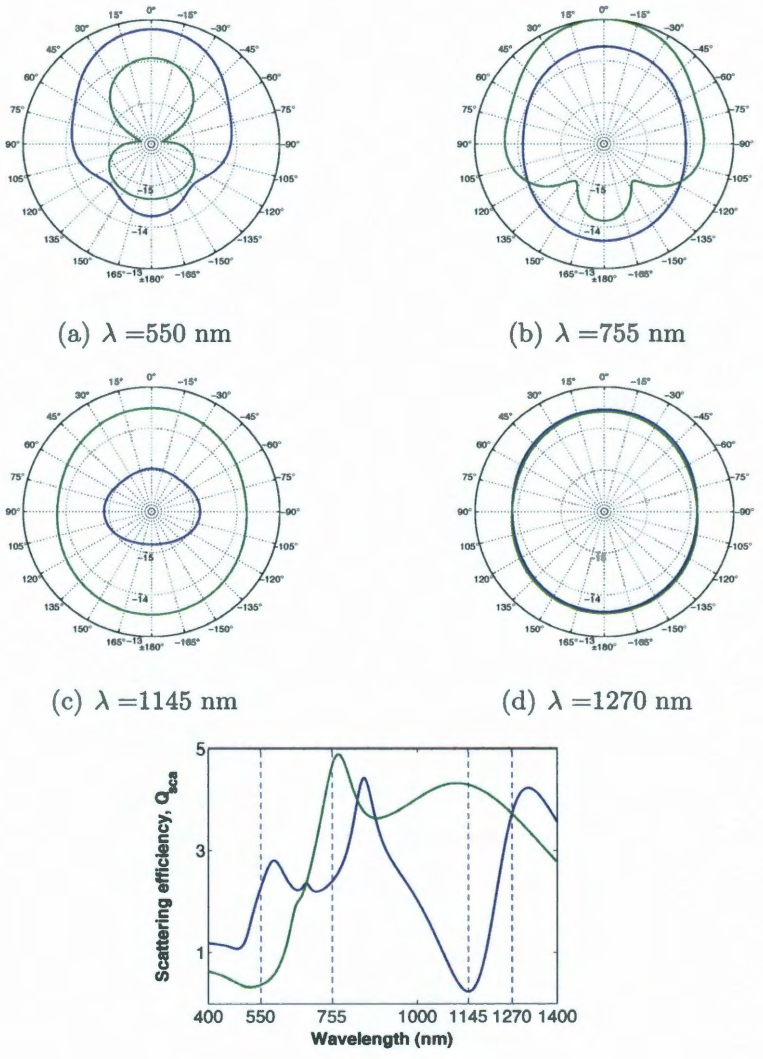

(a) λ =550 nm

(b) λ =755 nm

(c) λ =1145 nm

(d) λ =1270 nm

(e) Q_{sca}

Figure 3.7 : Angular radiation pattern of R90/125/140 nm MNS (blue) and R125/140 nm CNS (green) at (a) 550 nm, (b) 755 nm, (c) 1145 nm, (d) 1270 nm and (e) scattering spectra of MNS (blue) and CNS (green)). Nanoshells are located in the center of the plot, and the incident wave enters from the bottom (180°).

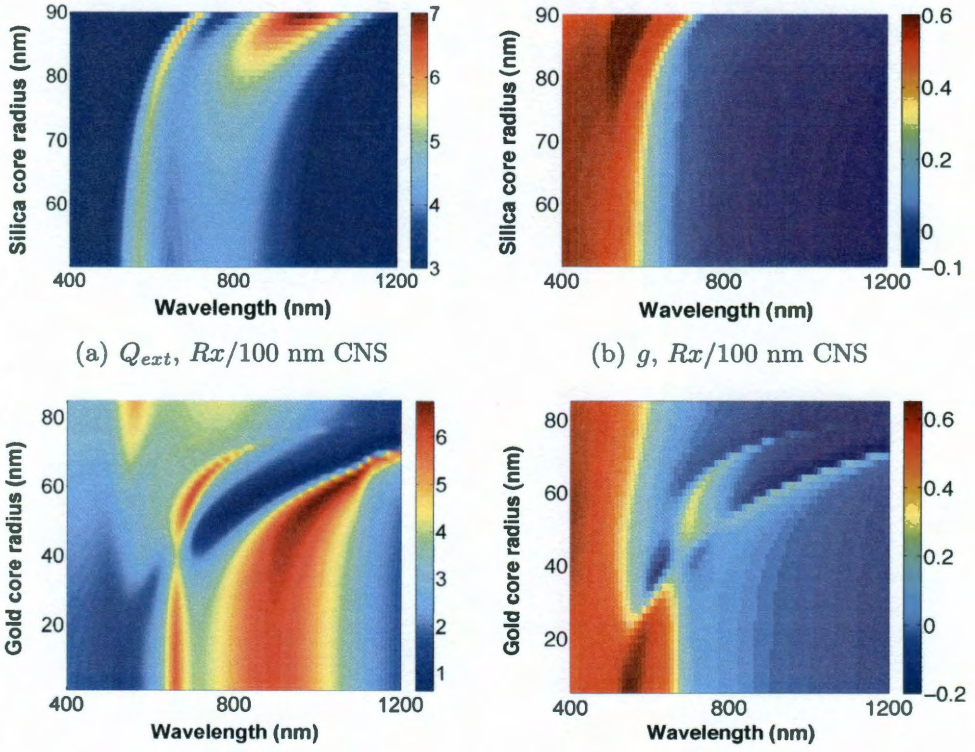

(a) Q_{ext}, $Rx/100$ nm CNS

(b) g, $Rx/100$ nm CNS

(c) Q_{ext}, $Rx/85/100$ nm MNS

(d) g, $Rx/85/100$ nm MNS

Figure 3.8 : (a) Extinction efficiency spectra for $Rx/100$ nm CNS with varying silica core radius x. (b) Anisotropy factor plot for corresponding CNS at different wavelengths. (c) Extinction efficiency spectra for $Rx/85/100$ nm MNS with varying gold core radius x. (d) Anisotropy factor plot for corresponding MNS at different wavelengths.

Chapter 4

Chemical synthesis of gold-silica-gold multilayer nanoshells *

Synthesis of multilayer nanoshells starts with monodisperse gold colloids. The colloids are coated with silica using a modified Söber method. The final gold layer is coated using a method similar to coating gold onto silica cores in silica-gold core-shell nanoshells. Figure 4.1 depicts the synthesis process. In this chapter, I will discuss the effort on making gold colloids as well as coating colloids with silica. The final multilayer nanoshells and future challenge will be briefly discussed.

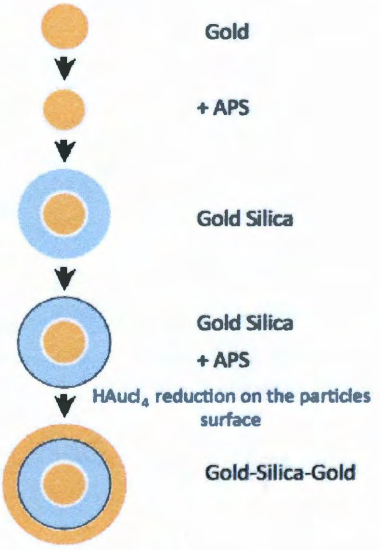

Figure 4.1 : Fabrication of gold-silica-gold multilayer nanoshells.

*Partially adapted from V. Nammalvar, E. Figueroa, J. Young, Y. Hu, M. Hung, D. Benoit, and R. A. Drezek, Synthesis of Monodispersed Silica-Coated Gold Particles: A Systematic Approach, in preparation.

4.1 Synthesize gold colloids using the citrate method

Controlled nucleation in monodisperse gold suspensions has been reported by Frens as early as 1973 [Frens, 1973]. The method involves using sodium citrate to gradually reduce Au from the $HAuCl_4$ solution. The reaction takes place quickly in a heated environment and is accompanied by a series of color changes. The final color of the solution depends on the diameter of the gold colloids, as Fren outlined in Table 4.1:

Table 4.1 : Amount of sodium citrate for making monodisperse gold nanoparticles. [Frens, 1973]

Diameter (nm)	Amount of sod. cit. (μl)	Color
16	800	Orange
24.5	600	Red
41	400	Red
71.5	240	Dark red
97.5	168	Violet
147	128	Violet

The following procedures were followed to synthesize 20 ml gold colloids of various sizes:

1. Prepare 0.01% by weight $HAuCl_4$ solution (I) and 0.5% by weight sodium citrate solution (II).

2. Dissolve 1.83 mg (corrected after Turkevich paper) $HAuCl_4$ in 20 g (ml) DI water (the result should be a faintly yellowish solution). Dissolve 50 mg sodium citrate in 10 g (ml) DI water.

3. Heat solution I till it boils.

4. Continue the heating and, while stirring vigorously, add solution II; keep stirring for the next 30 minutes. The amount of sodium citrate is listed in Table 4.1 based on the desired particle diameter. A series of color change will occur, i.e. faint yellow to clear to grey to purple to deep purple.

5. Add water to the solution as necessary to bring the volume back to 20 ml.

The entire process takes about half an hour. Figure 4.2 demonstrates the time course of the color change. The flask on the left of the hotplate has 110 ml $HAuCl_4$ stock solution mixed with 4.4 ml sodium citrate (producing 16 nm gold colloids), and the one on the right has 110 ml $HAuCl_4$ stock solution mixed with 1.3 ml sodium citrate (producing 71 nm gold colloids). Both flasks were heated up to 150^{o}C and stirred at 585 *rpm*. Change of color was observable within the first 10 minutes. The initiation of the color change was first observe on the flask with small colloids. However, the speed at which the color changes appeared to be faster on the flask with large colloids. Reactions in both flasks were complete in half an hour, with a deep burgundy color.

The following two samples prepared gold colloids of 23 and 40 nm:

	sod. cit. (0.5% by wt.)	$HAuCl_4$ (1%)
sample 1	800 μl	20 ml
sample 2	400 μl	20 ml

Both samples were heated up to 150 ^{o}C and stirred at 485 *rpm*.

Figure 4.3 shows TEM images of the gold colloids right after synthesis and after 17 hrs of storage in the fridge. No significant change in sizes was observed before and after the storage. Table 4.2 was obtained from measurements of 20 particles in each TEM image. The dispersion of the size distribution depends both on the temperature

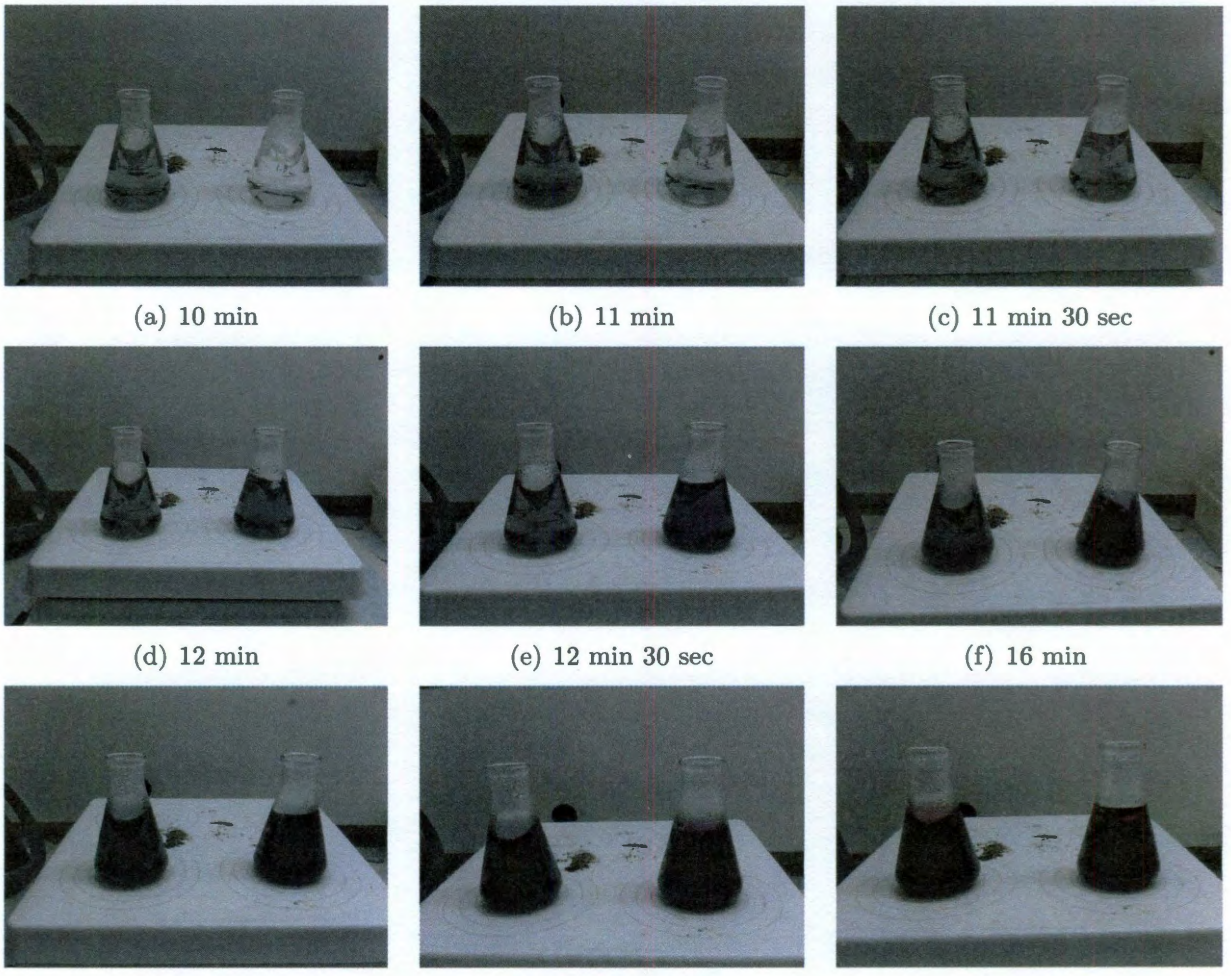

(a) 10 min (b) 11 min (c) 11 min 30 sec

(d) 12 min (e) 12 min 30 sec (f) 16 min

(g) 21 min (h) 23 min 30 sec (i) 29 min

Figure 4.2 : GC color change, left 16 nm (4.4 ml sodium citrate), right 71 nm (1.3 ml sodium citrate), faint yellow to light grey to dark gray to violet to purple to dark red.

of the solution, the stirring speed, as well as how fast one adds sodium citrate to the stock solution. Figure 4.4 shows the measured extinction spectra. The extinction peak of sample 2 is slightly red shifted from sample 1 due to the larger size of the gold colloids.

Table 4.2 : Gold colloid dimensions before and after the storage.

	avg. dia. [nm]	stdev [nm]
sample 1 after syn	24.41	7.72
sample 1 after 17 hrs	23.86	4.86
sample 2 after syn	40.57	4.86
sample 2 after 17 hrs	38.33	4.11

4.2 Coating gold colloids with silica

Thin silica coating is achieved by using a modified Stöber method:

1. Preparation of 1mM (3-aminopropyl)trimethoxysilane (APS) solution–1a: make 1M soln: add 175μl of APS into DI water till the total volume reaches 1mL. 1b: dilute 1000X: take 100μl of APS solution, add to 9.9ml of DI water (100X), then take 1ml of the mixed solution and add to 9ml of DI water (10X).

2. Add 50 μl, 1 mM freshly prepared aqueous (3-aminopropyl)trimethoxysilane solution to 10 ml of the 20 nm gold solution (5.0×10^{-4} M in $HAuCl_4$) under vigorous magnetic stirring.

3. Leave the mixture of (3-aminopropyl)trimethoxysilane and gold dispersion for 15 min (to ensure complexation of the amine groups with the gold surface).

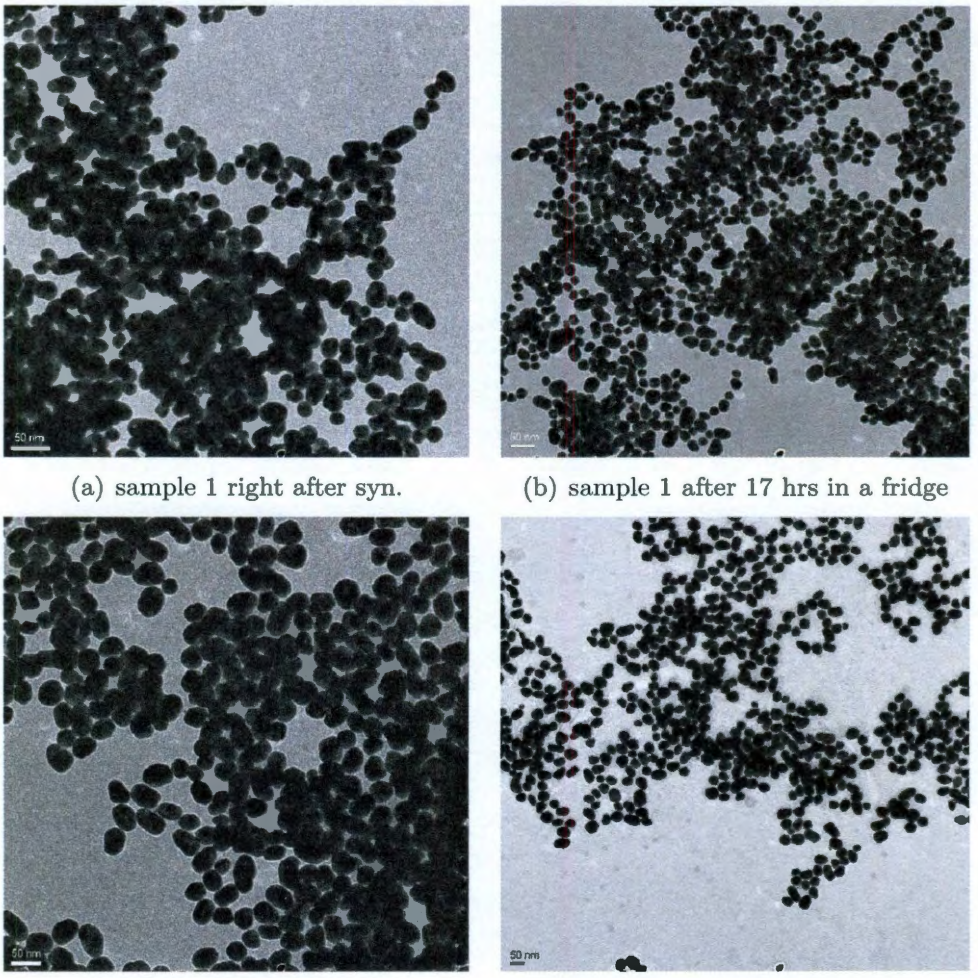

(a) sample 1 right after syn.

(b) sample 1 after 17 hrs in a fridge

(c) sample 2 right after syn.

(d) sample 2 17 hrs in a fridge

Figure 4.3 : TEM of the 20 and 40 nm gold colloids right after synthesis and after 17 hrs storage in a fridge.

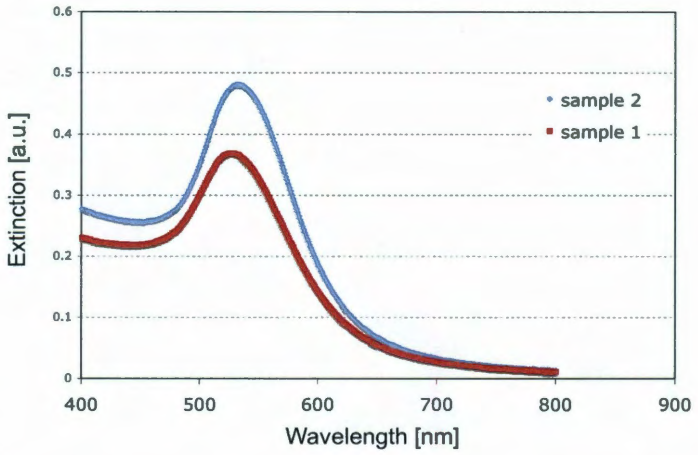

Figure 4.4 : Measured extinction spectra of the gold colloids.

4. Prepare the active silica: add water to 0.5 g of sodium silicate till the total mass reaches 25 g – this gives 0.54 wt% soln. progressively add the cation exchange resin to lower the pH of a 0.54 wt% sodium silicate solution to 10-11 (the sodium form of cation exchange resin is converted into the acid form by repeated washing with HCL and water).[†]

5. Add 400 μl of active silica to 10 ml of the surface modified gold, under vigorous magnetic stirring[‡].

6. Stand the resulting dispersion (pH=8.5) for at least one day(48 hrs or longer preferred); (so the active silica polymerizes onto the gold particle surface).

7. Transfer the particle to water/ethanol (1:4) mixture for further growth of silica layer (Söber method).

8. Add 20 ml ethanol to 5 ml active silicate treated gold particle (with $\sim$ 4 nm

[†]This is necessary to avoid aggregation of small gold particles in the alcoholic solutions

[‡]This is best done in plastic containers

silica), add 60 μl tetraethoxysilane (200μl TEOS results in 100 nm silica and 20μl TEOS results in 6 nm silica [Xia et al., 2006], 35 nm silica-coated particles could grow to 50, 65, and 80 nm by adding 50, 100, and 200μl of fresh TEOS[Langmuir 2008]). *After* the addition of TEOS under MILD stirring, add 100 μl of aqueous ammonia to ensure that single nuclear growth occurs. Magnetically stir for 12 hrs. The resultant particles have a silica shell thickness of around 20 nm. Purify by centrifuging at 2500 rpm for 6 hrs and re-disperse in 5 ml of thanol for future use.

The centrifugation in the last step was found to be crucial to remove impurities (*i.e.*, free silica) from the silica-coated gold nanoparticles. Meanwhile, the further growth of the silica layer was observed during the centrifugation, as shown in Figure 4.5. The growth can be stopped by adding methanol to the ethanol solution. The small molecular weight of methanol dramatically slows down the growth of silica.

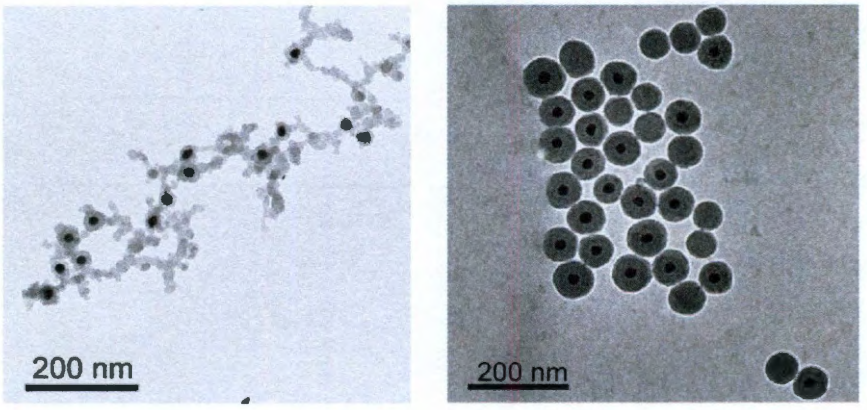

Figure 4.5 : Silica-coated 30 nm gold colloids before and after centrifuge.

4.3 Coating the outer gold layer

The method of coating the outer gold layer to silica follows the same protocol that has been outlined for silica-gold nanoshells. The following procedures outline the process:
a) Priming the silica-coated gold nanoparticles.

1. Add 500 μl (3-aminopropyl)trimethoxysilane (1mM) to a 5 ml aliquot of silica-coated gold nanoparticles, vigorously stir in ethanol solution. Leave the solution for 12 hrs.

2. Observe the separation of the solution into two layers when left unstirred – the (3-aminopropyl)trimethoxysilane-coated silica nanoparticles precipitate to the bottom, leaving clear ethanol at the top.

3. Gently reflux for one additional hour, to allow enhanced covalent bonding, centrifuge at 2000 rpm for one hour and re-dispense in water5 ml.

4. Transfer 2.5 ml aliquot of the (3-aminopropyl)trimethoxysaline-treated silica nanoshells water suspension ($\sim 7.0\times10^{11}$) to a 15 ml BD Falcon conical tube and agitate for 20 min, add 5 ml of 2 nm gold colloid ($\sim 1.5\times10^{14}$ particles per ml), gently shake for 2 min and allow to sit overnight.

5. Centrifuge at 2500 rpm for 3 hrs, decant the supernatant, leaving the dark colored pellet, re-disperse in 2.5 ml purified water and sonicate.

6. Take TEM images.

b) Formation of outer gold layer.

1. Dissolve 25 mg (0.18 mmol) potassium carbonate in 100 ml of HPLC-grade water, stir for 10 min, add 1.5 ml (20 mmol) of a solution of 1.0 wt% $HAuCl_4$

in water; (the solution initially appear transparent yellow and slowly became colorless over the course of 30 min, indicating the formation of gold hydroxide).

2. Age the resulting solution for 24 hrs in dark.

3. Add 4 ml colorless gold hydroxide solution to 1 ml of the gold primed silica-coated gold nanoparticles, add 10 μl of 37 wt% formaldehyde water solution to the nanoparticle gold hydroxide solution. Over the course of 5 min, the solution changes from colorless to light blue.

4. Nanoshells under dialysis for two days and centrifuged and re-dispersed in HPLC-grade water.

The general challenge of making multilayer nanoshells is the low particle concentration due to the loss of particles in the centrifugation process. Figure 4.6 shows the TEM and SEM images of an $R25/52$ nm silica-coated gold nanoparticles before and after the deposition of the outer gold shell. Bardhan *et al.* used a CO gas bubbling method to coat the outer gold layer. The group achieved synthesizing sub–100nm multilayer nanoshells.

4.4 Summary

In summary, the procedures of making multilayer nanoshells are outlined as three steps: 1) making the gold colloids, 2) coating gold colloids with silica, and 3) coating silica with gold. It is anticipated that the uniformity of the gold colloids can be further improved. In addition, further investigation should be carried out to study the optimal centrifugation speed in order to minimize the loss of the particles during the washing process.

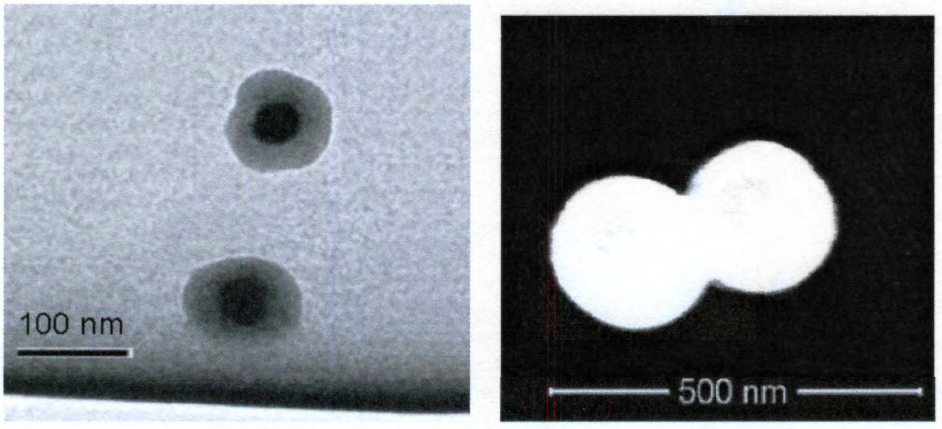

(a) (b)

Figure 4.6 : (a) TEM image of the $R25/52$ nm silica-coated gold nanoparticles. (b) SEM image of the $R25/52/72$ nm gold-silica-gold multilayer nanoshells.

Chapter 5

Symmetry breaking in gold-silica-gold multilayer nanoshells*

In Chapter 3, I investigated the spectral and angular radiation properties of concentric multilayer nanoshells. I explained the additional tunability of the multilayer nanoshells from the inner core using a hybridization model. It is not difficult to observe from the previous chapter that synthesized multilayer nanoshells exhibit irregularities in shape and morphology. In this chapter, I examine a simple case where the inner gold core is offset from the center [Hu et al., 2010]. Symmetry breaking results in rather interesting new properties that are not seen in the concentric geometry. Herein, I present a computational study of the plasmonic properties of gold-silica-gold multilayer nanoshells with the core offset from the center. Symmetry breaking, due to the core offset, makes plasmon resonances that are dark in concentric geometries visible. Applying plasmon hybridization theory, I explain the origin of these resonances from the interactions of an admixture of both primitive and multipolar modes between the core and the shell. The interactions introduce a dipole moment into the higher order modes and significantly enhance their coupling efficiency to light. To elucidate the symmetry breaking effect, I link the geometrical asymmetry to the asymmetrical distribution of surface charges and demonstrate illustratively the diminishing multipolar characteristic and increasing dipolar characteristic of the higher

*Adapted from Y. Hu, S. J. Noelck, and R. A. Drezek, Symmetry breaking in gold-silica-gold multilayer nanoshells, *ACS Nano*, **4**(3), pp1521-1528, 2010

order modes. The relative amplitudes of the modes are qualitatively related by visual examination of the dipolar component in the surface charge distributions. Using polarization-dependent surface charge plots, I illustrate two distinct mode configurations despite their spectral similarities. I further demonstrate a trend of increasing absorption relative to scattering as the resonant wavelength red shifts in response to a larger core offset.

5.1 Background on symmetry breaking

Up to date, symmetry breaking has been investigated in a variety of gold nanostructures from three-dimensional nanoeggs [Knight & Halas, 2008] and nanocups [Knight & Halas, 2008, Wang et al., 2006], to two-dimensional disk/ring [Hao et al., 2009, Hao et al., 2008], two-layer, and planar nanocavities [Liu et al., 2010, Liu et al., 2009]. In nanoeggs, where the silica core is off-centered in a silica-gold core-shell nanoshell, both far-field and near-field properties have been studied as functions of the core offset [Knight & Halas, 2008]. It was found that a larger offset correlates with larger red shifts in the low-energy plasmon resonant peaks, a stronger near-field enhancement, and a larger absorption-to-scattering ratio at the dipole resonance [Knight & Halas, 2008]. The polarization of light only weakly affects the far-field spectrum [Wang et al., 2006]. However, in nanocups where the gold shell is partially opened up by the offsetting core, the far-field scattering spectrum strongly depends on polarization owing to its anisotropic geometry [Lassiter et al., 2009]. As the core further protrudes from the shell, dipole modes gradually weaken and eventually vanish [Knight & Halas, 2008].

Studies of two-dimensional structures have revealed some interesting phenomena. In geometries with reduced symmetry, the highly-damped multipolar modes

are excited and interact with the dipole mode. Liu and co-workers demonstrated a carefully designed planar geometry in which the narrow quadrupole resonance of the nanobar/nanoslit dimer destructively interferes with the broad dipole mode of the nanobar/nanoslit monomer that is off-centered, leading to a narrow region where light transmission is significantly enhanced; in atomic physics this is known as electromagnetically enhanced interference (EIT) [Liu et al., 2010, Liu et al., 2009]. Similarly, Hao et al. reported a nonconcentric ring/disk nanocavity in which the broad dipole mode both constructively and destructively interferes with a sharp quadrupole mode. The interaction results in an asymmetrical sharp Fano-type resonance [Hao et al., 2009, Hao et al., 2008]. Due to the sharp nature of the Fano resonance, symmetry-breaking geometries have been proposed for nanoscale optical sensing such as high figure-of-merit metamaterial sensors [Liu et al., 2010]. It has also been found that offset geometries exhibit significantly larger local-field enhancement, making them promising for surface-enhanced spectroscopies [Knight & Halas, 2008, Wang et al., 2006, Hao et al., 2009].

MNS preserve three-dimensional spherical symmetry, as in nanoeggs and nanocups, but they also exhibit symmetry-breaking patterns similar to ring/disk nanocavities. Theoretical investigations of concentric MNS have been previously reported using various Mie-base approaches [Chen et al., 2005a, Khlebtsov & Khlebtsov, 2006, Hu et al., 2008a, Wu & Liu, 2009]. It has been found that the addition of a gold core to the gold shell splits the low-energy plasmon resonance of a conventional silica-gold core-shell nanoshell (CNS) into a high-energy anti-bonding mode and a low-energy bonding mode that can be tuned from the visible region into the infrared. The red shift of this mode correlates with intermediate silica layer thickness, which determines the strength of coupling between the core mode and the CNS mode. As the

mode red shifts, the MNS becomes relatively more absorbing than scattering at the bonding-mode resonance [Hu et al., 2008a]. An experimental study of MNS has also been published. Xia and co-workers reported the chemical synthesis of sub-100 nm multilayer nanoshells [Xia et al., 2006]. The silica coating on gold was achieved using a modified Stöber method [Graf et al., 2003, Kobayashi et al., 2005, Lee et al., 2006, LizMarzan et al., 1996]. The final gold layer was coated in a way similar to synthesizing silica-gold core-shell nanoshells [Westcott et al., 1998, Oldenburg et al., 1998, Bardhan et al., 2010]

Here I use a computational model to investigate MNS with an offset geometry: the inner gold core is moved away from the center but does not touch the gold shell, as illustrated in Figure 5.1. The MNS dimensions are denoted by the radius of each layer, R_1, R_2, and R_3, as well as the core offset, Δx, shown in Figure 5.1(b). I apply plasmon hybridization theory to obtain insight into spectral properties of the MNS. This theory is analogous to molecular orbital theory and describes how the fixed-frequency plasmons of elementary nanostructures hybridize to create more complicated resonances. It has been used to explain the plasmonic properties of structures ranging from concentric nanoshells [Prodan et al., 2003a, Radloff & Halas, 2004] to nanorice [Sealy, 2006, Srivastava & Lee, 2006, Wang et al., 2006b, Wiley et al., 2007] to nanosphere trimers [Brandl et al., 2006, Jain & El-Sayed, 2008] and quadrumers [Brandl et al., 2006]. Some interesting examples of plasmon hybridization applied to nonsymmetrical structures include analyzing the aforementioned nanocups [Knight & Halas, 2008, Wang et al., 2006, Lassiter et al., 2009] and nonconcentric ring-disk structures [Hao et al., 2009, Hao et al., 2008].

The far-field properties of MNS were simulated using a finite-element method (FEM) package: COMSOL Multiphysics v3.5a with the RF module. Because the

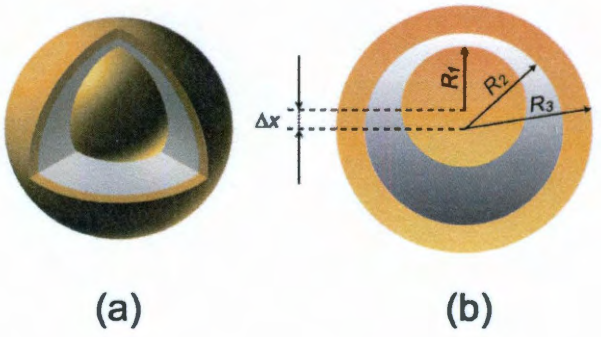

Figure 5.1 : (a) Three-dimensional illustration of a gold–silica–gold multilayer nanoshell with an offset core. (b) Dimensions of an $R_1/R_2/R_3$ gold-silica-gold multilayer nanoshell with core offset Δx.

dimensions of the gold core and shell remain unaltered as the location of the core changes, the offset process itself does not require size correction for the dielectric function of gold due to intrinsic effects. It should also be noted that this work does not focus on the spectral width of plasmon resonances, which can be considerably broadened by the surface scattering of electrons in nanostructures [Berciaud et al., 2005b, Kreibig & Vollmer, 1995, Moroz, 2008, Nehl et al., 2004].

5.2 Methodology

For the FEM simulations, gold properties were obtained from Johnson and Christy [Johnson & Christy, 1972]. The dielectric constant of silica was set to 2.04, and that for water to 1.33. The surrounding medium of MNS was water. Simulations were performed in COMSOL Multiphysics v3.5a. The simulation space and perfectly matched layer thickness were adjusted until agreement was obtained between the FEM and Mie-based calculations [Hu et al., 2008a]. For optical spectra, the scattering efficiency

was calculated by integrating the normalized E field around a far-field transform boundary enclosing the MNS. The absorption efficiency was calculated by summing time-average resistive heating on the inner gold core and other gold shell. For surface charge plots, Gausss law was applied:

The gradient operation was realized by implementing the up and down operators to the metal-dielectric interfaces in COMSOL. Mie calculations were implemented in an in-house Matlab code written for simulating light scattering from concentric spheres with arbitrary number of layers [Hu et al., 2008a]. The dielectric function of gold was kept the same as the one used in FEM calculations, so were other parameters such as the refractive index of silica and water. The Mie code has been previously validated against literature results [Hu et al., 2008a, Bohren & Huffman, 1983].

5.3 Plasmon hybridization

An MNS can be modeled as a hybrid between a silica-gold core-shell nanoshell and a solid gold core. I apply plasmon hybridization to explain the optical properties of MNS using these two basic nanostructures. The hybridization diagrams in Figure 5.2 show, for both the concentric and offset MNS, the interactions between the hybridized modes of the nanoshell and the spherical plasmon modes of the core. For clarity, only the dipolar and quadrupolar interactions are shown. The anti-bonding modes from the nanoshell are not shown because they are higher energy and have only very weak interactions with the core mode. The left panel of Figure 5.2 shows the hybridization diagram for the concentric MNS where the modes of different angular momenta are forbidden from interacting. Like the hybridization between the inner and outer layers of a nanoshell, there are two modes for each interaction: a low-energy bonding mode and a higher energy anti-bonding mode. This can be seen in the left panel of Figure 5.2

for the dipole-dipole ($l = 1$) and quadrupole-quadrupole ($l = 2$) interaction. For the nonconcentric case the selection rules for interaction are relaxed, allowing modes of different orders to mix. As depicted in the right panel of Figure 5.2, the dipole mode ($l = 1$) of the core can now interact with not only the dipole mode ($l = 1$) of the shell, but also the quadrupole and higher order modes ($l = 2$, 3, *etc.*) of the shell. Additionally, the quadrupole ($l = 2$) of the shell can now interact with the dipole ($l = 1$) of the core, bringing in the dipole moment into the quadrupole mode.

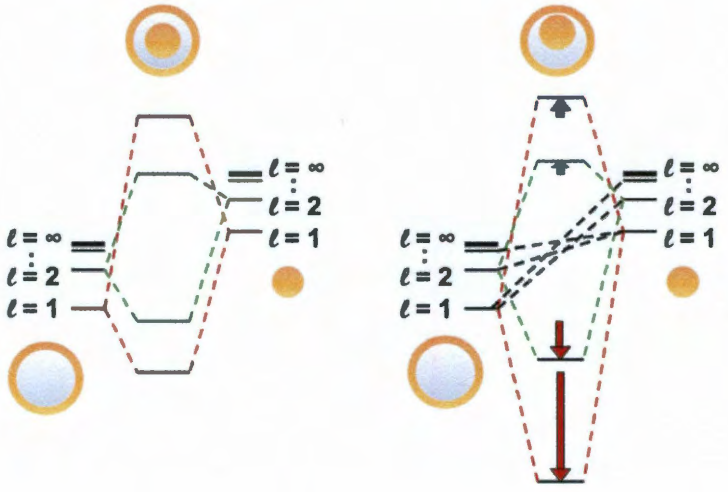

Figure 5.2 : Hybridization diagrams of MNS with concentric (left) and offset (right) geometries. The left panel illustrates the plasmon hybridization diagram for a concentric MNS with interaction between modes having the same angular momentum (energy increases from bottom to top). The right panel displays the nonconcentric MNS case with black lines showing additional interactions and arrows showing the relative red shift and blue shift (not to scale). Only dipole and quadrupolar interactions are shown for clarity.

The hybridization between different modes on the core and the shell also results in red shifts of the hybridized bonding modes of MNS. The lower order modes are red shifted as they become repelled by the interaction with higher order modes. As shown in the right panel of Figure 5.2, this yields a shift for the predominately

dipole-dipole hybridized modes that is larger than for the quadrupolar-quadrupolar hybridized modes, and so on. In addition to a red shift of the bonding modes, the anti-bonding hybridized modes are slightly blue shifted. This leads to a very asymmetrical splitting of the hybridized energy modes. Such asymmetrical splitting is seen in other nanostructures as the symmetry is broken [Wang et al., 2006, Hao et al., 2008, Wu & Nordlander, 2006], as well as in nanoparticle dimers [Lassiter et al., 2008a, Nordlander et al., 2004]. The degree of the shift is determined by the strength of the interactions between the different modes. As the gold core is offset more and approaches the gold nanoshell, and the plasmons of the core interact more strongly with plasmons of the shell. These increasing interactions lead to stronger mixing between the different modes, creating a greater shift from the concentric MNS interactions.

5.4 Symmetry breaking in MNS with different geometries

As seen in the work on concentric multilayer nanoshells, changing the ratio of the core, silica layer, and the outer layer allow tuning of the plasmon resonance [Hu et al., 2008a]. This same effect is seen in offset multilayer nanoshells as well. Figure 5.3 and Figure 5.4 show the extinction spectra of the offset MNS with two different $R_1/R_2/R_3$ ratios as well as different outer radii R_3. Figure 5.3 shows $R10/15/25$ nm MNS in water with various core offsets. The black stars from the Mie calculation agree very well with the black curve from the FEM calculation of a concentric geometry. Two distinct plasmon resonant peaks can be observed in the concentric spectrum. The high-energy peak around 530 nm is the anti-bonding mode of the dipole-dipole interaction between the shell and the core along with other higher order modes. The interband transitions of gold lead to a pronounced broadening and damping of all modes in this region [Hao & Nordlander, 2007, Pinchuk et al., 2004, Perner et al.,

1997]. The low-energy peak at 643 nm is the bonding mode of the dipolar interaction. Quadrupole modes are not excited as the particle lies in the quasi-static region. When the symmetry is reduced and the mode selection rule for hybridization is relaxed, modes of different angular momenta start to interact [Knight & Halas, 2008, Wang et al., 2006, Wu & Nordlander, 2006]. Among the offset spectra, one can immediately observe a red shift of the dipolar bonding mode. The fact that the dipole of the core is allowed to interact with the quadrupole of the shell and vice versa shifts the bonding mode to a lower energy. The blue shift of the anti-bonding mode, however, is too small to be visualized in the spectrum. In addition to the red shift of the bonding modes and blue shift of the anti-bonding modes, hybridization results in the appearance of dark modes that were only weakly excited or not excited at all in the concentric MNS. For instance, one can observe the emergence of a new peak at about 592 nm. This peak is likely to be the bonding mode of the quadrupole-quadrupole interaction between the shell and the core (noted by $l = 2$ in the hybridization diagram). This mode can be directly excited because the interaction between the quadrupolar and dipole modes introduces a small overall dipole moment in the plasmon. This mode is not excitable in the concentric case because of the lack of the dipole moment in the quadrupole-quadrupole interaction.

Although interesting in nature, the quadrupole peak is still not very well-defined at the largest offset I calculated. In Figure 5.4, I demonstrate the spectra of a larger MNS: $R30/40/50$ nm in water with a different $R_1/R_2/R_3$ ratio (3/4/5 instead of 2/3/5). The particle lies outside the quasi-static region and can provide opportunities to observe sharp higher order modes. As shown in Figure 5.4, good agreement was obtained between Mie and FEM calculations on the concentric geometry. The relatively large size of the MNS and limitations from the meshing and scattering

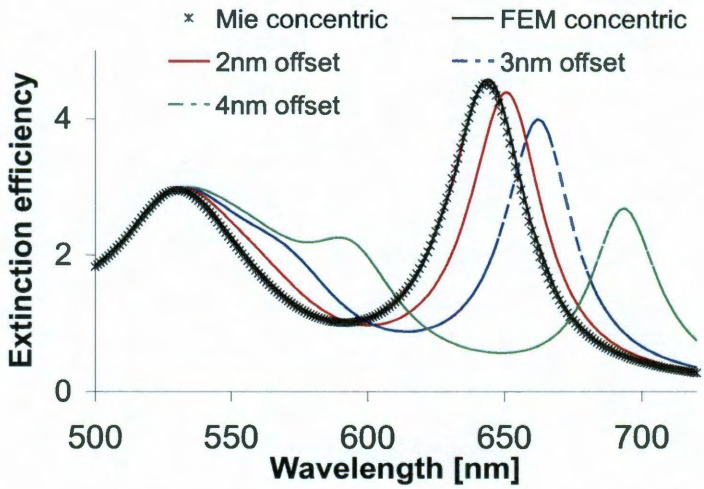

Figure 5.3 : Extinction spectra of $R10/15/25$ nm MNS in water with various core offsets. Core offsets in y; incident light linearly polarized in x and propagates in z.

boundary condition in COMSOL v3.5a may account for the 6% discrepancy on the peak intensity at 890 nm [Khoury et al., 2009]. For clarity, each resonant peak is labeled with a numerical value associated with its mode (*i.e.*, 1 for dipole, 2 for quadrupole, *etc.*), followed by a letter denoting the core offset of that spectrum.

In the concentric spectrum, in addition to the dipolar modes at 1a and 1*a, a slight quadrupolar peak can be observed at 2a. The excitation of this mode is attributed to the retardation effect as the particle size is comparable to the excitation wavelength. Its small amplitude reflects a lack of the dipole moment. More specifically, the amplitude of the extinction peak is directly proportional to the square of the dipole moment. When the symmetry is reduced, as shown in the 7 nm offset spectrum (red), the dipolar bonding mode is red shifted from 886 nm to 934 nm (1a to 1b) and the quadrupolar bonding mode is shifted from 644 nm to 688 nm (2a to 2b). While the peak intensity of 1b is decreased, that of 2b is significantly enhanced. The enhancement at 2b is due to the dipole-quadrupole interaction that adds a dipolar

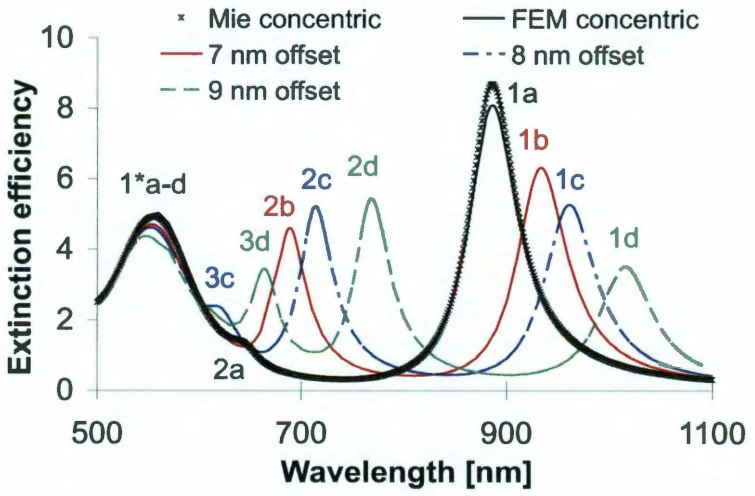

Figure 5.4 : Extinction spectra of the $R30/40/50$ nm MNS in water with various core offsets. Core offsets in y; incident light linearly polarized in x and propagates in z.

component into the quadrupole mode. Likewise, the interaction between the dipole of the core/shell and higher order modes of the core/shell introduces dark characteristics of the multipolar modes into 1b and causes its amplitude to decrease.

From a macroscopic perspective, the *f-sum law* can be used to interpret the relative change of the peak amplitude at each plasmon mode [Noziers & Pines, 1958, Mahan, 1990]. In the MNS system where the number of oscillating electrons is fixed, the convolution of the amplitudes of plasmon resonances with their energy levels remains a constant. This does not however indicate that an increase in one peak necessarily causes a decrease in another peak. In the 7 nm offset spectrum, nevertheless, the significant gain at the high-energy quadrupolar mode demands that the dipolar mode be both down shifted in energy and decreased in amplitude.

As the core continuously moves away from the center, more modes that are completely dark in the concentric spectrum start to emerge. In the 8 nm (blue) and 9 nm (green) offset spectra, the emergence of the 3c mode at ~620 nm and the 3d mode at

664 nm are the octupole mode excited with added dipole components. As previously described by the f-sum law, the introduction of this new octupole mode results in a decrease in amplitude of the dipole mode at 1c and 1d.

5.5 Surface charge distribution and the polarization effect

While hybridization theory qualitatively explains the plasmon resonances of MNS, it does not provide information regarding charge distributions on metal-dielectric interfaces at each resonant mode. Furthermore, it does not describe the relative amplitude of each peak nor the polarization effect on the spectrum. Therefore, I supplement the hybridization analysis with surface charge distributions at the outer and inner layers of the gold shell as well as the surface of the gold core at resonant wavelengths. I examine both spectral properties and charge distributions of the MNS when the incident light is axially polarized with respect to the core offset and when it is transversely polarized. Figure 5.5 shows the extinction spectra of the $R30/40/50$ nm MNS with a 9 nm offset core at two different polarizations. The dipole, quadrupole, and octupole resonances can be clearly recognized, as described in previous sections. To facilitate the analysis, I denote these modes in the following fashion: dipole modes 1d (transverse) and 1d′ (axial), quadrupole modes 2d (transverse) and 2d′ (axial), and octupole modes 3d (transverse) and 3d′ (axial). One can observe that the two spectra have very similar shapes, indicating minimal impact from polarization. It is worth noting that reported in the literature are three-dimensional nanoparticles whose plasmon resonances do not largely depend on the polarization, such as nanoeggs [Wang et al., 2006], and nanoparticles whose spectra bear distinct polarization-dependent characteristics, such as nanocups [Lassiter et al., 2009]. I conjecture that since the offset MNS bear more resemblance to the nanoegg structure, the spectra should be

largely polarization independent. One can observe in the axial spectrum slight red shifts in the bonding modes: from 1016 nm to 1094 nm for the dipole mode, 768 nm to 785 for the quadrupole mode, and 664 to 670 nm for the octupole mode. The red shift implies a stronger interaction between modes with different angular momenta when the light is axially polarized along the small gap between the core and the shell. One can also observe that 1d′ has the largest red shift whereas 3d′ has the least. This is in agreement with the plasmon hybridization theory shown in Figure 5.2. In addition, the quadrupole and octupole peaks in the axially polarized spectrum (2d′ and 3d′) appear to be higher than those in the transversely polarized spectrum (2d and 3d), possibly owing to the stronger interaction. In both spectra, the quadrupole peaks (2d and 2d′) appear to be higher than the octupole peaks (3d and 3d′). I will now explore these observations from the surface charge perspective. To calculate the surface charge, Gausss law was applied to metal-dielectric interfaces. The phase of the solution was swept to find the correct distribution that corresponds to the maximal surface charge density. The extinction spectrum was calculated for the geometry in which the core offset and light polarization were (1) in orthogonal directions (transverse) and (2) along the same direction (axial).

5.5.1 Transverse polarization

Figure 5.6 shows the charge distribution on metal-dielectric interfaces for plasmon modes in the transverse spectrum. Side and top views (left and right panel) are provided. The color scales (not shown) on each surface are different for better illustration. Three relevant observations can be made. First, the distributions at 3d, 2d, and 1d resemble octupole, quadrupole, and dipole-like characteristics, respectively. Opposite charges are found on the surface along the E field direction in which light is

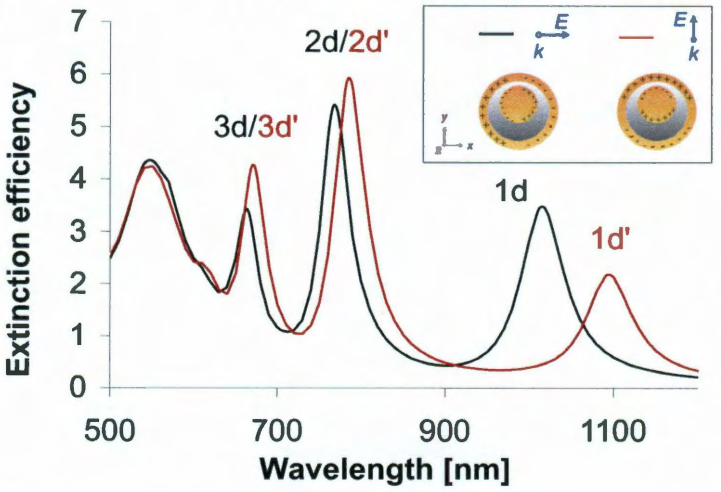

Figure 5.5 : Extinction spectrum of the $R30/40/50$ nm MNS in water with 9 nm core offset. Black: incident light is transversely polarized with respect to the offset; red: incident light is axially polarized along the offset.

polarized. At each resonance, the charge distribution exhibits an alternating half-ring shape stacked from the top to the bottom of the particle. The pattern is consistent with the predictions I made using plasmon hybridization theory. Second, one observes that the charge polarity is the same along the inner and outer surfaces of the gold shell. This corresponds to the bonding-mode configuration of the shell and indicates that the core is in fact interacting with the bonding mode of the shell. Further, the charge polarity on the inner core is oppositely aligned with the outer shell. This also corresponds to the low-energy configuration (bonding) of the MNS and indicates that the plasmon resonance is the low-energy bonding mode from the core-shell interaction. Lastly, the octupole, quadrupole, and dipole distributions appear spatially distorted. The nature of the spatial asymmetry indicates that the hybridized modes are composed of a mixture of modes with different angular momenta. For instance, a perfect quadrupole mode would appear evenly and symmetrically distributed along

each quadrant of the spherical surface. The fact that the distribution is skewed, as can be seen in the left panel of Figure 5.6, is caused by the admixture of a dipole component polarized along the horizontal direction. Since the plasmon resonant peak amplitude is directly proportional to the square of the dipole moment, the quadrupole and octupole modes are enhanced due to the introduction of the dipole interaction and the added dipole components, whereas the dipole mode will have a lower peak owing to the interaction with the multipolar modes and a reduction of the dipole component. Additionally, the degree of asymmetry of the charge distributions for the multipolar modes directly implies the amount of the dipole moment that has been added to the mode. The 2d mode appears to be more asymmetrical in a quadrupole sense than 3d in an octupole sense, suggesting that 2d has a larger dipole moment. This is better revealed in the spectrum in Figure 5.5 where 2d has a higher amplitude than 3d.

5.5.2 Axial polarization

When the incident light is axially polarized, the surface charge distributions exhibit distinct characteristics despite spectral similarities to the transverse polarization case. As shown in the right panel of Figure 5.7, the octupole and quadrupole distributions appear as whole rings instead of half rings across the entire particle. A larger dipole moment can be recognized in 3d′ and 2d′ as the charge distributions become more dipole-like. Meanwhile, the dipolar distributions in 1d? also appear distorted, indicating a large multipolar interaction, which attenuates and red shifts the resonant peak. Because the overall degree of asymmetry is larger in Figure 5.7 than in Figure 5.6, I conclude that the mode hybridization due to symmetry breaking is stronger when the light is axially polarized. This explains the overall red shift from 1d, 2d,

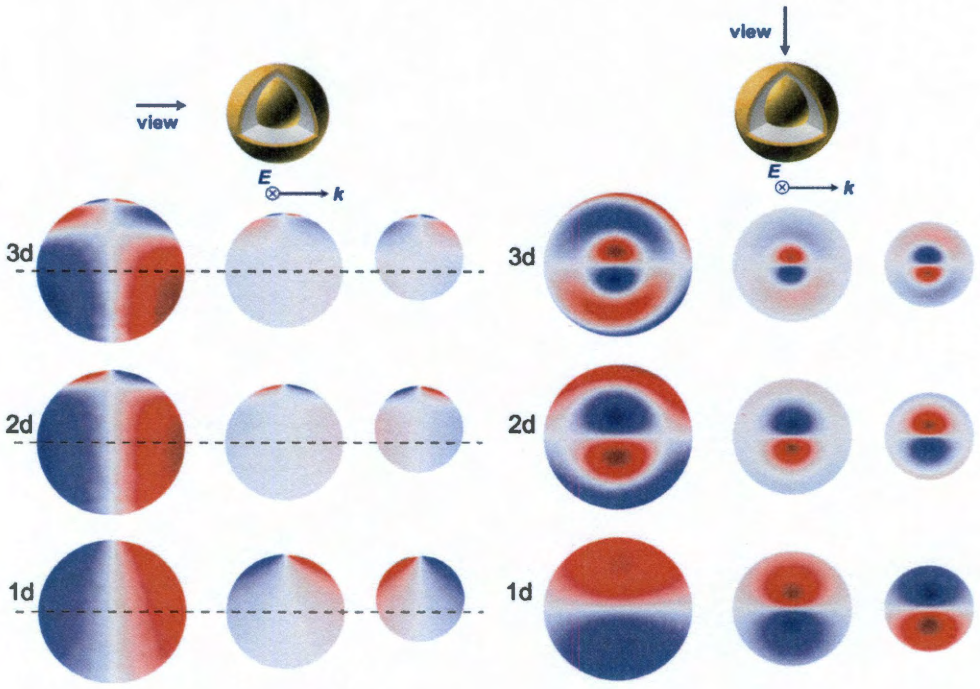

Figure 5.6 : Side (left) and top (right) views of the surface charge plot of R30/40/50 nm MNS with 9 nm core offset at various hybridized plasmon peaks as the incident light is transversely polarized with respect to the offset. The three columns correspond to the outer gold shell (left), inner gold shell (middle), and inner gold core (right) layers. Red: positive charges; blue: negative charges. Horizontal dashed lines in the left panel mark the center location with respect to the core offset.

and 3d to 1d′, 2d′, and 3d′, and also the higher amplitudes at 1d′, 2d′ versus 1d, 2d and the lower amplitude at 3d′ versus 3d, as previously described. It is worth noting that due to the relatively large size of the particle (100 nm), the retardation from the propagating electromagnetic wave comes into play. For instance, in the right panels of Figure 5.6 and 5.7, the left-right asymmetry of the charge distribution for the octupole modes reveals this retardation effect. Waves travel in slightly different phase across the particle along the direction of the propagation (indicated by the k vector), which yields a slightly asymmetric charge distribution.

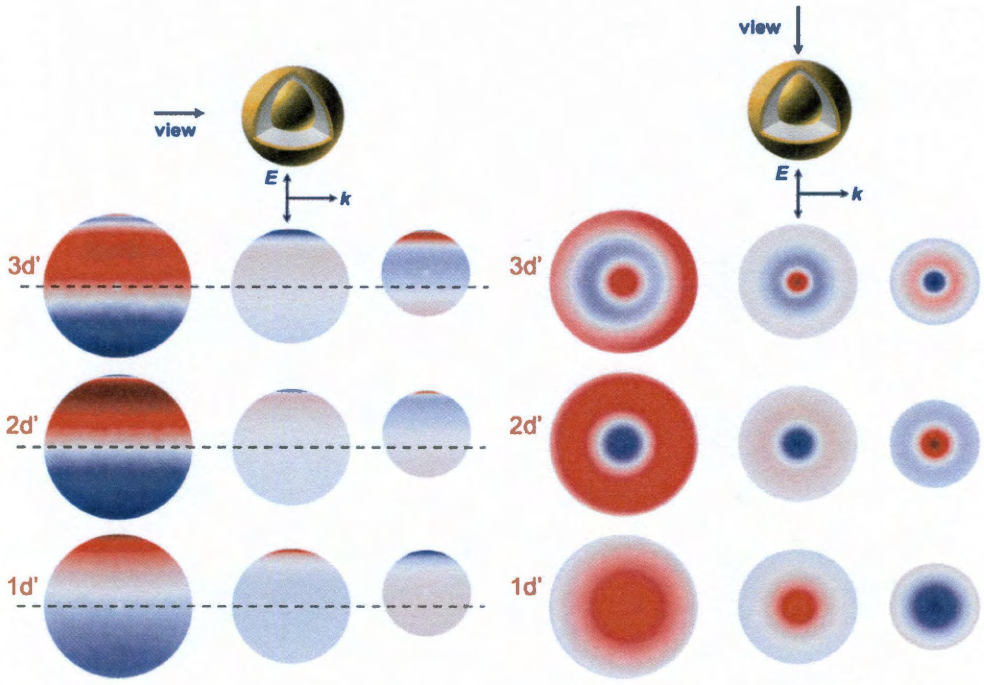

Figure 5.7 : Side (left) and top (right) views of the surface charge plot of $R30/40/50$ nm MNS with 9 nm core offset at various hybridized plasmon peaks as the incident light is axially polarized along the offset. The three columns correspond to the outer gold shell (left), inner gold shell (middle), and inner gold core (right) surfaces. Red: positive charges, blue: negative charges. Horizontal dashed lines in the left panel mark the center location with respect to the core offset.

5.5.3 Circular polarization

When MNS are excited by circularly polarized light (see Figure 5.8), the surface charge distribution is a hybrid between the two types described above. The distributions not only appear distorted along the direction of the core offset, but also become skewed around the spherical surface. The basic analysis, however, falls in the discussions for the axial and transverse polarizations.

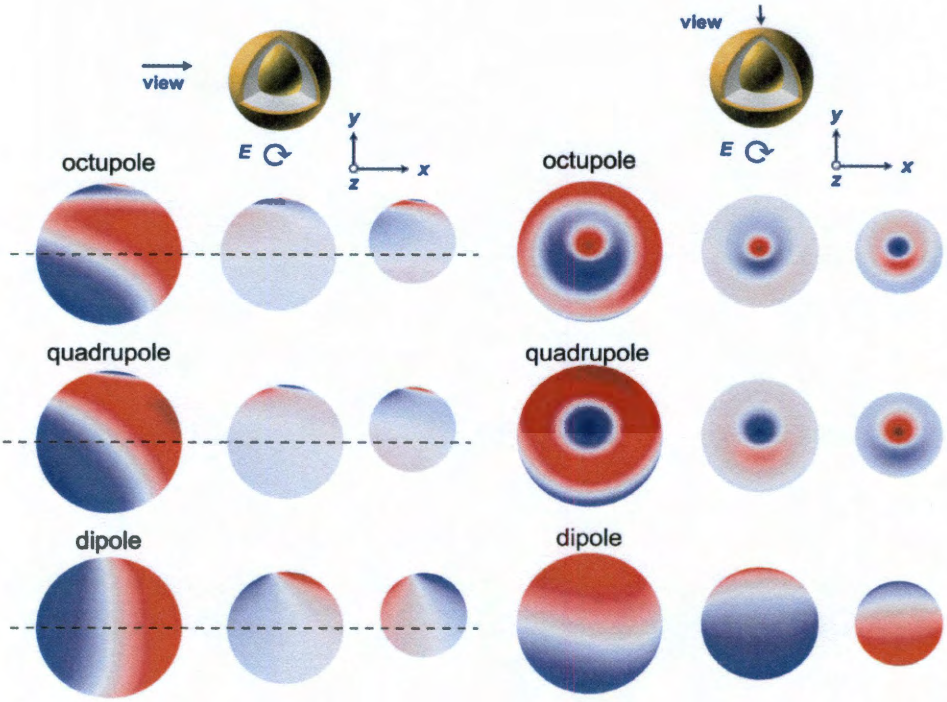

Figure 5.8 : Side (left) and top (right) views of the surface charge plot of $R30/40/50$ nm MNS with 9 nm core offset at various hybridized plasmon peaks as the incident light is circularly polarized. The three columns correspond to the outer gold shell (left), inner gold shell (middle), and inner gold core (right) surfaces. Red: positive charges, blue: negative charges. Horizontal dashed lines in the left panel mark the center location with respect to the core offset.

5.6 Absorption relative to scattering

In concentric MNS, an increase of the gold core in an otherwise fixed geometry red shifts the dipolar bonding mode and renders the particle more absorbing than scattering at the plasmon resonance [Hu et al., 2008a]. It is thus of interest to investigate how the absorption of MNS changes with respect to scattering as a function of the core offset. I chose to focus on the dipolar and quadrupolar peaks and compare the absorption and scattering components of overall extinction. It is important to note that the wavelengths of peak values for absorption and scattering are slightly offset

from each other. This is manifested not just in the FEM calculations of offset geometries, but also in the Mie-based calculations of concentric geometries. The $R30/40/50$ nm MNS with a 9 nm offset and excited by transversely polarized light has an extinction peak at 886 nm, while the absorption peak is at 885 nm, and the scattering peak at 889 nm. The offset is noticeable in Figure 5.9. The offset value, however, is small enough so the actual scattering and absorption values do not change very much. For consistency I used the absorption and scattering values at the peak extinction wavelength for the comparisons in Figure 5.10 (a) and (b).

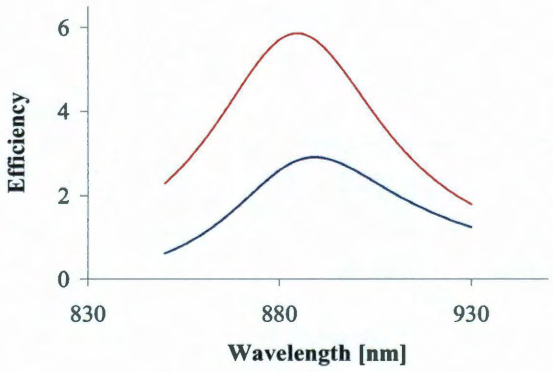

Figure 5.9 : Mie-based calculation of the absorption (red) and scattering (blue) spectra of the concentric $R30/40/50$ nm MNS in water near the dipolar resonance.

From Figure 5.10(a) it is clear that both scattering and absorption decrease with increasing offset, and the particle becomes more absorbing relative to scattering at the dipole peak. The scattering component steadily decreases and becomes almost insignificant at large offsets. The quadrupolar peak, shown in Figure 5.10(b), is more complicated as the scattering first increases and then decreases after the 8 nm offset. Although with the decreasing scattering, the overall extinction continues to increase

due to the rapidly growing absorption. The stronger absorption of the metal is mainly caused by a larger field confinement within a smaller volume (*i.e.* the reducing gap between the core and the shell). These general trends are also seen in a $R20/30/50$ nm MNS. Overall, our results show a general trend toward a larger absorption component in the extinction peak as the core offset increases.

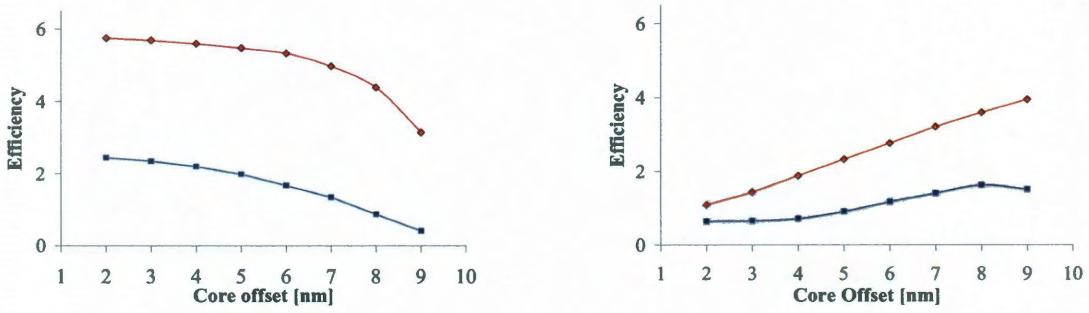

(a) (b)

Figure 5.10 : FEM calculation of the absorption (red) and scattering (blue) efficiency of the R30/40/50 nm MNS with a variable core offset in water (a) at the dipolar resonance, (b) at the quadrupolar resonance. Incident light transversely polarized.

5.7 Summary

In this chapter I used the plasmon hybridization theory to demonstrate that an offset of the core in an MNS allows interactions between plasmon resonances of different angular momenta. The mixing of modes allowed by the broken symmetry introduces a dipolar characteristic into higher order multipolar modes and makes them visible in the extinction spectra. I presented qualitatively using a hybridization diagram and quantitatively using FEM calculations red shifts of the bonding plasmon modes as

well as the emergence of the multipolar modes in the offset MNS. While polarization has little effect on the extinction spectra, I demonstrated that different polarizations create distinctly different surface charge distributions. I decomposed the extinction spectra into scattering and absorption and found that MNS tend to have a larger absorption component relative to scattering as the core offset increases. I postulate that offset MNS with larger dimensions will exhibit more interesting multi-wavelength plasmon resonances that are associated with even higher order modes. Assuming methods for large-scale synthesis can be developed, such particles may become valuable for multiplexed imaging. The distinctive spectral properties of MNS and their sensitivity to the core offset can also be harnessed to provide proof-of-concept studies for tracking intracellular movements of vessels and capsules that contain gold nanoparticles.

Chapter 6

Anti-reflection coating for improved optical trapping*

While in chapters 2 and 3, I showed that the Mie-based code can be used to calculate the optical properties of solid gold colloids, two-layer and tri-layer nanoshells, in the following chapters, I switch directions slightly and use the code to study non-plasmonic structures and secondary structures generated by plasmonic gold nanoparticles. In this chapter, I investigate the reduction of scattering by coating dielectric spheres with anti-reflection layers. In the next chapter, I probe optical amplification of photothermal bubbles generated by gold nanoparticles.

An anti-reflection coating improves optical trapping by reducing the scattering force. The improvement allows strong trapping of high-index particles that normally cannot be trapped. It also lowers the numerical aperture of the objective used for trapping. In this study, I show that the improvement is not overly sensitive to the refractive index or thickness of the coating.

6.1 Background on optical trapping

Even in the earliest work on optical tweezers [Ashkin et al., 1986], it was realized that the reflectivity of high refractive index particles limited trapping outside the Rayleigh regime. While the gradient force that is responsible for trapping is symmetric about

*Adapted from Y. Hu, T. A. Nieminen, N. R. Heckenberg and H. Rubinsztein-Dunlop, Antireflection coating for improved optical trapping, *J. Appl. Phys.* **103**(9), 2008.

the focal plane, the so-called "scattering" force is always directed in the direction of propagation of the beam and, beyond the focal plane, opposes trapping. Thus, the strength of the trap is limited by the axial force in this region where these two forces are in opposition to each other (see Figure 6.1).

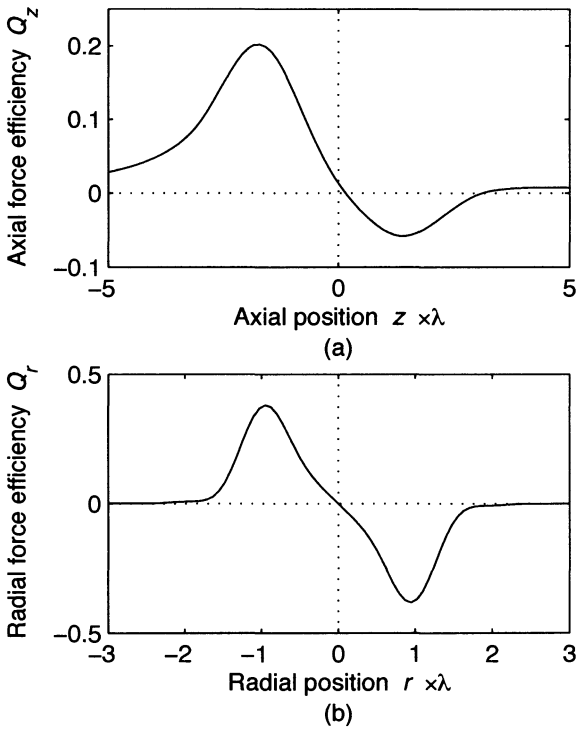

Figure 6.1 : Axial (a) and radial (b) force in optical tweezers as a function of displacement from the focus. Note the asymmetry in the axial force due to the scattering force adding to the gradient force before the focal plane, and opposing the gradient force after the focal plane.

In general, there are three distinct optical forces acting in optical tweezers. All three forces arise from scattering of the trapping beam by the particle in question, but are conceptually distinct. Firstly, the gradient force is mainly responsible for trapping. For a small (i.e., Rayleigh) particle, the gradient force is proportional to $\nabla|\mathbf{E}|^2$, where $|\mathbf{E}|$ is the electric field amplitude. For Rayleigh particles, the gradient

force is also proportional to the polarisability, and hence the volume of the particle.

For larger particles, the origin of the gradient force can be understood in terms of the particle acting as a weak positive lens, reducing the divergence of the forward-scattered (i.e., transmitted) beam. If we decompose the trapping beam into rays, each ray, of power P, and hence momentum flux of magnitude $n_{\text{medium}}P/c$, where c/n_{medium} is the speed of light in the medium, only contributes the vector component of this momentum that is directed along the beam axis to the total momentum. Because a tightly focused beam carries less axial momentum than a more parallel beam, as light is made more parallel by the particle, the increase in beam momentum results in a force acting opposite to the direction of propagation. This attracts the particle towards the beam focus. In practical applications, this restoring force is usually maximized by using a high numerical aperture (NA) objective to focus the beam as tightly as possible, to produce the largest possible axial intensity gradient, before it impinges upon the particle.

The second force, known as the scattering force, is the result of backscattering or large-angle scattering of the trapping beam. When the particle is located beyond the focal plane, the scattering force acts against the gradient force and pushes the particle away from the trap. For a Rayleigh particle, this scattering force is proportional to the sixth power of its radius. Thus, for sufficiently small particles, optical trapping is readily achieved, provided the laser power is sufficient to overcome Brownian motion. Larger particles are more problematic, as the scattering force is, for most part, proportional to the reflectivity of the particle. This in turn restricts the range of relative refractive indices of particles able to be trapped to 1.1–1.3 [Nieminen et al., 2007].

The third force is known as the absorption force. It is proportional to the volume for small particles, and to the radius for large particles with small absorption. The

Ohmic heating resulting from absorption may be counter-productive, for instance, causing rapid opticution of live specimens. Proper choice of materials and wavelength may alleviate the problem, but optical tweezers are usually not suitable for the manipulation of absorbing particles.

While it is difficult to eliminate absorption forces, the control of reflectivity is a standard practice in optics, with anti-reflection coatings to reduce reflection from optical components. The addition of such coatings to high-index particles would appear plausible to improve the trapping of such particles. Firstly, the range of relative refractive indices for which trapping is effective would be greatly extended, and, sans reflection, I can expect high-index particles to be strongly trapped due to their high refractivity. This could allow the use of new materials as probe particles, or the 3D manipulation of objects currently considered impossible to trap. Secondly, since the reverse gradient force will be competing with a greatly reduced scattering force, the requirement for objectives with high numerical aperture would be significantly relaxed. This opens the possibility of integrating optical tweezers with other microscopy technologies. The optical trapping of coated spheres has been considered in the literature, for purposes other than reducing reflection, such as for applications in enzymology [Galneder et al., 2001], 3D trapping of partially silvered silica microparticles [Jordan et al., 2004], and the trapping of hollow microspheres [Ricardez-Vargas et al., 2005] and bubbles [Jones et al., 2007, Lankers et al., 1997]. Optical properties of coated spheres have also been studied outside optical trapping, for various applications ranging from from colorimetrics [Voarino et al., 2006] to cancer treatment [Lowery et al., 2006a].

Since the experimental demonstration of such a procedure could involve a significant effort, it is worthwhile to explore the potential effectiveness computationally.

For simplicity, I only consider spherical particles with uniform coatings, but I should note that coated non-spherical high-index particles are potentially useful as optically-driven micromachines.

6.2 Modeling optical tweezers and Mie theory for coated spheres

An ideal method for calculating the optical forces acting in optical tweezers is generalized Lorenz–Mie theory [Gouesbet & Grehan, 1982, Maheu et al., 1988, Lock et al., 2006], which has been widely applied to this problem [Nieminen et al., 2007, T. A. Nieminen & Rubinsztein-Dunlop, 2007, Ren et al., 1996, Neto & Nussenzveig, 2000, Mazolli et al., 2003, Lock, 2004b, Lock, 2004a, Neves et al., 2006] . It is essentially the extension of the original Lorenz–Mie theory [Mie, 1908] to non-plane-wave illumination. Since the optical forces result from the scattering of the trapping beam by the trapped particle [Ashkin et al., 1986, Nieminen et al., 2007, T. A. Nieminen & Rubinsztein-Dunlop, 2007], it is sufficient to find the incident and scattered fields, and the total rate of transfer of momentum to the trapped particle. In Lorenz–Mie theory, the incident and scattered fields are represented by their spherical wave spectra—regular and outgoing multipole waves provide a complete basis set of modes, with an amplitude (or multipole coefficient, beam shape coefficient, or expansion coefficient) corresponding to each mode. This provides a tremendous computational advantage, since the integration of the Poynting vector in the far field (or the stress tensor) needed to find the momentum flux can be performed analytically, yielding an expression for the force in terms of products of the mode amplitudes [Nieminen et al., 2007, Farsund & Felderhof, 1996].

The amplitudes of the scattered modes are equal to the incident mode amplitudes multiplied by the *Mie coefficients*—the modes are orthogonal over a spherical surface, and the problem can be dealt with one mode at a time. The method can be readily extended in order to calculate the force on a coated sphere—extra spherical interfaces do not alter this orthogonality property.

In Mie theory for a single sphere, the boundary conditions require the tangential **E** and **H** components to be continuous across the spherical interface. This gives rise to two equations with two unknowns, the amplitudes of the internal mode and the scattered mode. The internal mode amplitude can be eliminated, giving the ratio of the scattered mode amplitude to the incident mode amplitude, which is the desired Mie coefficient. Details regarding the calculation can be found in books by van de Hulst [van de Hulst, 1981], Bohren and Huffman [Bohren & Huffman, 1983], and in Appendix A. Here, I summarize below the procedures for making the calculation for coated spheres.

The vector spherical wave functions (VSWFs) form a complete solution basis to the Maxwell equations in spherical coordinates. Any wave solution consists of a linear combination of a series summation of these VSWFs. In particular, the VSWFs **M** and **N** can be written as:

$$\mathbf{M}_{nm}^{(1,2)}(kr) = \mathbf{N}_n h_n^{(1,2)}(kr)\mathbf{C}_{nm}(\theta,\phi), \tag{6.1}$$

$$\mathbf{N}_{nm}^{(1,2)}(kr) = \frac{h_n^{(1,2)}(kr)}{krN_n}\mathbf{P}_{nm}(\theta,\phi) + N_n[h_{n-1}^{(1,2)}(kr) - \frac{nh_n^{(1,2)}(kr)}{kr}]\mathbf{B}_{nm}(\theta,\phi), \tag{6.2}$$

where $h^{(1,2)}$ are the spherical Hankel functions of the first and second kind, the normalization constant $N_n = 1/\sqrt{n(n+1)}$. $\mathbf{B}_{nm}(\theta,\phi)$, $\mathbf{C}_{nm}(\theta,\phi)$ and $\mathbf{P}(\theta,\phi)$ are the

angle-dependent vector spherical harmonics:

$$\mathbf{B}_{nm}(\theta,\phi) = \hat{\theta}\frac{\partial}{\partial\theta}Y_n^m(\theta,\phi) + \hat{\phi}\frac{im}{\sin\theta}Y_n^m(\theta,\phi) \tag{6.3}$$

$$\mathbf{C}_{nm}(\theta,\phi) = \hat{\theta}\frac{im}{\sin\theta}Y_n^m(\theta,\phi) - \hat{\phi}\frac{\partial}{\partial\theta}Y_n^m(\theta,\phi) \tag{6.4}$$

$$\mathbf{P}_{nm}(\theta,\phi) = \hat{\mathrm{r}}Y_n^m(\theta,\phi), \tag{6.5}$$

where $Y_n^m(\theta,\phi)$ are the normalized scalar spherical harmonics related to the associated Legendre functions.

The VSWFs have direct physical interpretations: $\mathbf{M}_{nm}^{(1)}$ and $\mathbf{N}_{nm}^{(1)}$ are outgoing waves (and will be used to represent the scattered wave), and $\mathbf{M}_{nm}^{(2)}$ and $\mathbf{N}_{nm}^{(2)}$ are incoming waves. It is useful to define the *regular* VSWFs,

$$\begin{aligned}\mathbf{M}_{nm}^{(3)}(kr) &= \frac{1}{2}[\mathbf{M}_{nm}^{(1)}(kr) + \mathbf{M}_{nm}^{(2)}(kr)] \\ \mathbf{N}_{nm}^{(3)}(kr) &= \frac{1}{2}[\mathbf{N}_{nm}^{(1)}(kr) + \mathbf{N}_{nm}^{(2)}(kr)],\end{aligned}$$

which due to the combination of the two terms, contain spherical Bessel functions of the first kind rather than spherical Hankel functions. The regular VSWFs are finite at the origin, and are therefore suitable to represent both the incident wave and the wave in the interior of the sphere. Polarization-wise, $\mathbf{M}_{nm}$ and $\mathbf{N}_{nm}$ denote TE and TM waves, respectively.

I consider a coated sphere with regions numbered outwards, consisting of a core (region 1), a coating layer (region 2), and the surrounding medium (region 3), as shown in Figure 6.2. For a TE mode, waves in region 3 are composed of both the

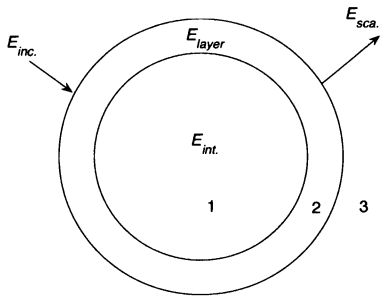

Figure 6.2 : Core–shell geometry of the system: 1—core, 2—coating layer, 3—surrounding medium.

incident and scattered fields, with

$$\mathbf{E}_3 = \sum_{n=1}^{\infty} \sum_{m=-n}^{m=n} \mathbf{M}_{nm3}^{(3)} + a_n \mathbf{M}_{nm3}^{(1)}, \tag{6.6}$$

where the scattered amplitude has been normalized to the incident amplitude, yielding a_n as the Mie coefficient of interest. The field in the coating layer consists of both incoming and outgoing waves, so that

$$\mathbf{E}_2 = \sum_{n=1}^{\infty} \sum_{m=-n}^{m=n} c_{nm} \mathbf{M}_{nm2}^{(2)} + d_{nm} \mathbf{M}_{nm2}^{(1)}. \tag{6.7}$$

The internal (core) field is written as

$$\mathbf{E}_1 = \sum_{n=1}^{\infty} \sum_{m=-n}^{m=n} e_{nm} \mathbf{M}_{nm1}^{(3)}. \tag{6.8}$$

The corresponding magnetic field $\mathbf{H}$ can be found readily, since

$$\mathbf{H} = -\frac{\mathrm{i}}{kZ} \nabla \times \mathbf{E}, \tag{6.9}$$

where Z is the impedance, and

$$\mathbf{N} = \frac{1}{k}\nabla \times \mathbf{M}. \tag{6.10}$$

Since, as noted earlier, the tangential components of **E** and **H** are continuous across the boundaries, and in all regions 1–3, the angular dependence in each of the equations above is identical, only the non-angle dependent tangential part of the VSWFs needs to be retained, namely

$$\mathbf{M}^{\tan} = N_n h_n^{(1,2)}(kr) \tag{6.11}$$

$$\mathbf{N}^{\tan} = N_n[h_{n-1}^{(1,2)}(kr) - \frac{n h_n^{(1,2)}(kr)}{kr}] \tag{6.12}$$

for our boundary conditions. Note that the boundary conditions for **H** will involve the impedance Z.

Two equations (the tangential field for **E** and **H** for each side being equal at the interface) at each of the two interfaces give four boundary conditions, which can be readily solved numerically for the four unknowns, a_n, c_{nm}, d_{nm}, and e_{nm}. Of these, the Mie scattering coefficient a_n is of most interest. By swapping **M**s and **N**s, the same procedure is followed for the TM modes, giving the TM coefficients b_n.

In practice, the infinite summation is terminated at some value $N_{\max}$. $N_{\max}$ is on the order of kr where k is the wavenumber in the surrounding medium and r is the outer radius of the sphere. For an incident plane wave, or an incident Gaussian beam as used in optical tweezers, with the sphere on the beam axis, m only takes the values of ± 1.

The computational advantage of this method is that the linear system of equations

can be readily solved by standard packages such as MATLAB. A routine calculating the coefficients for a layered sphere was developed and used with our optical tweezers modeling software [Nieminen et al., 2007] to calculate forces on coated spheres.

6.3 Trapping for spheres with and without ideal anti-reflection coatings

The medium was assumed to be water with $n_{\text{medium}} = 1.34$. A high-index glass was chosen to give an $n_{\text{sphere}} = 1.80$. Since the objective is to test the effectiveness of an anti-reflection coating, the coat index was set to $n_{\text{coat}} = (n_{\text{medium}} n_{\text{sphere}})^{1/2}$, and its thickness to $\lambda_{\text{coat}}/4$, which would make the layer an ideal *planar* anti-reflection coating.

The optical force was calculated as a function of axial position along the beam axis, and radial position for transverse displacement from the equilibrium position (where particles can be stably trapped). The trapping beam was Gaussian with a convergence half-angle of 50°, which would be produced by an optimally filled objective of numerical aperture 1.0.

The strength of the trap can be determined by finding the maximum reverse restoring force (i.e., the maximum axial force acting opposite to the direction of propagation—the point in Figure 6.1 where the force is most negative). The dependence of the trapping strength on particle size is shown in Figure 6.3. The force is given in terms of the dimensionless force efficiency; the actual force is equal to $n_{\text{medium}} P/c$, where P is the laser power in the trap. The force on an uncoated sphere with the same radius as the core is given for comparison.

Figure 6.3 indicates that uncoated spheres cannot be trapped at all sizes. Whether

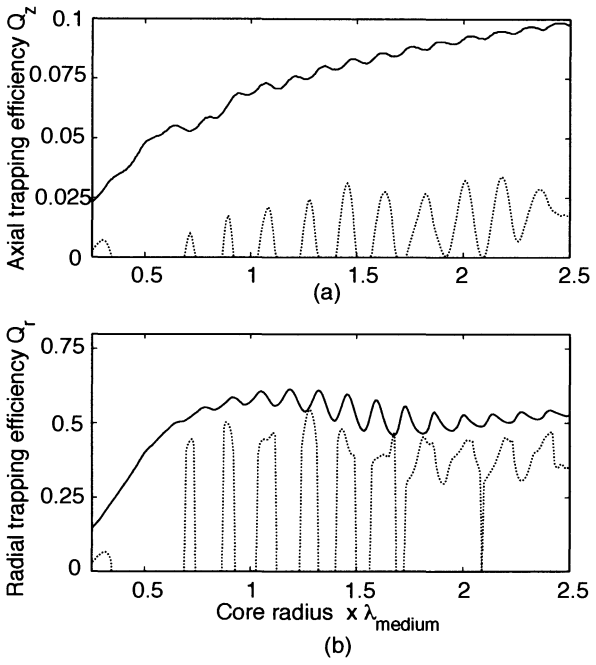

Figure 6.3 : Maximum axial reverse force efficiency (a) maximum radial restoring force efficiency (b) for coated (solid) and uncoated (dotted) high-index ($n = 1.8$) spheres.

or not it can be trapped depends on whether light reflected from the front and back surface interferes constructively, enhancing the scattering force, or destructively, reducing it [Nieminen et al., 2007]. Coated spheres, on the other hand, can be trapped regardless of their radius. The trapping becomes stronger for larger particles. Compared with uncoated spheres, the enhancement brought by the coating is over threefold in the axial direction and relatively small in the transverse direction. The same interference effect can still be seen for coated spheres, but in a greatly reduced fashion.

A natural question to follow is: can a similar improvement be obtained for a more conventional particle with lower refractive indices? The same procedure was repeated for polystyrene beads with $n_{\text{sphere}} = 1.59$. As shown in Figure 6.4, the improvement in axial trapping is about 50%. Again, the radial efficiency is slightly enhanced.

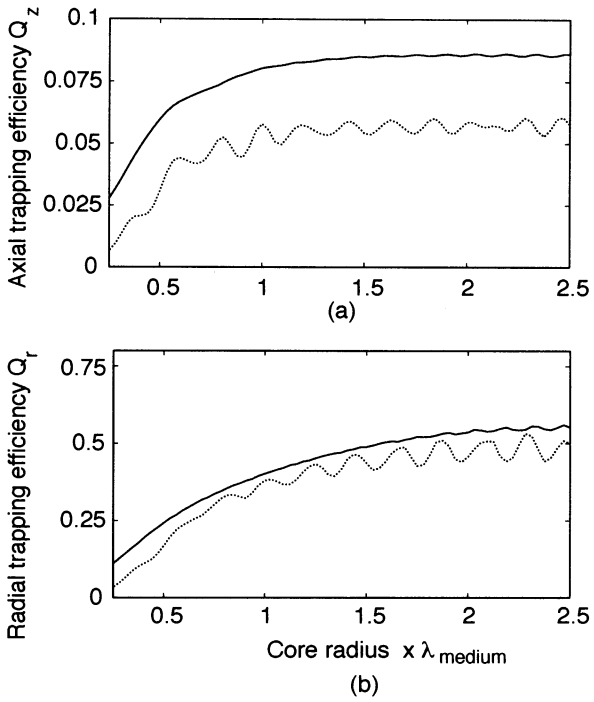

Figure 6.4 : Maximum axial reverse force efficiency (a) maximum radial restoring force efficiency (b) for coated polystyrene spheres (solid) and uncoated polystyrene spheres (dotted).

The trend is consistent with the observation on Figure 6.3. Essentially the coating functions as a buffer region to reduce the index gradient between the core and the medium. As the refractive index of the sphere becomes closer to that of the medium, the advantage provided by the coating gradually diminishes. In a special case where $n_{\text{coat}} = n_{\text{sphere}}$, the addition of the coating does not alter any optical properties of the particle except augmenting its size, which, from Figure 6.4(a) and (b), does not provide significant added benefit to the trapping. Although the enhancement is not as drastic as in the high index material, particles with lower indices also pose less challenge for conventional optical trapping.

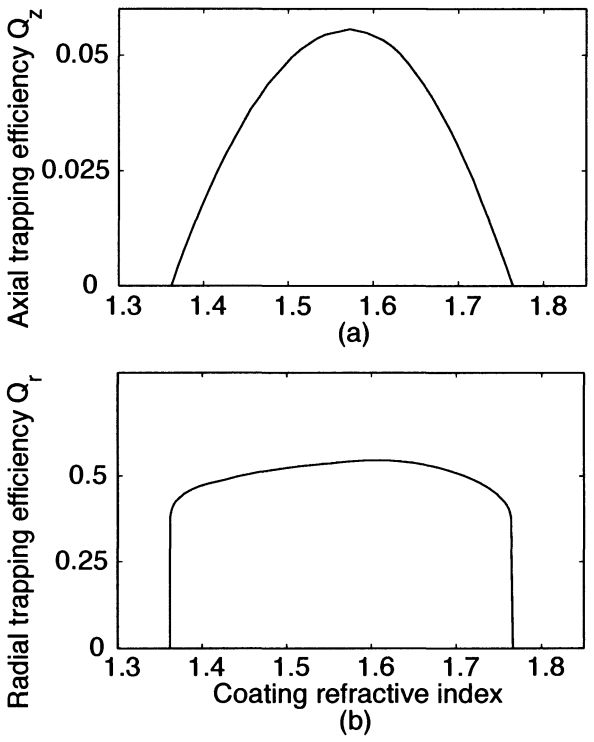

Figure 6.5 : Axial (a) and radial (b) force on a coated high-index ($n_{\text{sphere}} = 1.8$) sphere of core radius $0.75\lambda_{\text{medium}}$, as the refractive index of coating varies.

6.4 Trapping for spheres with coatings with various refractive indices and thicknesses

The above results are for a coating of the expected-to-be-ideal refractive index and thickness. It is also prudent to probe how much of an improvement can be obtained if the refractive index and thickness deviate from these ideal values. In Figure 6.5, the layer index is varied while the layer thickness is kept at $\lambda_{\text{coat}}/4$. When the refractive index departs from the ideal value, the strength of the trap decreases smoothly, until the coat index is close to that of either the medium (1.34) or the sphere (1.80). Strong trapping is achieved over a range of refractive indices varying by more than 0.15 on either side of the ideal value. This suggests having a coating material with a refractive

index very close to the ideal value is not crucial for trapping enhancement.

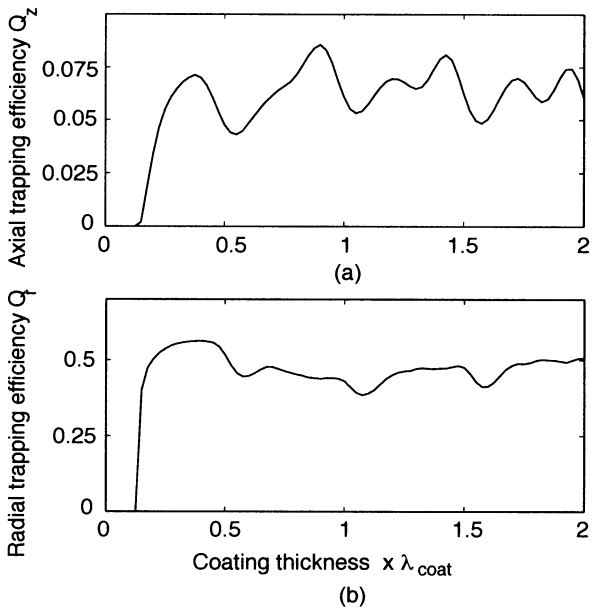

Figure 6.6 : Axial (a) and radial (b) force on a coated high-index ($n_{\text{sphere}} = 1.8$) sphere of core radius $0.75\lambda_{\text{medium}}$, as the thickness of coating varies.

The effect of variations in coating thickness is shown in Figure 6.6. Here the refractive index of the coating material is kept at $n_{\text{coat}} = [(n_{\text{sphere}})(n_{\text{medium}})]^{1/2}$ while the coating thickness is varied. As reflected light from the inside and outside surfaces alternates between destructive and constructive interference, the corresponding maxima and minima can be observed in trapping strength. However, rather than projected exactly at multiples of one-quarter wavelength, peaks and valleys reside in the neighborhood of these locations. The first maximum in the axial direction, for instance, occurs at a coat thickness of $0.375\lambda_{\text{coat}}$, and the second, larger, maximum occurs at $0.9\lambda_{\text{coat}}$. This may be due to the complex situation in which light is reflected from a sphere rather than from a planar structure. In addition, as long as the coating thicknesses is greater than $0.15\lambda_{\text{coat}}$, the enhancement in trapping efficiency

is roughly constant. This suggests the improvement from the coating is not overly sensitive to its thickness either.

6.5 Trapping for high-index spheres with and without anti-reflection coatings under various numerical apertures

Lastly, NA was studied as a variable parameter. The aim is two-fold: firstly, to show how NA affects the trapping efficiency, and secondly to see whether or how much the coating technique would relax the hardware requirement on objectives. Figure 7.3 plots the results in the radial and axial directions. For the radial trapping, the efficiency reaches a maximum between NA = 0.8 and 1.3. Coated spheres achieve higher efficiency than their bare counterparts at all NAs. Meanwhile, the axial trapping increases monotonically with NA, attributed to the larger changes in light momentum as discussed earlier. Moreover, coating provides considerable improvement, allowing relatively low numerical apertures to achieve axial trapping strength that would not be achieved with uncoated particles unless a larger NA objective is used. This could in turn effectively alleviate the hardware limitations. For instance, the strenght of axial trapping of a bare glass particle using NA $\sim$ 1.15 can be achieved with NA $\sim$ 0.8 simply by coating the particle with an anti-reflection layer.

6.6 Summary

In summary, based on detailed calculations, the coating of high-index spheres appears to be a promising strategy for enhancing trapping in optical tweezers by reducing the refractive-index contrast. For uncoated particles that cannot be trapped, the coating provides immediate trapping. This improvement is more prominent in the

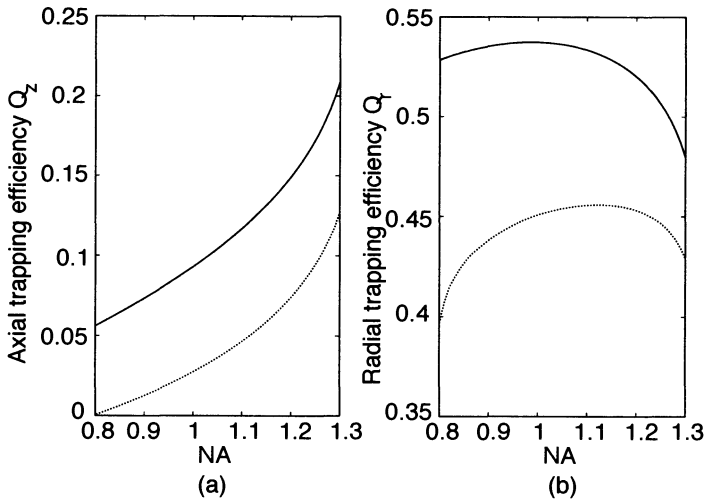

Figure 6.7 : Axial (a) and radial (b) trapping efficiency on a coated (solid) and bare (dotted) high-index ($n_{\text{sphere}} = 1.8$) sphere as NA varies. Core radius is $2\lambda_{\text{medium}}$.

axial direction than in the radial direction. Particles with a higher refractive index also benefit more from the coating than the ones with a lower index. Moreover, the improvement is relatively insensitive to either the refractive index or the thickness of the coating, which could promise a simple yet robust procedure that could become a standard practice to trap high index materials. Improved trapping also lowers the requirement on numerical aperture of the objectives. This opens possibilities to combine optical tweezers with other microscopy technologies.

Chapter 7

Enhanced scattering from photothermal bubbles*

7.1 Background on photothermal bubble (PTB)

Gold nanoparticles and gold nanoshells, as discussed in Chapter 2, have unique plasmonic properties. At plasmon resonance, these nanoparticles can strongly scatter and/or absorb light. The enhanced scattering has been explored in biomedical-imaging applications as increased contrast is created by nanoparticles between normal and targeted samples [Loo et al., 2005, Bickford et al., 2008b]. From the efficiency plot (*i.e.*, Figures 2.3 and 2.3), one can observe that gold nanoparticles and nanoshells can have scattering cross-sections a few times (*i.e.* 3–8×) larger than the physical cross-sections. The main challenge of using gold nanoparticles and nanoshells for scattering-based applications is sensitivity. Because tissues are highly heterogeneous media, photons become randomized quickly. Scattering from nanoparticles can be detected only when the concentration of the nanoparticle reaches above certain threshold (*i.e.*,1×10^9 *particles / ml*). Here I computationally investigate an absorption-based imaging technique where photothermal bubbles are created by super-heating nanoparticles in water. Photothermal bubbles may possess scattering properties a few orders of magnitude stronger than gold nanoparticles and nanoshells alone.

---

*Adapted from E. Lukianova-Hleb, Y. Hu, A. Volkov, L. Zhigiley, S. Lee, R. Drezek, J. Hafner and D. Lapotkp, Plasmonic nanobubbles as transient vapor nanobubbles generates around plasmonic nanoparticles, *ACS Nano* **4**(4), 2010. E. Y. Hleb, Y. Hu, R. A. Drezek, J. H. Hafner, and D. O. Lapotko, Photothermal bubbles as optical-scattering probes for imaging living cells, *Nanomed.* **3**(6), 2008.

7.2 Experimental setup to generate PTB

Figure 7.1 shows a schematic of the PTB generation. Briefly, a short-pulsed pump laser is overlaid with a low-power probe continuous wave (c.w.) laser. The super-heating of gold nanoparticles evaporates vapor around the particles. The expansion of the vapor layer eventually develops into transient air bubbles. The life- time of the bubble depends on the fluence of the pump laser and is typically in the range of 10-1000 ns. The air bubble eventually collapses due to surface tension of water. Using lock-in mechanism, the scattering from these PTBs can be measured from the probe laser by either measuring side-scattering or forward-scattering intensity.

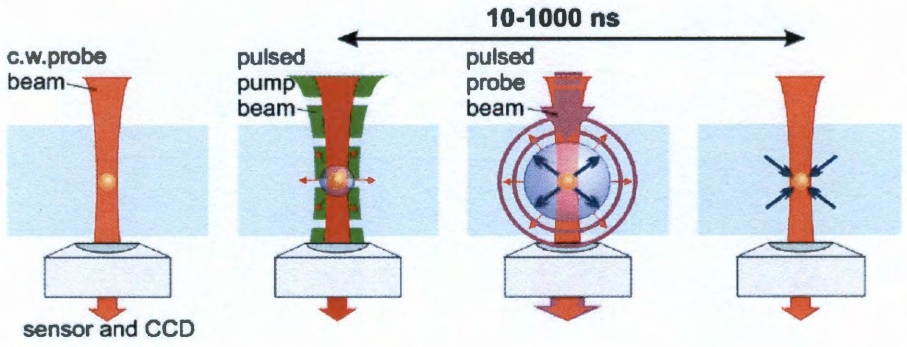

Figure 7.1 : Schematic diagram showing the generation of PTB [Lukianova-Hleb et al., 2010].

Figure 7.2 shows a block diagram of the experimental setup constructed by our collaborator. A short-pulse laser at 532 nm with 10-ns pulses was focused onto gold nanoparticles (with a fluence of 0.45 J/cm^2). The pulse width is shorter than the thermal diffusion time in water so sub-micron nanobubbles can be generated. In addition, the wavelength was chosen to overlap with the plasmon resonant wavelength of gold nanoparticles to maximize the heating effect. Time-response of PTB was registered with a continuous probe beam at 633 nm [Hleb et al., 2008]. The dynamics

of the PTB was measured by a shift of the beam phase that affects the intensity of the beam. Side images was obtained with a 750-nm laser with the same pulse rate as the 633-nm laser [Hleb et al., 2008].

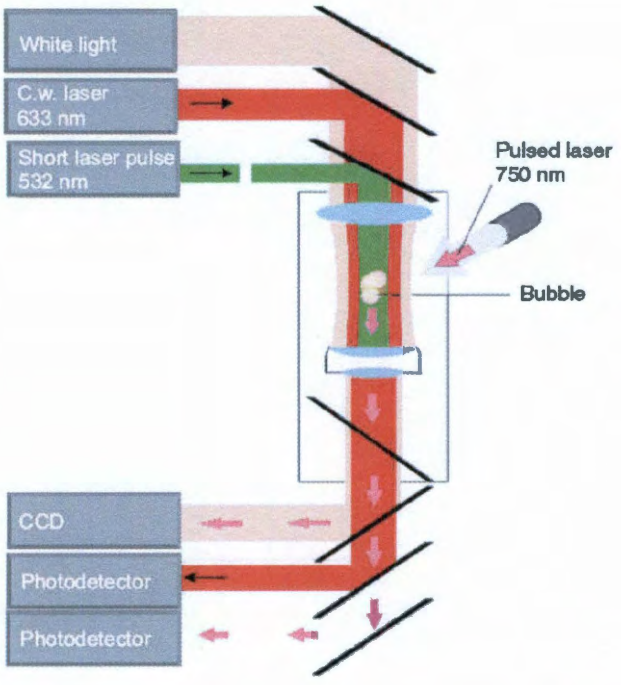

Figure 7.2 : Experimental setup to generate PTB [Hleb et al., 2008].

Experimentally observed is a direction relationship between the life-time and intensity of the PTB. A larger pump fluence results in a larger PTB that lasts longer and scatters more strongly. In Figure 7.3, the left panel shows a side-scattering of the 30-nm AuNPs in water with the probe laser, the right panel shows the same area after the pump laser was applied at 0.45 J/cm^2. A much stronger scattering was clearly observed and it was found that the enhancement can be as large as three orders of magnitude [Hleb et al., 2008].

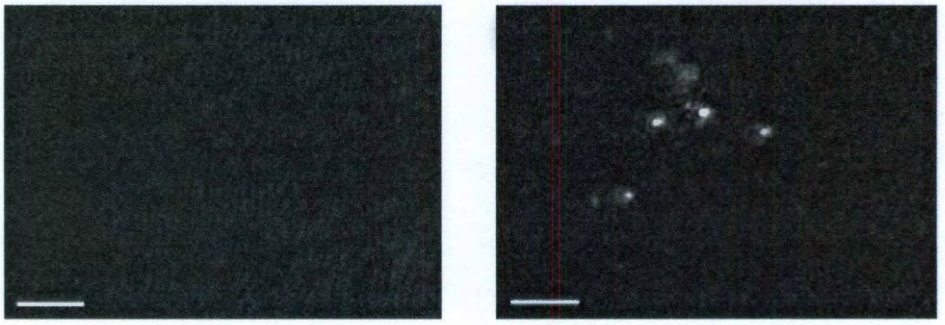

Figure 7.3 : Optical detection of the side scattering of PTB. Scale bar is 10 μm [Hleb et al., 2008].

7.3 Mie modeling of optical amplification of PTB

I use the Mie code for concentric spheres to model light scattering from bubbles generated around gold NPs. Subject to general limitations of Mie calculations, the assumptions made here are that NPs and bubbles are rigidly spherical in shape; bubbles are perfectly centered on NPs and the illumination is along a plane wave.

Owing to the nonabsorbent nature of the bubbles, the scattering cross-section (C_{sca}) is an effective figure of measurement for their optical properties. The differential scattering cross-section, $\delta C_{sca}/\delta\Omega$, is defined as the time-averaged energy projected into a unit solid angle, $\delta\Omega$, at a direction, $\hat{\Omega}$. It is expressed in terms of scattered irradiance, I_s, incident irradiance, I_i, and distance, r, from the center of the sphere to the detector:

$$\frac{\delta C_{sca}}{\delta\Omega} = r^2 \frac{I_s}{I_i}. \tag{7.1}$$

By integrating over all solid angles, Ω, one obtains the C_{sca}, which, from the definition above, is also equal to the percentage of scattered power in all directions with respect to the incident power multiplied by r^2 . Therefore, given C_{sca} and r, the

percentage of total scattered power can be obtained. Based on Mie coefficients a_n and b_n derived from the aforementioned code, C_{sca} can be calculated (See Equation A.36 in Appendix A). The detector distance r can be estimated from the experimental setup.

Figure 7.4 plots the total scattered power for a gold sphere with a diameter of 30 nm and a silica-gold NS with an outer diameter of 170 nm and a gold-layer thickness of 8 nm, each NP surrounded by the single air bubble suspended in water. Of note is the general trend of increase in scattering against PTB radius. This can be understood qualitatively from Rayleigh scattering as already has been discussed in Chapter 2. Compared with the scattering from the NPs, PTBs could potentially produce many orders of magnitude amplification in scattering intensity. As air bubbles grow larger, the effect of the particles enclosed diminishes, as can be seen on the 30-nm NP curves versus the 170-nm NS curves. For example, the scattering from a 600-nm bubble that encloses a 30-nm gold NP, and a 600-nm bubble that encloses a 170-nm gold NS gives a nearly identical value of scattered signal. When the bubble becomes comparable to or larger than a particular wavelength, this growth slows down significantly.

One may observe an initial dip in scattering of the 30-nm gold NP. I attribute this phenomenon to two causes. First, the formation of the vapor layer lowers the refractive index of the media immediately surrounding the nanoparticle. This change in the media blue shifts the plasmon resonance of the gold NP and causes the heating efficiency to go down. Meanwhile, the lowering of refractive index of the media also lowers the scattering cross-section of the particle. Second, I suspect that before the complete formation of PTB, the media around gold NP are a mixture of water vapor and air. This mixture layer effectively behaves as an anti-reflection layer (*i.e.*, as discussed in Chapter 6). The intermediate layer smoothes out the discontinuity

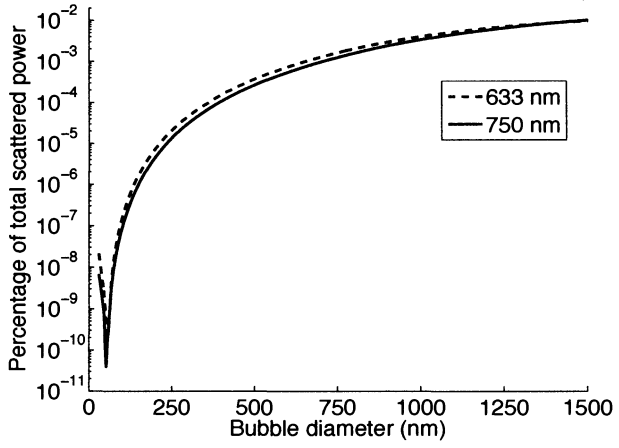

(a)

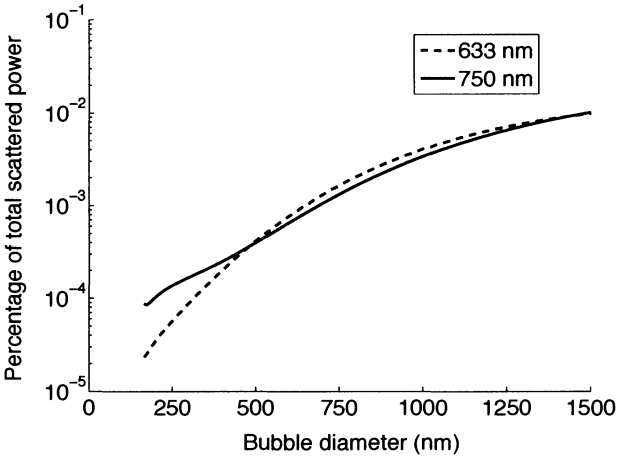

(b)

Figure 7.4 : Theoretical modeling of the amplification of optical side scattering by the air bubble surrounding a 30-nm gold sphere and a 170-nm silica-gold shell as a function of the bubble diameter.

between gold NP and water and thus reduces scattering. This transient reduction in scattering has also been observed experimentally [Lukianova-Hleb & Lapotko, 2009].

7.4 Summary

Following the previous chapter that describes a Mie-based modeling to show a reduction of scattering and increase in optical trapping for coated spheres, in this chapter I demonstrated a theoretical and experimental investigation on the optical amplification of photothermal bubbles created by gold nanoparticles and nanoshells. I found that, although gold nanoparticles possess strong plasmon resonance, their scattering cross-sections are still much smaller than non-plasmonic structure (*i.e.* air bubbles) that are many times larger. Due to the fact that Rayleigh scattering increases as the sixth power of the size of the particle (equation 2.2), the increase in scattering is substantial if an increase in size of the structure can be achieved. PTBs provide a smart approach to deliver nano-size gold particles into cells and generate on-demand extremely bright scattering bubbles for imaging and/or destruction of the cells.

Chapter 8

Enhanced Raman scattering from nanocone substrates decorated with gold nanoparticles*

In this chapter, I use the finite-element method (FEM) to investigate the near-field electromagnetic (EM) enhancement from the coupling between two nanostructures. The subject to be discussed is different from previous chapters in two aspects. First, the near-field enhancement is different from far-field properties (*i.e.*, scattering and extinction). Using Mie approach to investigate near-field properties is cumbersome due to the complex nature of VSWFs' dependency on radius r(recall the far-field approximations made in equations A.41 and A.42)). In addition, the complex geometrical features of the nanocone cannot be calculated using Mie theory. Thus, the simulation work presented here is purely numerical in nature. Second, in elastic scattering (*i.e.*, scattering from nanoparticles), energy of the incident light is preserved (*i.e.*, the incident and scattered light have the same wavelength). However, Raman scattering is an inelastic process (*i.e.*, the Raman scattered light has different energy levels than the excitation light). I study the near-field properties that enhance Raman scattering.

---

*Adapted from Ying S. Hu, Jaeseok Jeon, Tae J. Seok, Seunghyun Lee, Jason H. Hafner, Rebekah A. Drezek, and Hyuck Choo, Enhanced Raman scattering from nanoparticle-decorated nanocone substrates: a practical approach to harness in-plane excitations, *ACS Nano*, in press, 2010

8.1 Background on Raman scattering and surface-enhanced Raman scattering (SERS)

Inelastic scattering by a molecule can provide unique information about the vibrational states of the molecule. Named after C. V. Raman for his discovery in 1928 [C. V. Raman, 1928], Raman scattering has attracted numerous research interests from forensic science to bio-sensing. Raman scattering provides signature spectra of molecules and has the sensitivity high enough for single-molecule detection [Nie & Emery, 1997]. The main drawback of Raman scattering is it's an extremely weak scattering process, much weaker than fluorescence. In 1974, Fleischman and co-workers discovered a much enhanced Raman scattering from pyridine molecules absorbed on electrochemically roughened silver surface [Fleischmann et al., 1974]. In 1977, two group independently reported two mechanisms that explain the surface-enhanced Raman scattering (SERS). Albrecht and Creighton noted a chemical enhancement mechanism which states that the enhancement is related to the charge-transfer complex formed between the absorbent molecule and gold surface [Albert & Creighton, 1977]; while Jeanmarie and Van Duyne proposed an electromagnetic enhancement mechanism in which Raman scattering is enhanced to the fourth power of the enhanced near-field electric field excited by surface plasmon resonance [Jeanmaire & Vanduyne, 1977]. In this chapter, I explore an effective and practical approach to enhance the Raman scattering from a SERS substrate from the electromagnetic (EM) enhancement perspective.

I investigate SERS from gold-coated silicon-germanium nanocone substrates that are decorated with 30-nm spherical gold nanoparticles (AuNPs). Finite-element simulations suggest that individual nanocones generate stronger electromagnetic enhance-

ment with axial polarization (*i.e.*, polarization parallel to the vertical axis of the nanocones) than with transverse polarization (*i.e.*, polarization in the plane of the nanocone substrate), whereas the excitation in a typical Raman microscope is mainly polarized in the transverse plane. Thus, a more practical approach to improve the SERS performance of the substrate it to fill the valleys between nanocones with AuNPs. Simulations reveal enhanced electric field at the nano-scale junctions formed between AuNPs and nanocones, and this lateral coupling is explained by a hybridization model for a particle-film system. I further experimentally verify the added enhancement by measuring SERS from trans-1,2-bi-(4-pyridyl) ethylene molecules absorbed onto the substrates. An over one order-of-magnitude increase in SERS activities and a spatially averaged enhancement factor of 1.78×10^8 at 785-nm excitation have been achieved. Understanding and implementing the enhancing mechanism of structured metallic surfaces decorated with plasmonic nanoparticles open possibilities to substantially improve the SERS performance of the existing process-engineered substrates.

8.1.1 Background on SERS-substrate design

Surface-enhanced Raman scattering (SERS) has been extensively investigated on substrates formed by nanoparticles of various morphologies, compositions and plasmonic properties [Ko et al., 2008]. Gold and silver nanoparticles possess unique optical properties due to their localized surface-plasmon resonance. Morphological features, such as sharp tips and edges, are believed to create strong spatially confined electric-field enhancement, which enhances Raman scattering of the molecules in the region. Mesoscopic nanoparticles with rich geometrical features have been investigated, such as dendritic nanostructures [Shamsaie et al., 2007], nanostars [Esenturk & Walker,

2009, Khoury & Vo-Dinh, 2008], bipyramids [Lee et al., 2009], meatball-like [Wang & Halas, 2008] and flower-like [Duan et al., 2006] particles. In addition to morphological features, nanoparticles of composite structures, such as core-shell nanoshells [Hirsch et al., 2006, Oldenburg et al., 1999, Jackson & Halas, 2004], possess tunable plasmonic properties. These nanoparticles can be engineered to generate large electromagnetic field enhancement when the laser-excitation wavelength overlaps with the plasmon-resonance wavelength. A relatively new design explored core-satellite nanoparticle complexes, in which strong enhancement due to the synergistic and cascading effects was found [Gopinath et al., 2009a, Chen & Lazarides, 2009]. Lately, bimetallic nanoparticles have gained research interests due to the synergism and plasmonic tunability of the metals [Ko et al., 2008, Gunawidjaja et al., 2009, Rycenga et al., 2009, Pande et al., 2007, Rivas et al., 2000, Hu et al., 2007, Bao et al., 2008]. Individual nanoparticles have also been assembled into conjugated dimmers, trimers and aggregates [Brousseau et al., 1999, Wang et al., 2005], as well as one-dimensional nanoparticle chains [Zeng et al., 2007, Lin et al., 2005b, Yang et al., 2007], nanodisk arrays [Qin et al., 2006, Qin et al., 2007], two-dimensional nanoparticle arrays and clusters [Polavarapu & Xu, 2008, Kim et al., 2008, Liao et al., 2006, Wang et al., 2005, Hulteen et al., 1999, Tsukruk et al., 1997, Yan et al., 2009, Gopinath et al., 2009b]. Large-scale three-dimensional structures have been created by depositing plasmonic nanoparticles into non-plasmonic templates [Tessier et al., 2000, Chan et al., 2003, Ko & Tsukruk, 2008, Kondo et al., 2009].

Concurrent with the plasmonic nanoparticle studies is a vast pool of literature that discusses the fabrication of process-engineered metallic substrates. Similar to nanoparticles, nanostructured metallic substrates create strong enhancement due to their plasmonic properties. Patterned nanostructures are often created by performing

chemical and plasma etching on a supporting substrate and subsequently depositing a thin layer of gold onto the surface [Fan & Zhao, 2008, Geissler et al., 2009, Linn et al., 2009, Ruan et al., 2007, Bora et al., 2010]. A design variant creates periodic impressions instead of protruding nanostructures on thin gold films [Brolo et al., 2004, Reilly et al., 2007].

An emerging new design utilizes plasmonic nanoparticles supported by a metallic structure that also exhibits surface plasmon properties. A recent paper reported a bimetallic nanocob structure, in which silver nanowires are coated with polymer layers embedded with 4-nm gold nanoparticles (AuNPs) [Gunawidjaja et al., 2008]. While two crossing nanowires with no AuNPs exhibited noticeable Raman signal only from the intersection point (where the gap distance is small), AuNP-decorated nanowires generated the Raman signal throughout the nanowires, at an intensity that is about two orders of magnitude stronger than that of the non-decorated silver wires [Gunawidjaja et al., 2008].

Inspired by the bi-structured SERS substrates that exhibit high Raman activities, I explore here a simple and effective approach to improve SERS performance of a process-engineered nanocone substrate by decorating its surface with AuNPs. The limitations of the substrate can be diagnosed by simulating plasmonic properties of the AFM-characterized nanocone geometries at different excitation wavelengths and polarizations - the relatively weak enhancement exists with transversely polarized light. I show that this weak enhancement can be dramatically improved by adding AuNPs to the substrate and efficiently utilizing transversely polarized light. I further demonstrate strong lateral coupling created by a 30-nm AuNP situated between a pair of nanocones. The improved SERS performance is verified by measuring and comparing Raman spectra of trans-1,2-bi-(4-pyridyl) ethylene (BPE) molecules absorbed

onto the substrates with and without AuNPs.

8.2 Fabrication of nanocone substrates

The nanocone substrates was fabricated by depositing a polycrystalline silicon-germanium (SiGe) layer on a silicon (Si) wafer, followed by plasma etching. The process produced ordered nanoscale peaks, as shown in Figures 8.1(a) and 8.11(b). After dicing the wafer into 1 cm by 1 cm chips and attaching them to a handling Si-wafer, a 40-nm gold layer was evaporated onto the SiGe surface, producing the nanocone substrates shown in Figure 8.1(c). The thickness of the gold layer was measured by characterizing the step height at the borderline between the areas covered and not covered by the gold layer on the handling Si-wafer. The deposition rate of the gold evaporation process is sensitive to incident angles, with maximum at normal incidence. As a result, the tips of the nanoscale peaks are covered by a 40-nm-gold layer, and the coating thickness tapers down toward the base. Side-view images taken at 40° are shown in Figures 8.1(b) and (c) and reveal the cone-like shapes of the nanocones.

8.3 Surface topology analysis

In order to construct models that accurately represent the geometry of the nanocone, surface topologies of the nanocone substrate were characterized using atomic force microscopy (AFM) and scanning electron microscopy (SEM). The effective gold surface area and the number of analyte molecules that could form a monolayer on the substrate were estimated.

An AFM scan of the height profile on a 1-μm^2 square area is displayed in Figure 8.2(a). The y sectioning plots in Figure 8.2 (b)-(d) show three common structures: doublet nanocones denoted by triangles, isolated single nanocones denoted by blocks,

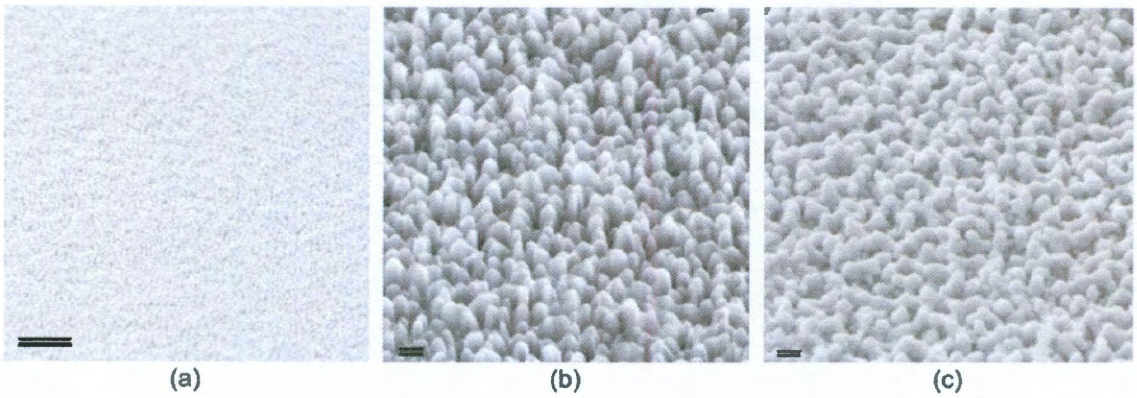

Figure 8.1 : Scanning electron microscope images of (a) a low-magnification view of ordered nanostructures fabricated on the SiGe substrate, (b) a high-magnification view of the SiGe substrate shown in (a), and (c) a side view taken at 40° of the SiGe substrate after deposition of 40 nm of gold (*i.e.*, the nanocone substrate). Scale bar is 1 μm in (a) and 100 nm in (b) and (c).

and nanocones with deep gaps denoted by circles. For SiGe nanocones, an average base radius of ~30-50 nm and a height of ~80-130 nm were measured. Dimensions of several nanocones are labeled in Figure 8.2(c) and Figure 8.2(d). Simulations employed a base radius of 40 nm (base width of 80 nm) and a height of 100 nm. The average peak-to-peak separation varies between 60 and 150 nm. The AFM analysis of the surface revealed a nanocone density of 142 peaks/μm^2. Assuming all gold surfaces on the nanocones contribute to the SERS signal and by modeling nanocones as singlet cones with the dimensions given above, the effective gold surface area per μm^2 on the substrate is approximately 1.9 μm^2.

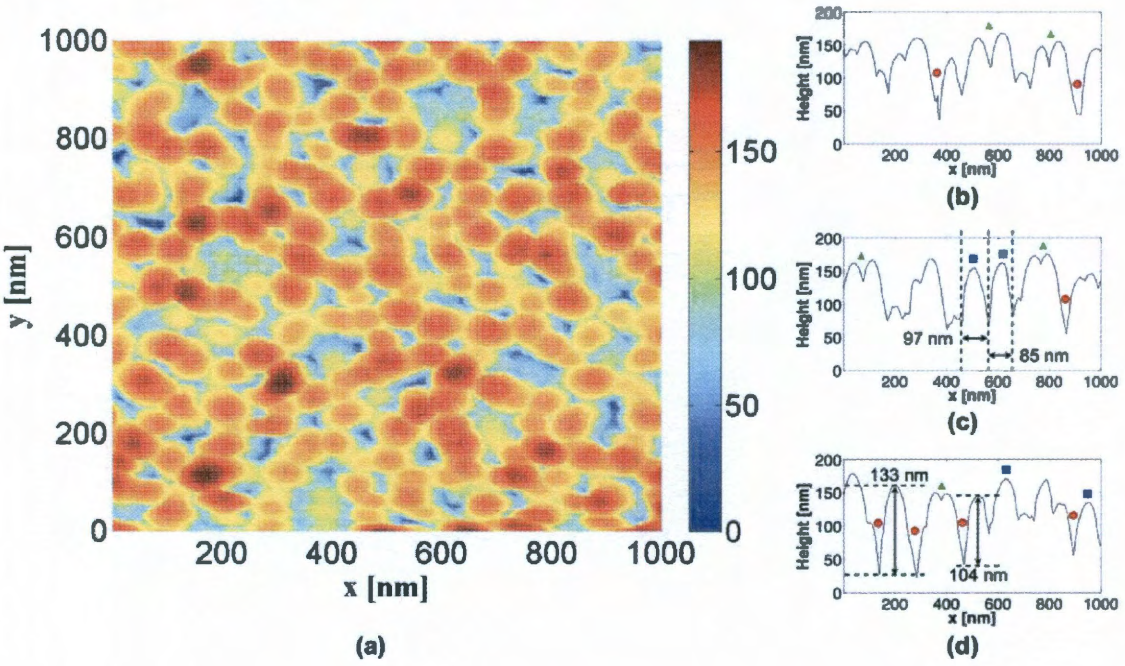

Figure 8.2 : AFM height profile of the SiGe substrate before gold deposition. (a) Height profile of a two-dimensional scan, with color bar giving the height in nm. Individual line sectioning plots (b)-(d) shows doublet peaks denoted by triangles, isolated single peaks denoted by blocks, and deep gaps between peaks denoted by circles.

8.4 Simulations on the polarization- and wavelength-dependent characteristics of the nanocone

Whereas Raman shifts are invariant with respect to the excitation energy, the strength and localization of the near-field (*i.e.* EM) enhancement of the SERS signal strongly depend on the excitation wavelength. This variation in strength and localization of the EM enhancement may cause the amplitude of certain Raman modes to be sensitive to excitation wavelength. In addition, the laser polarization plays a role in selectively exciting different modes depending on the geometry of the nanostructure. I examine herein the effects of two orthogonal polarizations of the excitation light: the excitation light polarized parallel to the vertical axis of the nanocone for axial polarization and perpendicular to the vertical axis for transverse polarization, as shown in Figure 8.3.

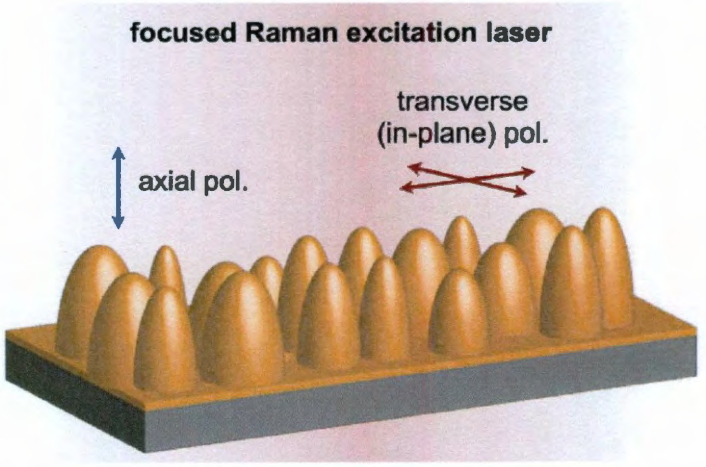

Figure 8.3 : Illustration of the axial and transverse (in-plane) polarizations of the Raman excitation light in relation to the SERS substrate.

8.4.1 Axial polarization

Figure 8.4 shows the magnitude of the normalized electric field when a nanocone is excited at four different wavelengths with axially polarized light [Figure 8.4(a)]. The dimension of the SiGe nanocone is described previously. The gold coating is 40-nm thick on the tip and tapers down to 5 nm at the base. Strong EM enhancement is generally found at the tip of the nanocone and the distribution of the electric field varies at different wavelengths. For excitation at 543 nm [Figure 8.4 (a)], the localized field is mainly focused at the gold tip of the nanocone; whereas for excitation at 1064 nm [Figure 8.4(d)], noticeable fields are developing inside the SiGe nanocone. I attribute this dependence on the excitation wavelength to plasmon hybridization of surface plasmons on the nanocone. The interplay between surface plasmons at the gold-air interface and at the SiGe-gold interface influences the localized electric field distribution.

8.4.2 Transverse polarization

The wavelength-dependent characteristic of the enhancement can also be observed when the excitation light is transversely polarized. Figure 8.5 shows this trait at the same wavelengths as are shown in Figure 8.4 . Unlike with axial polarization, the nanocone exhibits low enhancement at the tip due to the geometrical symmetry in the transverse direction. Figure 8.5(c) presents an interesting case where the section toward the base resonates at 785 nm, separately from the rest of the nanocone. This dipole-like plasmon resonance can be induced by the thin gold layer (~5 nm), which results in a strong coupling between the two aforementioned surface plasmons at 785 nm. This resonance wavelength blue shifts as the gold layer becomes thicker (*i.e.*, toward the tip of the cone). Despite the similar wavelength-dependent characteristic,

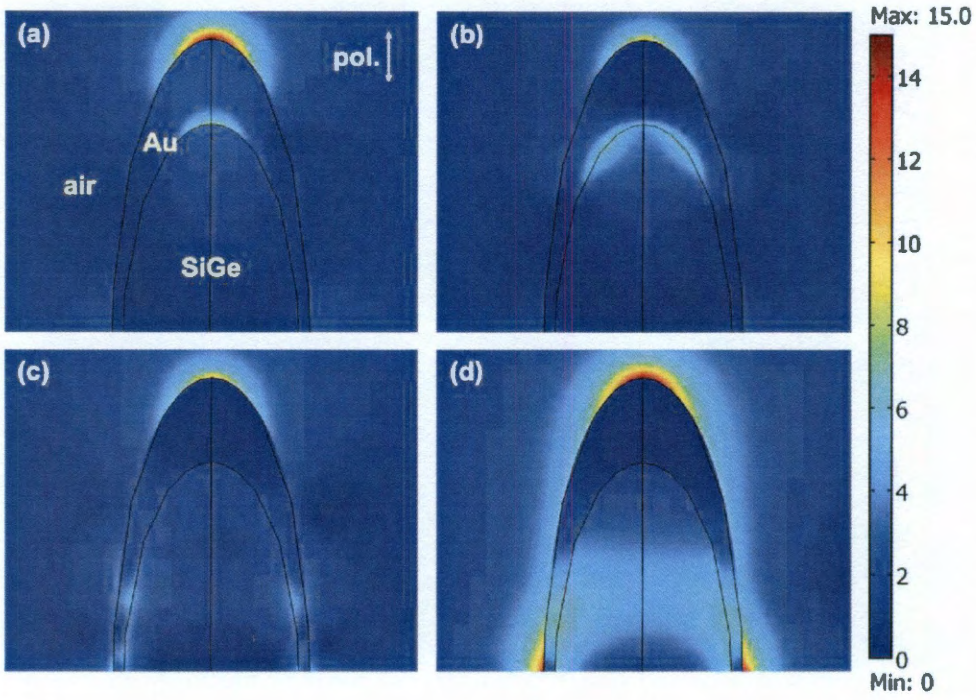

Figure 8.4 : Normalized electric field of the nanocone with axial (vertical) excitations at four different wavelengths: (a) 543, (b) 633, (c) 785, and (d) 1064 nm.

the overall EM enhancement with transversely polarized light, as indicated by the color scale, is not as strong as with axially polarized light.

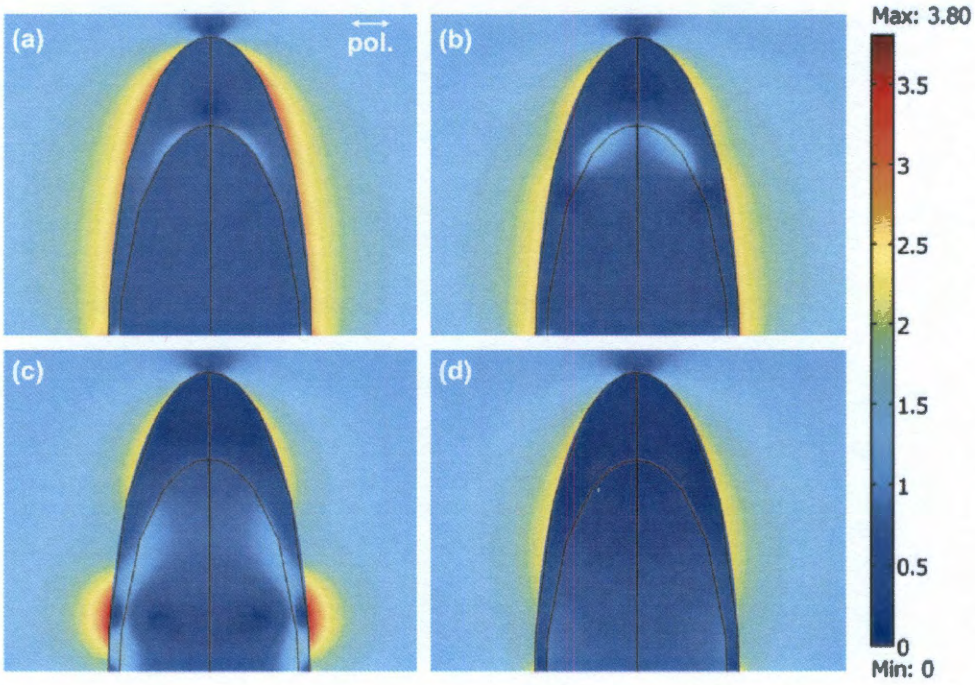

Figure 8.5 : Normalized electric field of the nanocone with transverse (horizontal) excitations at four different wavelengths: (a) 543, (b) 633, (c) 785, and (d) 1064 nm.

The relatively weak enhancement of the nanocones with in-plane excitations leaves space for improvement, because the majority of light is transversely polarized in a confocal setup where the laser light propagates perpendicularly to the sample substrate. An axial component of the focused light can exist only if the light is tightly focused to a point using a high NA objective (*i.e.*, the wave front at the focal point has a slight curvature), or if the sample substrate is oriented oblique to the light. The EM enhancement from transversely polarized light improves if narrow nanocones are packed in close proximity with one another and form nanoscale gaps. I show in Figure

6 that a narrow gap between a pair of nanocones [Figure 8.6(c)] generates relatively strong enhancement, whereas a singlet [Figure 8.6(a)] and a doublet [Figure 8.6(b)] in general do not generate strong enhancement.

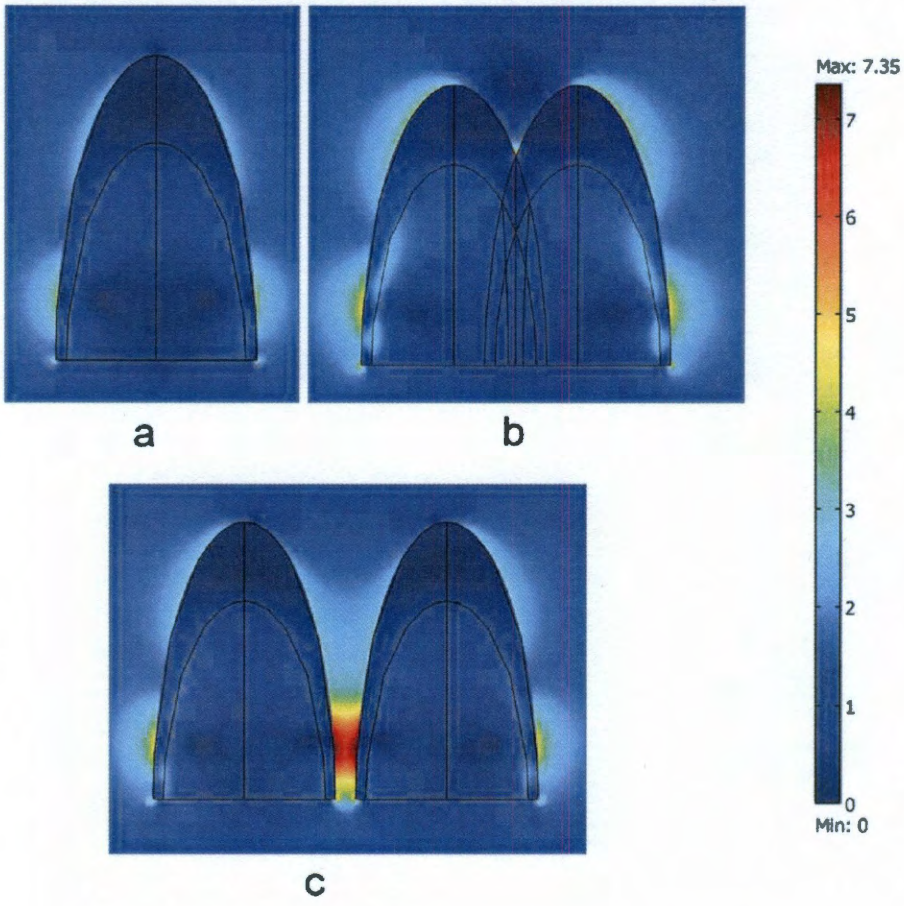

Figure 8.6 : Normalized electric field of (a) a nanocone singlet, (b) a nanocone doublet with a peak-to-peak distance of 60 nm, (c) a nanocone pair with a peak-to-peak distance of 100 nm. Nanocones have the same dimension as previously described. Transverse excitation at 785 nm.

It is also noteworthy that the geometries and the surface morphology vary across the substrate. I show in Figures 8.7 and 8.8 plots of normalized electric field on nanocones with the base diameters and heights that vary up to ±25% from the geom-

etry shown in Figures 8.5 and 8.4. I found that for axial polarization, the enhancement is affected by the tip radius; and for transverse polarization, the enhancement is more sensitive to the height of the nanocone than to its base width. The overall enhancing behavior of the nanocone, however, remains relatively insensitive to the variation of its dimensions. The simulations indicate that individual nanocones do not exhibit strong EM enhancement with transversely polarized light in comparison to axially polarized light. Thus, to improve the SERS performance of the substrate, I introduce plasmonic gold nanoparticles between nanocones to enhance the coupling efficiency to the transversely polarized light.

Table 8.1 : Dimensions of the SiGe nanocones simulated in Figures 8.7 and 8.8. Base diameters in rows and heights in columns.

Base dia./Height [nm]	70	100	125
60	a	b	c
80	d	e	f
100	g	h	i

8.5 Lateral Coupling between Nanocones and AuNPs

AuNPs situated near nanocones create lateral nanoscale gaps that can be excited by transversely polarized light. Figure 8.9 shows the simulation results for an AuNP situated between two nanocones. Figures 8.9(a) and 8.9(b) show the normalized electric field with the AuNP located at different elevations from the base of the nanocones. The excitation light is transversely polarized (along the gap) at 785 nm. The size of the gap between the AuNP and the nanocones is proportional to the vertical elevation of the AuNP from the substrate [shown in Figure 8.9(a)]. Before

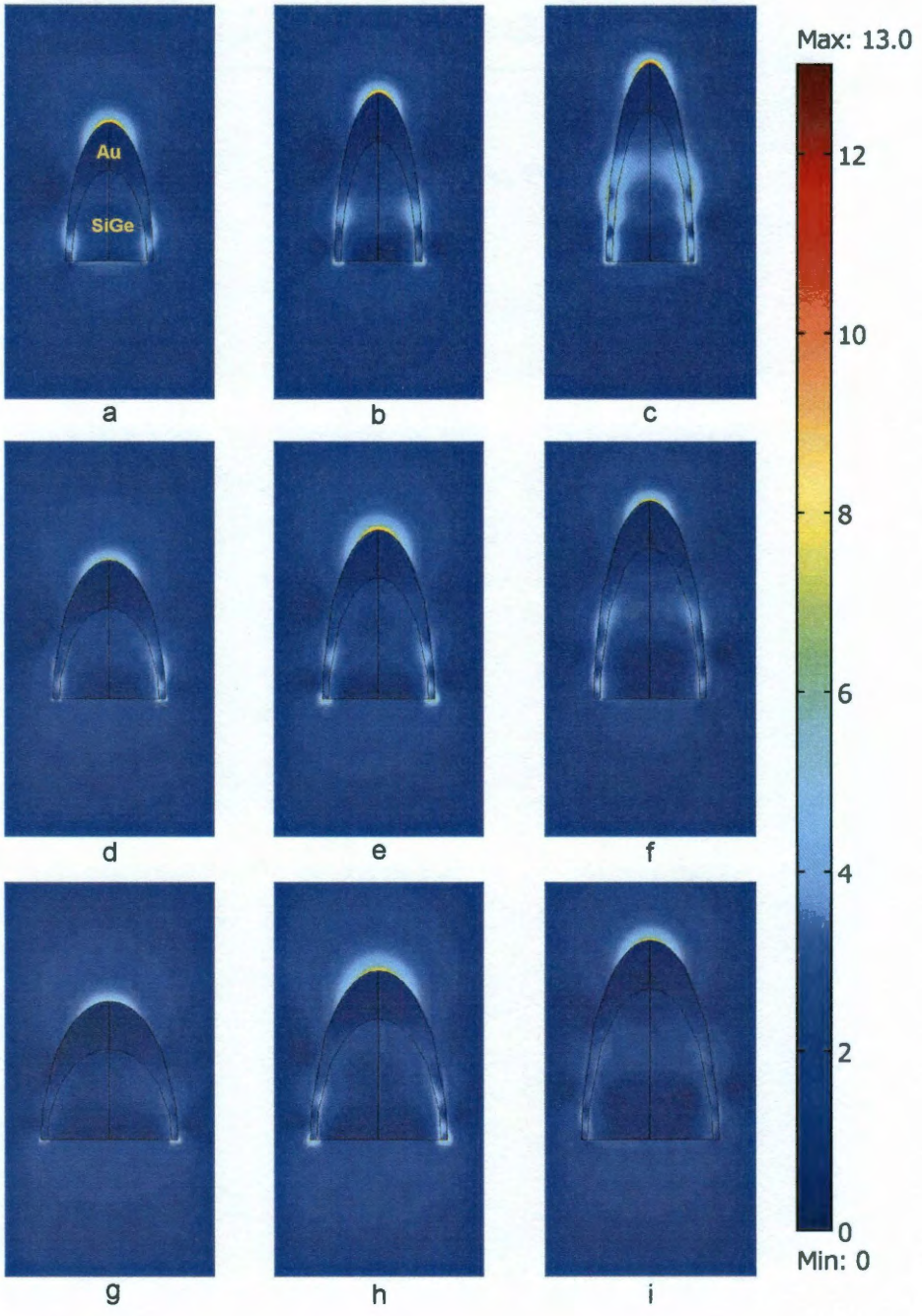

Figure 8.7 : Normalized electric field distribution of gold-coated SiGe nanocones with axial excitations at 785 nm and dimensions shown in Table 8.1.

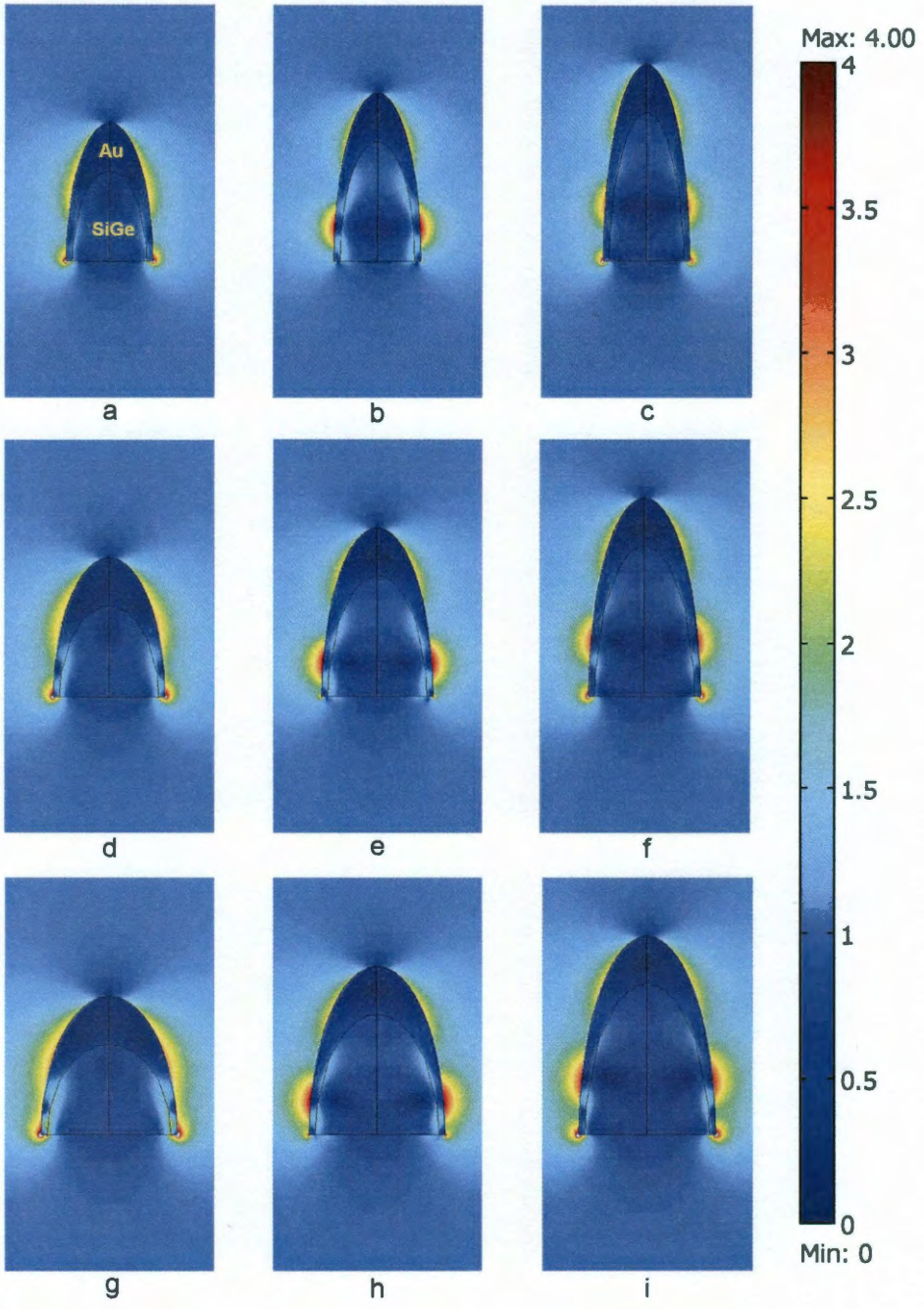

Figure 8.8 : Normalized electric field distribution of gold-coated SiGe nanocones with transverse excitations at 785 nm and dimensions shown in Table 8.1.

the AuNP couples to the nanocones, a moderate enhancement of the electric field can be observed in the gap between the nanocones. When the AuNP and the nanocones are in the close proximity to each other, the coupling between the AuNP and the nanocones strengthens and creates strong hotspots [Figure 8.9(b)].

The coupling between the nanocones and the AuNP can be interpreted using a relevant particle-film system reported in the literature [Le et al., 2005, Nordlander & Le, 2006, Le et al., 2007]. Briefly, the discrete plasmon modes of an AuNP couple with a continuum of the plasmon modes on a flat film. The superposition of the coupling between discrete and continuous modes creates virtual states. Surface charges on the nanoparticle and the nearby surface of the film generate large electric-field enhancement. In addition, image charges on the far side of the film contribute additional enhancement to the junction. Provided that the film is not too thin to support plasmons (*i.e.*$<$5 nm), a larger enhancement is generally observed on a thinner film [Nordlander & Le, 2006]. In comparison to a flat film, a core-shell nanocone possesses a large number of discrete modes (due to its large surface area compared to AuNPs) instead of continuous modes. The hybridization between the nanoparticle and the nanocone creates a large number of localized discrete plasmon modes, some of which are shifted to the visible and near-infrared region. When the wavelength of a plasmon mode is in vicinity of the Raman excitation wavelength, a strong coupling can be induced.

To quantify the added SERS enhancement and to visualize the synergistic effect between the AuNP and the nanocones, electric field across the gold surfaces both on the substrate and on the AuNP has been integrated. The EM enhancement, which is calculated as the fourth power of the electric field prior to the integration, is normalized by the values at the elevation of 155 nm, where the lowest point of the AuNP is

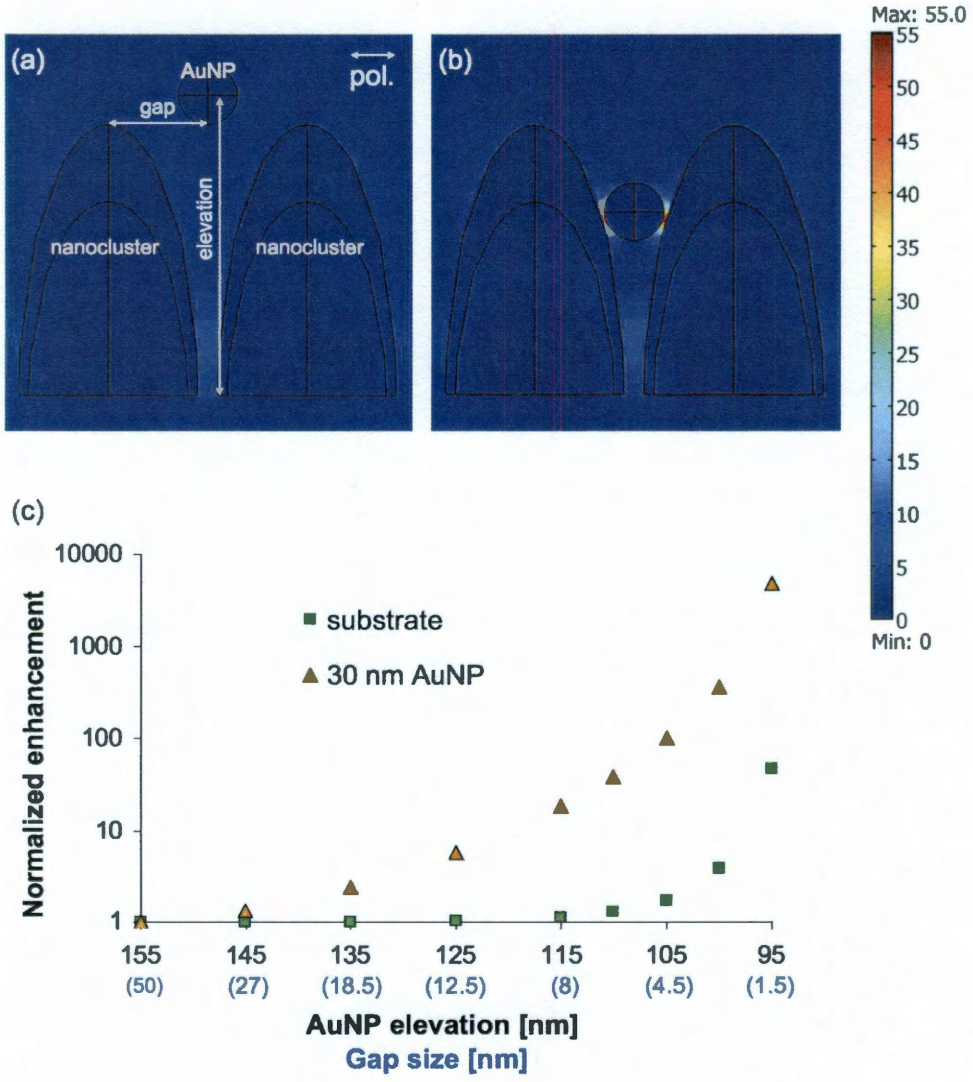

Figure 8.9 : Normalized electric field distribution of a 30-nm AuNP located between a pair of nanocones 100-nm apart and the enhancement resulted from the coupling. The AuNP is situated at an elevation of (a) 155 and (b) 95 nm. Panel (c) shows the normalized enhancement versus particle elevation for the AuNP-nanocone system (gap size denoted in parentheses). The excitation light at 785 nm is transversely polarized.

at the same elevation as the peak of the nanocone and no visible coupling between the AuNP and the nanocones can be observed [Figure 8.9(a)]. The normalized enhancement is plotted against AuNP elevation (or gap size) in Figure 8.9(c). The enhancement increases both on the AuNP and on the nanocone substrate as the gap size decreases. Due to the relatively larger surface area of the nanocones with respect to the size of the hot spot, the EM field in the substrate is enhanced at a slower rate than its counterpart in the 30-nm AuNP. An enhancement over tenfold is achieved on the substrate when the gap size is reduced to 1.5 nm.

8.6 AuNP-Decorated Nanocone Substrates and SERS Measurements

8.6.1 Spectral acquisition and the observation of added enhancement

I performed experimental measurements to verify the improved SERS performance indicated by the observations made in simulation results. Nanocone substrates were decorated using the 30-nm unconjugated colloidal gold solution in DI water purchased from Ted Pella (Redding, CA, USA). The solution has a particle concentration of 2 $\times$ 10^{11} particles/ml. A 20 μl aliquot of AuNP solution was applied onto the substrate and let it dry in air. The area coated by the droplet occupied $\sim$1/2 of the entire 1-cm^2 surface. On examining the AuNP-coated surface with an SEM, I found that AuNPs embedded evenly throughout the coated area and no large aggregates. Figure 8.10(a) shows a side view of the nanocone substrate before AuNP-decoration, and Figure 8.10(b) shows a top view of the nanocone substrate after AuNP-decoration (some AuNPs are indicated by the arrows).

50μM BPE solutions were used to incubate all substrates. In general, studies

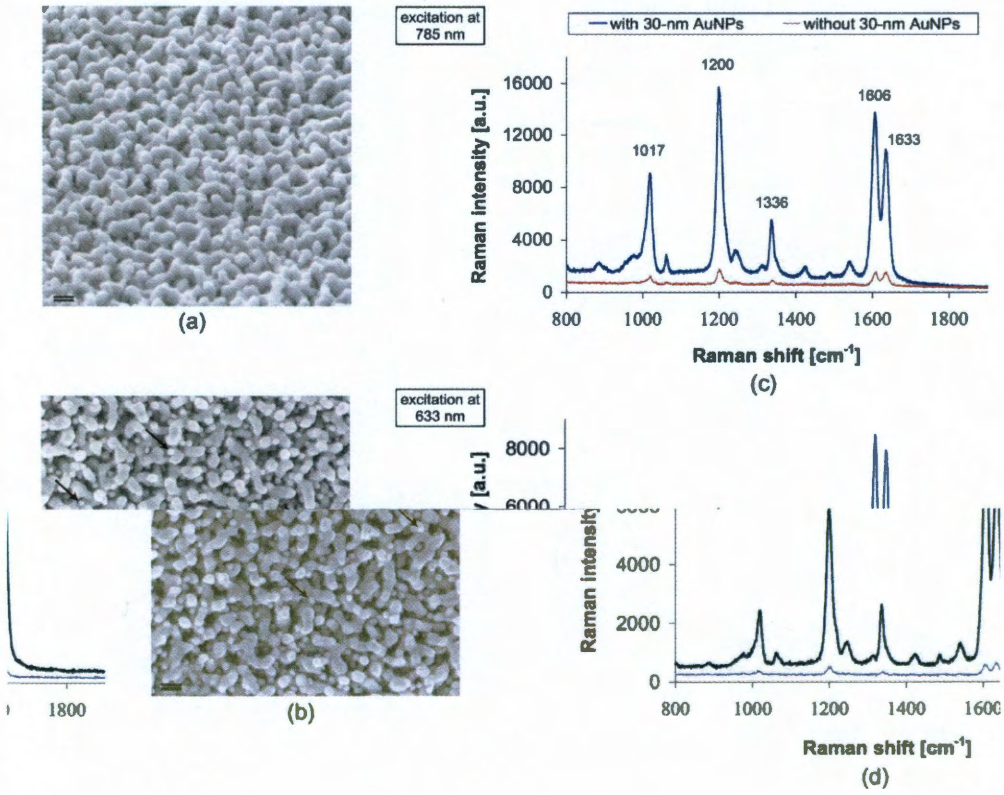

Figure 8.10 : SEM images showing (a) a side view of the nanocone substrate prior to AuNP-deposition, (b) a top view of the nanocone substrate after AuNP-deposition, and SERS spectra from BPE molecules on the nanocone substrate with (blue) and without (red) 30-nm AuNPs with the excitation wavelength of (c) 785 and (d) 633 nm. Scale bar is 100 nm in (a) and (b).

indicate that the Raman intensity increases linearly at low concentrations of Raman molecules and gradually declines at higher concentrations. Van Duynes group investigated cobalt phthalocyanine on rough Ag films and reported that the Raman intensity reaches its maximum at 10% monolayer coverage on rough substrates [Zeman et al., 1987]. Meanwhile, for BPE molecules, increasing the molecular concentration results in self quenching and causes the Raman intensity to decrease [Zeman et al., 1987, Chaney et al., 2005]. To estimate an optimal incubation time in conjunction with the concentration of BPE solution in order to obtain a sub-monolayer coating, a total of seven nanocone substrates were immersed in 5-ml solutions of 50-μM BPE solutions for 1, 6, 12, 18, 24, 48, and 72 hours, immediately followed afterward by SERS measurements. The intensity of the 1200 cm^{-1} mode increases approximately linearly from 1 to 24 hours, and gradually levels off around 48 hours, as shown in Figure 8.11. The plot indicates that a 24-hr incubation is likely to produce a sub-monolayer coverage. In light of this observation, substrates were incubated in 5 mL of 50-μM BPE solutions for 24 hours and blew dry the samples using N_2 gas.

A commercial Renishaw inVia Raman microscope was used for SERS measurements. Figure 8.10(c) and Figure 8.10(d) show representative spectra obtained from the substrates with and without 30-nm AuNPs. Figure 8.10(c) corresponds to the excitation wavelength of 785 nm and Figure 8(d) corresponds to 633 nm. For the 633-nm laser, 5% of its power was coupled into the microscope and approximately 0.13 mW was delivered to the sample. For the 785-nm laser, 1% of its power was coupled into the microscope and approximately 0.29 mW was delivered to the sample. An integration time of 10 s was used. At both excitation wavelengths, the substrate coated with AuNPs exhibits substantially stronger Raman scattering than the substrate without AuNPs. Additionally, I note that among the five most promi-

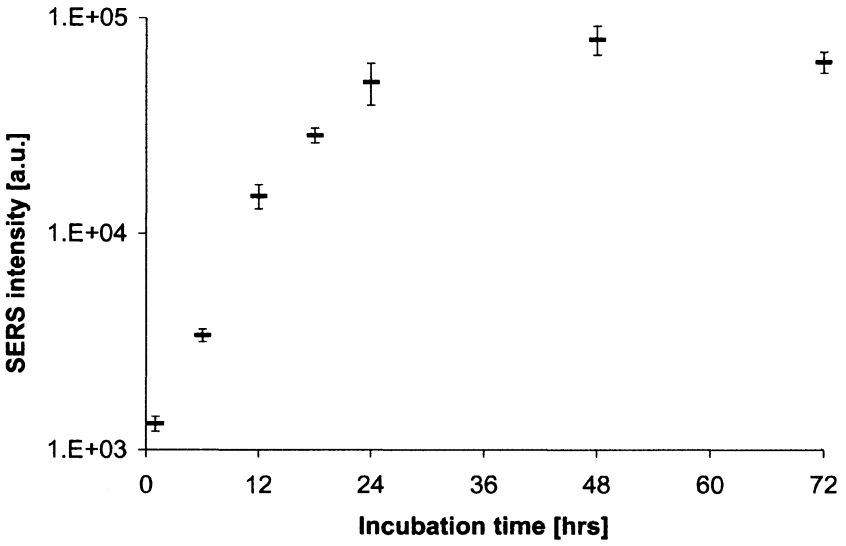

Figure 8.11 : SERS intensity of the 1200 cm−1 mode from the substrate, which was incubated for different time periods.

nent Raman modes of BPE molecules at 1017, 1200, 1336, 1606, and 1633 cm^{-1}, the amplitudes of the modes at 1200, 1606 and 1633 cm^{-1} appear to be sensitive to the excitation wavelength. At 785-nm excitation, the 1200-cm^{-1} peak is higher than the 1605- and 1634-cm^{-1} peaks; whereas at 633-nm excitation, the 1200-cm^{-1} peak is lower than the 1605- and 1634-cm^{-1} peaks. The relative change in amplitudes indicates a frequency-dependent nature of the SERS modes.

The 1200 cm^{-1} mode is used to characterize the enhancement Raman scattering. Twenty individual SERS spectra were acquired from ten different locations on the substrate. Within the AuNP-coated area, measurements were taken near the center to avoid densely packed AuNP aggregates that accumulated at the edges. SERS intensity of the 1200 cm^{-1} mode on the nanocone substrate before and after AuNP decoration has a standard deviation of 29% and 16% at 785 nm, and 22% and 18% at 633 nm, respectively. By comparing the intensity of 1200 cm^{-1} mode from the same

substrate before and after AuNP decoration, I found that the nanocone substrate decorated with AuNPs exhibited nearly 28 times stronger SERS activity at 785 nm compared to that of the nanocone substrate without AuNPs. Similar observation was made at 633 nm with an over 16-fold improvement.

8.6.2 Raman scan of the substrate

The Raman spectra were acquired using a 50×, 0.55 objective and exhibit relatively good spatial enhancement uniformity for the combined substrate. I further examine the uniformity of the AuNP-decorated nanocone substrate by performing a Raman scan. To acquire the integrated Raman intensities across the substrate (i.e., integrated intensities around the 1200 cm^{-1} mode), I employed a 100×, 0.95 objective. Figure 8.12 shows a representative scan of the AuNP-coated area on the nanocone substrate at 633-nm excitation along with Raman spectra sampled at four locations as indicated. Individual hotspots typically confined within 0.5–1 μm are clearly observed. Although these diffraction-limited hotspots do not allow us to resolve individual nanocone structures and AuNPs, the fact that they are distributed relatively uniformly over the nanocone substrate indicates that the AuNPs and the BPE are uniformly distributed over the nanocone substrate [this conclusion is also supported by the SEM image in Figure 8.10(b) in the manuscript]. With a lower NA objective (*i.e.*, 50×, 0.55), the Raman signal is spatially averaged and remains consistent over a large area of the substrate. Note that, if the AuNP coating was not uniform, large patches of enhancement (*i.e.*, bright areas in Figure 8.12) would be juxtaposed with large patches of non-enhancement (*i.e.*, dark areas in Figure 8.12).

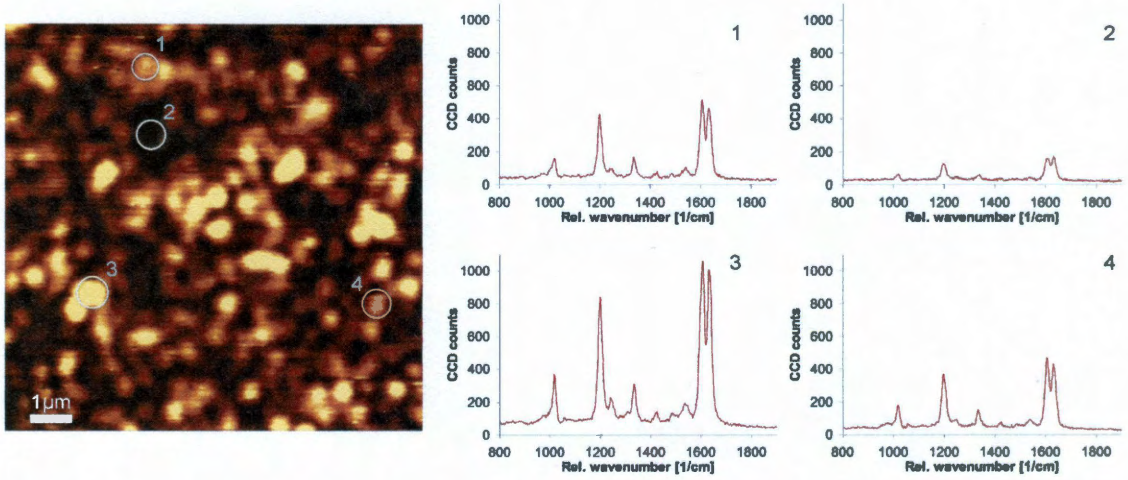

Figure 8.12 : Raman scan of the 30-nm AuNP-coated nanocone substrate (left) and SERS spectra (right) from four locations labeled in the scan image. The excitation wavelength is 633 nm, and a 100×, 0.95 objective lens was used. For the Raman scan image, the 1200 cm^{-1} mode was captured by integrating intensities from 1178 to 1227 cm^{-1}.

8.6.3 Enhancement factor (EF)

The SERS enhancement factor (EF) of the 30-nm AuNP-decorated nanocone substrate at the excitation wavelength of 785 nm was calculated for the 1200 cm^{-1} mode. The average background intensity, mostly caused by the auto-fluorescence of the gold, was subtracted from the Raman spectrum to obtain the peak value. The effective area contributing to SERS is estimated by adding the surface area of the nanocones with the surface area of the AuNPs. From the details given in the sections discussing AFM and SEM characterization, the effective area is 1.9 times the laser spot size. The packing density of the BPE molecules is estimated to be 3.30×10^6 μm^{-2}, with the approximate area of a single molecule to be 30 $\AA^2$ [Zeman et al., 1987]. I assumed 100% monolayer coverage of the surface by BPE molecules, which would lead to a more conservative estimate of EF due to the coating condition I used.

Prior to measuring Raman spectra from the neat solution, I determined the probe volume of the objective (50×, 0.55) using a gold nanocone substrate coated with BPE molecules as reference [Smythe et al., 2009]. The probe volume is modeled as a cylinder with diameter equal to the laser-focus spot size and height equal to the effective probe depth H_{obj}. The probe depth H_{obj} was measured by moving the substrate sample out of the focus plane at 1-μm increments and recording the Raman peak value at 1200 cm^{-1} at each position. Raman intensities were integrated over all positions and normalized by the maximum intensity at the focal plane, yielding H_{obj} = 28.54 μm.

Neat spectra were acquired by placing an aliquot of 0.1-M BPE solution under the objective. The excitation light was first focused onto the backside of the sealing coverslip, then moved further into the solution. The excitation power at 785 nm and the integration time were chosen so that the clearly distinct 1200 cm^{-1} mode would be obtained in the neat BPE-Raman spectrum while the corresponding BPE-SERS measurement at the same settings would not saturate the detector.

The EF is calculated using

$$EF = \frac{I_{SERS}}{I_{neat}} \times \frac{N_{neat}}{N_{SERS}}, \tag{8.1}$$

where I_{neat} and I_{SERS} represent the intensity of the neat and SERS signals of the 1200 cm^{-1} peak, and N_{neat} and N_{SERS} are the numbers of the BPE molecules contributing to the neat and SERS Raman intensities. As previously described, N_{neat} and N_{SERS} can be calculated from the effective volume and the effective surface area. Because I used the same measurement setup and excitation wavelength, the laser spot size is assumed to be identical, so it cancels out in the EF calculation. The spatially

averaged EF is calculated to be 1.78×10^8.

8.7 Discussion

A portion of the Raman enhancement after coating AuNPs to the nanocone substrate comes from the increased gold surface area from AuNPs. However, I prove here that this fraction is negligible in our experiments. From SEM images, such as Figure 8.10(b), I estimate the particle density of the 30-nm AuNPs to be 76 particles/μm^2. The surface area added per μm^2 by AuNPs on the substrate is calculated by multiplying the particle density with the surface area of a 30-nm sphere, and it yields a merely 8% increase to the total surface area. Thus, the additional enhancement must originate from other sources, such as lateral coupling between AuNPs and nanocones on the substrate.

While the EM theory may explain the increased EM enhancement from AuNPs, some observations are still unclear and require further study. For instance, the 1200-cm^{-1} mode from the nanocone substrate exhibits a frequency-dependent EM enhancement (*i.e.*, it is stronger than the 1600-cm^{-1} modes at 785-nm excitation, but weaker than the same modes at 633-nm excitation) both with and without AuNPs. Because EM theory suggests that all modes are equally amplified (*i.e.*, to the fourth power of the enhanced electric field), it cannot explain this mode-dependent enhancement. The autofluoresence of the gold substrate, which appears as background in the SERS spectra, is distributed non-uniformly with respect to the Raman shifts. Therefore, a simple background subtraction may skew the amplitudes of the Raman modes. I expect future efforts to seek more accurate methods to scale the amplitude of each Raman mode with respect to the substrate background level.

While in the hybridization model for the particle-film system, the magnitude of

enhanced electric field in the junction can be tuned by the thickness of the gold film (*i.e.*, a thinner film results in a larger EM enhancement) [Nordlander & Le, 2006], hybridization in the nanocone-nanoparticle system is more complex. Our nanocone substrate employs a high-permittivity dielectric material (ϵ_r= 14 for SiGe), which induces a strong screening effect. The screening charges in the dielectric offset image charges on the gold-dielectric interface. For this reason, I suspect that the enhancement in the nanoparticle-nanocone junction is less sensitive to the thickness of the gold layer on the nanocone.

8.8 Summary

From finite-element simulations, I show that individual nanocones on our process-engineered substrates do not generate strong enhancement with transversely polarized light, whereas the addition of gold nanoparticles creates lateral coupling to adjacent nanocones and harnesses transversely polarized light. The creation of nano-scale nanoparticle-nanocone junctions led to a relatively uniform enhancement of 1.78×10^8, over one order of magnitude stronger than that of the nanocone substrate alone. Using plasmon hybridization theory and finite-element simulations, I explain the nature of this coupling and demonstrate polarization-dependent enhancement from the substrate and the nanoparticles. I expect that the use of plasmonic nanoparticles supported by plasmonic structured metal surfaces is an efficient and practical approach. It has the potential to substantially improve the SERS sensitivity of the substrates designed with homogeneous structures and/or compositions.

Chapter 9

Conclusions and outlook

In this thesis work, both analytical (Mie) and numerical (FEM) approaches have been used to investigate the optical and plasmonic properties of micro- and nanostructures. I explored the plasmonic properties of gold nanoparticles, silica-gold core-shell nanoshells and gold-silica-gold multilayer nanoshells, each of which adds tunabilities to the previous nanoparticle due to the added surface plasmons. In multilayer nanoshells with the number of surface plasmon modes unchanged, reducing the geometric symmetry results in the excitation of higher-order plasmon modes and yield further tunabilities of the particle. For non-pasmonic structures, I used the Mie code to demonstrate that multilayer structures can be engineered to either reduce (anti-reflection coating) or enhance (photothermal bubbles) the scattering of light. Lastly, I showed that coupling between different plasmonic nanostructures produces large field confinement that enhances Raman scattering.

The study of the gold-silica-gold multilayer nanoshell is a logical extension from the silica-gold core-shell nanoshell. While the addition of the gold core splits the bonding mode of the silica-gold nanoshell into two plasmon modes and geometrical asymmetry allows mixed plasmon hybridization, a recent paper pointed out that such geometry exhibits build-in Fano resonances [Mukherjee et al., 2010]. Specifically, in concentric geometries, the broad superradiant (anti-bonding) and the narrow subradiant (bonding) dipole modes interfere to form a dipole-dipole Fano resonance, and in geometries with reduced symmetry, the dipolar subradiant mode couples with the

quadrupolar mode to form a secondary dipole-quadrupole Fano resonance [Mukherjee et al., 2010]. Other papers pointed out that Fano resonances produced from symmetry breaking in more complex structures revealed rather interesting properties, such as spatial and spectral localization of light from bowtie antennas [Zhang et al., 2009], and high sensing figure-of-merit from plasmonic nanoclusters [Lassiter et al., 2010]. I anticipate future research in the direction of studying clusters of multilayer nanoshells with and without geometrical symmetry. In particular, both near- and far-field properties of the clusters at Fano resonances need to be investigated. Such geometries may prove useful for bio-sensing, surface-enhanced Raman spectroscopy, and metamaterials.

The SERS study yet requires further investigation. Uniform coating of nanoparticles onto the nano-patterned substrate can be achieved by inserting a bifunctional molecule between the substrate and the nanoparticle (*i.e.*,-SH and -NH_2 groups are known to bind to Au). With the uniform coating, the mechanism behind SERS can be explored using the tip-enhanced Raman spectroscopy (TERS) microscope or near-field scanning optical microscope (NSOM). TERS and NSOM may allow for direct observation of the hot spot formed between the nanoparticle and the nanocone. Combined with the near-field measurements (*i.e.*, two-photon luminescence (TPPL)), the investigation can provide experimental evidence of the relationship between the near-field enhancement and Raman scattering.

In simulating nanostructures, current methods such as FEM and FDTD that involve the use of the bulk dielectric function suffice for structures that are much larger than the mean free path of the electron in a bulk material. Future development in nanoplasmonics will embark on much smaller nanostructures in which quantum effects manifest. For these nanostructures, electrons impinge upon the surface before

traversing the distance of a mean free path, and the electromagnetic field excited by surface plasmons can influence the confinement effect. The use of bulk properties to simulate these nanostructures is in question for they do no take into account the confinement effect. Thus, future research may use atomistic approaches, such as density functional theory, to investigate the plasmonic properties of nanostructures [Zuloaga et al., 2010]. In addition, hybrid methods that use both the classical electromagnetic and quantum mechanic theories allow for simulating larger nanostructures without the use of bulk properties. Perhaps the motivation of these quantum approaches is no longer on pure plasmonics, but rather on quantum-plasmonics, which may become the base of the next-generation of optical devices that can reach the resolution below the "plasmon limit".

Appendix A

Mie theory for concentric spheres

Light scattering by a multilayer concentric sphere can be understood by first looking at a simple case - scattering by a single sphere. The solution is derived from a linear combination of proper harmonic functions that satisfy the vector Helmholtz equation and divergence-free properties. Boundary conditions are then applied to solve for the scattering coefficients.

First consider a flat interface between two semi-infinite spaces, calculating the magnitude of the reflected and transmitted wave involves two light polarizations: E being perpendicularly or parallel with respect to the incidence plane, which is defined by the unit normal vector to the boundary and the incident wave vector. Because boundary conditions depend on the polarization state of the wave, two distinguish sets of solutions exist for the two polarizations. Thus, the reflectance/transmission coefficients, defined by the ratio between the reflected/transmitted wave and the incident wave, also depend on polarization of the incident wave.

When the interface becomes spherical, the transmitted wave becomes part of the internal field inside the sphere. The reflected (scattered) wave is calculated at two polarization modes: transverse-electric (TE) and transverse-magnetic (TM) mode. In the TE mode, no electric field is present in the direction of propagation; and in the TM mode, no magnetic field is present along the direction of propagation. Conventionally a_n and b_n represent reflection coefficients for the TE and TM wave, also known as the Mie scattering coefficients. From Mie coefficients, scattering, absorption, and

extinction (scattering + absorption) cross-sections can be calculated.

A.1 Vector Helmholtz equation

Maxwell's equations require time-harmonic radiation fields $\vec{E}$ and $\vec{H}$ satisfy the vector Helmholtz equation:

$$\bigtriangledown^2 \vec{A} + k^2 \vec{A} = 0 \tag{A.1}$$

If $\vec{\Phi}$ is a solution to the scalar Helmholtz equation, then

$$\vec{L} = \bigtriangledown \phi \tag{A.2}$$

is a solution to the vector Helmholtz equation. Due to the property:

$$\bigtriangledown \times \bigtriangledown \Phi = 0 \tag{A.3}$$

$\vec{L}$ is curl-free, that is:

$$\bigtriangledown \times \vec{L} = 0 \tag{A.4}$$

whereas from the Maxwell's equations, the solutions for a source-free region need to be divergence-free, such that:

$$\bigtriangledown \cdot \vec{E} = 0 \tag{A.5}$$

$$\bigtriangledown \cdot \vec{B} = 0 \tag{A.6}$$

Divergence-free solutions are therefore constructed based on $\vec{L}$:

$$\vec{M} = \hat{a} \times \vec{L} = \bigtriangledown \times \hat{a}\phi \tag{A.7}$$

$$\vec{N} = \frac{1}{k} \bigtriangledown \times \vec{M} = \frac{1}{k} \bigtriangledown \times \bigtriangledown \times \hat{a}\phi \tag{A.8}$$

where $\hat{a}$ is a unit vector. From the identity:

$$\bigtriangledown \cdot \bigtriangledown \times \vec{A} = 0 \tag{A.9}$$

one can readily prove $\vec{M}$ and $\vec{N}$ are divergence-free, that is:

$$\bigtriangledown \cdot \vec{M} = 0 \tag{A.10}$$

$$\bigtriangledown \cdot \vec{N} = 0 \tag{A.11}$$

Equations (A.2), (A.7) and (A.8) represent three complete independent solutions to the vector Helmholtz equation (A.1). In addition, the latter two satisfy Maxwell's equations, thus, $\vec{M}$ and $\vec{N}$ are called vector spherical wave function (VSWF). Any wave solution is composed of a combination of these VSWFs. In particular, $\vec{M}$ corresponds to TE-polarized waves and $\vec{N}$ to TM waves. Approximating continuous field in terms of a summation of discrete VSWFs is analogous to performing a Fourier transform to the wave function. While the approximation technique leaves out a truncation error, the discrete form of representation makes it possible for computer-based calculations. For instance, the "wave coefficients" can be written in terms of matrices and readily solved by using MATLAB.

The vector spherical functions $\vec{M}$ and $\vec{N}$ are further expanded:

$$\vec{M}_{nm}^{(1,2)}(kr) = \vec{N}_n h_n^{(1,2)}(kr) \vec{C}_{nm}(\theta, \phi) \tag{A.12}$$

$$\vec{N}_{nm}^{(1,2)}(kr) = \frac{h_n^{(1,2)}(kr)}{krN_n} \vec{P}_{nm}(\theta, \phi) + N_n [h_{n-1}^{(1,2)}(kr) - \frac{n h_n^{(1,2)}(kr)}{kr}] \vec{B}_{nm}(\theta, \phi) \tag{A.13}$$

where $h^{(1,2)}$ are the spherical Hankel functions of the first and second kind. The Hankel functions $h^{(1)}$ and $h^{(2)}$are defined by:

$$h^{(1)}(x) = j(x) + iy(x) \tag{A.14}$$

$$h^{(2)}(x) = j(x) - iy(x) \tag{A.15}$$

where i is the imaginary unit, j and y are the Bessel functions of the first and second kind. Note that Bessel function of the first kind $j(x)$ has a finite origin ($x = 0$), while Bessel function of the second kind $y(x)$ has a singularity at the origin. A linear combination of the two (*i.e.*, $[h^{(1)}(x) + h^{(2)}(x)]/2$) is only related to $j(x)$ and is finite at the origin. VSFWs of the regular kind ($M^{(3)}$ and $N^{(3)}$) are defined to be finite at the origin:

$$M^{(3)}_{nm}(kr) = \frac{1}{2}[\vec{M}^{(1)}_{nm}(kr) + \vec{M}^{(2)}_{nm}(kr)] \tag{A.16}$$

$$\vec{N}^{(3)}_{nm}(kr) = \frac{1}{2}[\vec{N}^{(1)}_{nm}(kr) + \vec{N}^{(2)}_{nm}(kr)]. \tag{A.17}$$

The normalization constant N_n in Equations (A.12) and (A.13) is $\frac{1}{\sqrt{n(n+1)}}$; $\vec{B}_{nm}(\theta,\phi)$,$\vec{C}_{nm}(\theta,\phi)$ and $\vec{P}(\theta,\phi)$ are defined by:

$$\vec{B}_{nm}(\theta,\phi) = \hat{\theta}\frac{\partial}{\partial\theta}Y^m_n(\theta,\phi) + \hat{\phi}\frac{im}{sin\theta}Y^m_n(\theta,\phi) \tag{A.18}$$

$$\vec{C}_{nm}(\theta,\phi) = \hat{\theta}\frac{im}{sin\theta}Y^m_n(\theta,\phi) - \hat{\phi}\frac{\partial}{\partial\theta}Y^m_n(\theta,\phi) \tag{A.19}$$

$$\vec{P}_{nm}(\theta,\phi) = \hat{r}Y^m_n(\theta,\phi) \tag{A.20}$$

where $Y_n^m(\theta, \phi)$are the normalized scalar spherical harmonics. $\vec{M}_{nm}^{(1)}$ and $\vec{N}_{nm}^{(1)}$ are the outgoing waves, and $\vec{M}_{nm}^{(2)}$ and $\vec{N}_{nm}^{(2)}$ are the incoming waves.

A.2 Mie coefficients for a single sphere

Waves in a spherical geometry are separated into the incident field, scattered field, and internal field. Each field is written as a summation of the VSWFs. Note that the time dependence e^{-jwt} is not explicitly included here.

The incident field has an equal incoming and outgoing component(*i.e.*, the field does not approach infinity at the origin):*

$$\vec{E}_{inc}(k_o r) = \sum_{n=1}^{\infty} \sum_{m=-n}^{n} [a_{nm} \vec{M}_{nm}^{(3)}(k_o r) + b_{nm} \vec{N}_{nm}^{(3)}(k_o r)]. \tag{A.21}$$

The a_{nm} and b_{nm} are the multipole expansion coefficients. The scattered field only has outgoing components:

$$\vec{E}_s(k_o r) = \sum_{n=1}^{\infty} \sum_{m=-n}^{n} [p_{nm} \vec{M}_{nm}^{(1)}(k_o r) + q_{nm} \vec{N}_{nm}^{(1)}(k_o r)] \tag{A.22}$$

The internal field has both incoming and outgoing components:

$$\vec{E}_{int}(k_i r) = \sum_{n=1}^{\infty} \sum_{m=-n}^{n} [c_{nm} \vec{M}_{nm}^{(3)}(k_i r) + d_{nm} \vec{N}_{nm}^{(3)}(k_i r)] \tag{A.23}$$

---

*The complete solution to the Helmholtz equation can be either described by the Bessel function j_n and the Hankel function of the first kind $h_n^{(1)}$ or the Hankel function of the first and second kind $h_n^{(1,2)}$. If the first method is adapted, j_n represents the incident wave and $h_n^{(1)}$ stands for the scattered wave. If instead the latter scheme is adapted, then $h_n^{(1)}$ represents the outgoing wave and $h_n^{(2)}$ for the incoming wave. I chose the second scheme because of its ease of physical interpretation and numerical stability. The Bessel and Hankel functions are related by:$h_n^{(1,2)} = j_n \pm j n_n$, where n_n goes to infinity at the origin.

The corresponding magnetic fields can be derived by using:

$$\vec{H} = -\frac{j}{kZ} \bigtriangledown \times \vec{E}$$

$$\vec{N} = \frac{1}{k} \bigtriangledown \times \vec{M}$$

$$\text{and} \quad \vec{M} = \frac{1}{k} \bigtriangledown \times \vec{N},$$

and the magnetic fields are written as:

$$\vec{H}_{inc}(k_o r) = -\frac{j}{Z_o} \sum_{n=1}^{\infty} \sum_{m=-n}^{n} [a_{nm} \vec{N}_{nm}^{(3)}(k_o r) + b_{nm} \vec{M}_{nm}^{(3)}(k_o r)] \tag{A.24}$$

$$\vec{H}_{s}(k_o r) = -\frac{j}{Z_o} \sum_{n=1}^{\infty} \sum_{m=-n}^{n} [p_{nm} \vec{N}_{nm}^{(1)}(k_o r) + q_{nm} \vec{M}_{nm}^{(1)}(k_o r)] \tag{A.25}$$

$$\vec{H}_{int}(k_i r) = -\frac{j}{Z_i} \sum_{n=1}^{\infty} \sum_{m=-n}^{n} [c_{nm} \vec{N}_{nm}^{(3)}(k_i r) + d_{nm} \vec{M}_{nm}^{(3)}(k_i r)]. \tag{A.26}$$

The scattering coefficients are obtained by p_{nm}/a_{nm} for TE and q_{nm}/b_{nm} for TM waves. To solve for the two unknowns, additional equations are generated from boundary conditions. By equating the tangential E and H field from the inside and outside of the sphere at the boundary, one obtains:

$$a_{nm} \vec{M}_{nm}^{tan(3)}(k_o R) + p_{nm} \vec{M}_{nm}^{tan(1)}(k_o R) = c_{nm} \vec{M}_{nm}^{tan(3)}(k_i R) \tag{A.27}$$

$$\frac{a_{nm}}{Z_o} \vec{N}_{nm}^{tan(3)}(k_o R) + \frac{p_{nm}}{Z_o} \vec{N}_{nm}^{tan(1)}(k_o R) = \frac{c_{nm}}{Z_i} \vec{N}_{nm}^{tan(3)}(k_i R). \tag{A.28}$$

Observations from equations (A.12)-(A.20) suggest that $\vec{M}$ is already the tangential component since it only depends on θ and ϕ. Similarly the tangential component of $\vec{N}$ only include the part multiplied by $\vec{B}_{nm}(\theta, \phi)$ because $\vec{P}_{nm}(\theta, \phi)$ depends on the

radial vector $\hat{r}$. Substituting equation(A.18) and (A.19) into the equations above and after simplification, the Mie coefficients are obtained:

$$a_n = \frac{p_{nm}}{a_{nm}} = -\frac{k_i Z_i h_n^{(3)}(k_i R) f_n^{(3)}(k_o R) - k_o Z_o h_n^{(3)}(k_o R) f_n^{(3)}(k_i R)}{k_i Z_i h_n^{(3)}(k_i R) f_n^{(1)}(k_o R) - k_o Z_o h_n^{(1)}(k_o R) f_n^{(3)}(k_i R)} \tag{A.29}$$

and

$$b_n = \frac{q_{nm}}{b_{nm}} = -\frac{k_i Z_o h_n^{(3)}(k_i R) f_n^{(3)}(k_o R) - k_o Z_i h_n^{(3)}(k_o R) f_n^{(3)}(k_i R)}{k_i Z_o h_n^{(3)}(k_i R) f_n^{(1)}(k_o R) - k_o Z_i h_n^{(1)}(k_o R) f_n^{(3)}(k_i R)} \tag{A.30}$$

where

$$f_n^{(1,3)}(k_{i,o} R) = k_{i,o} R h_{n-1}^{(1,3)}(k_{i,o} R) - n h_n^{(1,3)}(k_{i,o} R). \tag{A.31}$$

A.3 Scattering of a plane wave

For an incident plane wave traveling in the $\hat{z}$ direction and polarized in the $\hat{x}$ direction, the multipole expansion coefficients in equations (A.21)-(A.26) are:

$$a_{nm} = j^n \sqrt{\pi(2n+1)} \tag{A.32}$$

$$b_{nm} = j^{n-1} \sqrt{\pi(2n+1)}. \tag{A.33}$$

Given the Mie coefficients a_n and b_n, the scattered electric field can be expressed as:

$$\begin{aligned} \vec{E}_s(\theta, \phi) = \sum_{n=1}^{\infty} \sum_{m=\pm 1} [a_n i^n \sqrt{\pi(2n+1)} \vec{M}_{nm} + \\ b_n i^{n-1} \sqrt{\pi(2n+1)} \vec{N}_{nm}] \end{aligned} \tag{A.34}$$

More details about calculating the angular scattering field can be found in Section A.4. The total scattered power W_s and the incident light intensity I are related by

the scattering cross-section C_s:

$$W_s = C_s I_i.$$

Similarly the absorbed power W_{abs} and incident light intensity I are related by the absorption cross-section C_{abs}:

$$W_{abs} = C_{abs} I_i.$$

The extinction cross-section C_{ext} is defined as:

$$C_{ext} = C_s + C_{abs}.$$

This quantity can be calculated from Mie coefficients:

$$C_{ext} = \frac{2\pi}{k_o^2} \sum_{n=1}^{\infty} (2n+1) Re(a_n + b_n). \tag{A.35}$$

Due to the orthogonality of the VSWFs, the scattering cross-section C_{sca} can be calculated by directly summing the amplitude of each "mode":

$$C_{sca} = \frac{2\pi}{k_o^2} \sum_{n=1}^{\infty} (2n+1)(|a_n|^2 + |b_n|^2) \tag{A.36}$$

Thus, the absorption cross-section can be calculated as:

$$C_{abs} = C_{ext} - C_{sca}. \tag{A.37}$$

The extinction/scattering/absorption efficiency $Q_{ext}/Q_{sca}/Q_{abs}$, is obtained by normalizing the optical cross-section area to the particle's area projected onto a plane perpendicular to the incident wave (usually the physical cross-section). For a spherical

particle, the efficiency is calculated by:

$$Q_{ext} = \frac{2}{k_o R^2} \sum_{n=1}^{\infty} (2n+1) Re(a_n + b_n) \tag{A.38}$$

$$Q_{sca} = \frac{2}{k_o R^2} \sum_{n=1}^{\infty} (2n+1)(|a_n|^2 + |b_n|^2) \tag{A.39}$$

$$Q_{abs} = Q_{ext} - Q_{sca}. \tag{A.40}$$

A.3.1 A case study on Q_{ext}

I now study some non-absorbing dielectric spheres. The upper limit for n is kept at the next larger integer to $k_o R$; m takes the values of ± 1 for the plane wave. The extinction efficiency Q_{ext} and the angular radiation intensity is plotted against the size parameter $x = \frac{2\pi R}{\lambda_o}$, as shown in Figure A.1 and A.2 on page 131 and 132. One could observe the whispering gallery mode when the dielectric constant of the sphere is larger than that of the surrounding medium. In addition, the extinction efficiency converges to two as explained by the extinction paradox.

A.4 Angular radiation intensity

Angular distribution of scattered field can be obtained from equation (A.34). The major task is to solve the vector spherical wave functions $\vec{M}$ and $\vec{N}$. In the far field approximation, $kr >> 2\pi$ and $\frac{1}{kr} \rightarrow 0$, thus, terms with kr in the denominator of equation(A.13) vanish:

$$\vec{N}_{nm}^{(1,2)}(kr) = N_n h_{n-1}^{(1,2)}(kr) \vec{B}_{nm}(\theta, \phi) \tag{A.41}$$

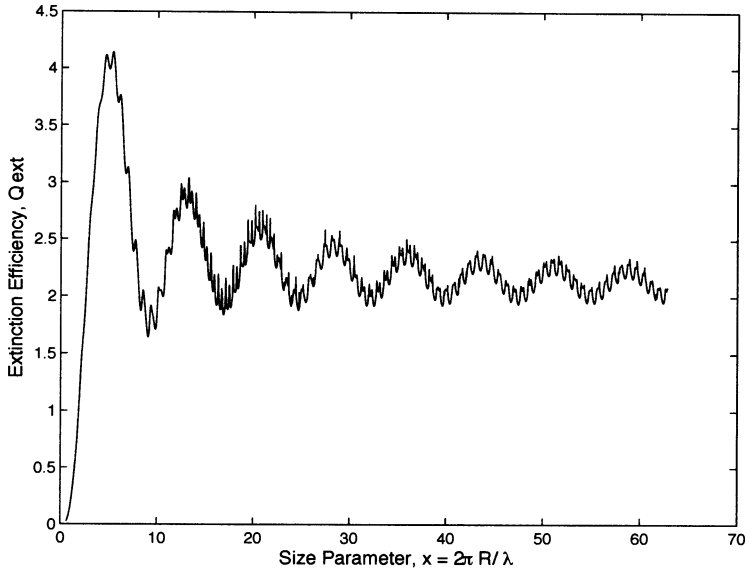

(a)

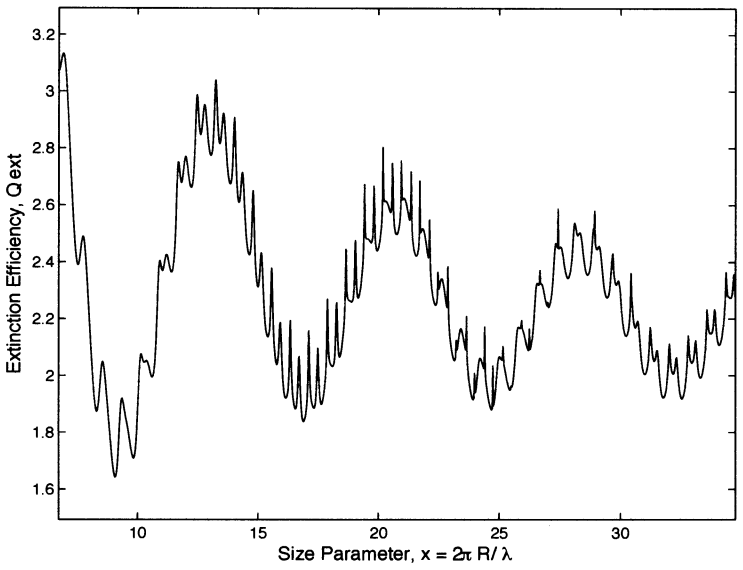

(b)

Figure A.1 : Extinction efficiency vs size parameter. ϵ_o=1.0 (surrounding medium), ϵ_i=2.0 (sphere). The large damped oscillation converges at Q_{ext}=2. The secondary ripples and spikes (see details image in (b)) correspond to the whispering gallery modes. This is due to the surface waves at the boundary.

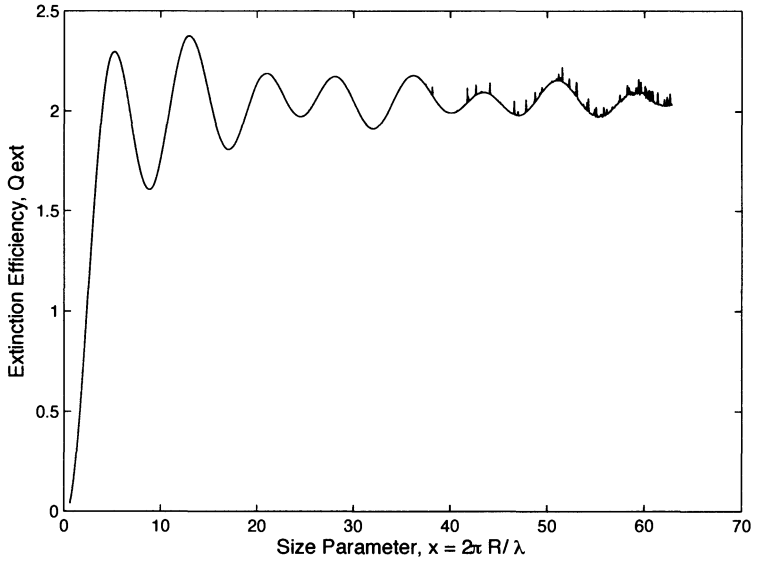

(a)

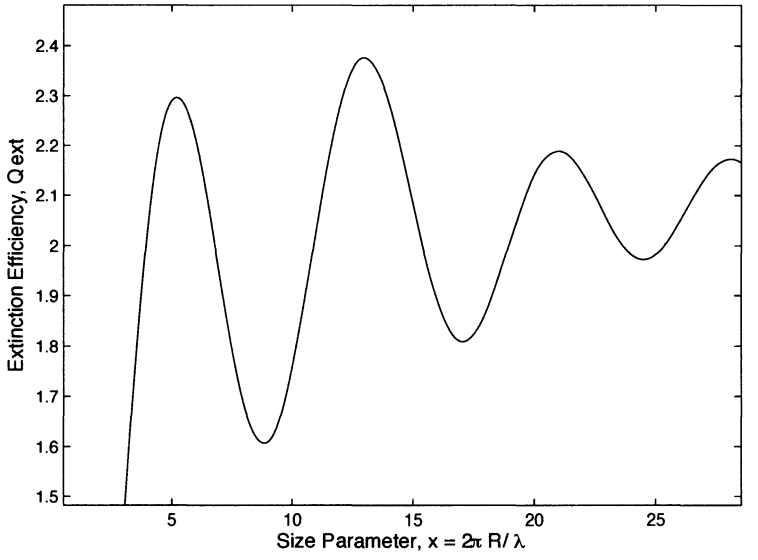

(b)

Figure A.2 : Extinction efficiency vs size parameter. ϵ_o=2.0, ϵ_i=1.0. The large damped oscillation still converges at Q_{ext}=2, but the whispering gallery modes vanish. This is due to the fact that surface waves are not supported when $\epsilon_o > \epsilon_i$.

In addition, the spherical Hankel function converges to:

$$h_n(kr) = \frac{(-i)^{n+1}}{kr} e^{jkr} \tag{A.42}$$

Combining equations (A.12),(A.34),(A.41) and (A.42), I obtain the expression for E in the far field:

$$\begin{aligned} \vec{E}_s(kr) = \sum_{n=1}^{\infty} \sum_{m=\pm 1} [a_n i^n \sqrt{\pi(2n+1)} N_n \frac{(-i)^{n+1}}{kr} e^{ikr} \vec{C}_{nm} \\ + b_n i^{n-1} \sqrt{\pi(2n+1)} N_n \frac{(-i)^n}{kr} e^{ikr} \vec{B}_{nm}] \end{aligned} \tag{A.43}$$

For simplicity, I write the equation above as:

$$\vec{E} = \frac{f(\vec{C}, \vec{B})}{kr} e^{ikr} \tag{A.44}$$

The phase term e^{ikr} does not contribute to the radiation intensity $I \propto |E|^2$.The r term in the denominator can be canceled by normalizing the intensity to solid angle per surface area. By further dropping k in the denominator, I rewrite equation (A.43) as:

$$\begin{aligned} \vec{E}_s(kr) = \sum_{n=1}^{\infty} \sum_{m=\pm 1} [a_n i^n \sqrt{\pi(2n+1)} N_n (-i)^{n+1} \vec{C}_{nm} \\ + b_n i^{n-1} \sqrt{\pi(2n+1)} N_n (-i)^n \vec{B}_{nm}] \end{aligned} \tag{A.45}$$

which gives:

$$\vec{E}_s(kr) = \sum_{n=1}^{\infty} \sum_{m=\pm 1} [a_n \sqrt{\frac{\pi(2n+1)}{n(n+1)}} \vec{C}_{nm} + b_n \sqrt{\frac{\pi(2n+1)}{n(n+1)}} \vec{B}_{nm}] \tag{A.46}$$

I now calculate the spherical harmonics $\vec{B}(\theta, \phi)$ and $\vec{C}(\theta, \phi)$. Note from equations (A.18) and (A.19):

$$\vec{B}(\hat{\theta}) = -\vec{C}(\hat{\phi}) \tag{A.47}$$

$$\text{and} \quad \vec{B}(\hat{\phi}) = \vec{C}(\hat{\theta}) \tag{A.48}$$

Both are related to the normalized scalar spherical harmonic $Y_{nm}(\theta, \phi)$ defined as:

$$Y_{nm}(\theta, \phi) = \sqrt{\frac{2n+1}{4\pi} \frac{(n-m)!}{(n+m)!}} P_n^m(cos\theta) e^{jm\phi} \tag{A.49}$$

where $P_n^m(x)$ is the associated Legendre function.

For the partial derivative of Y_{nm} with respect to θ, I use the recursion relation [†]:

$$\vec{B}(\hat{\theta}) = \frac{\partial}{\partial \theta} Y_{lm}(\theta, \phi) = \frac{1}{2} \sqrt{l(l+1) - m(m+1)} Y_{l(m+1)}(\theta, \phi) e^{-i\phi} - \frac{1}{2} \sqrt{l(l+1) - m(m-1)} Y_{l(m-1)}(\theta, \phi) e^{i\phi} \tag{A.50}$$

Meanwhile, notice from equation(A.49) and (A.18) that:

$$\vec{B}(\hat{\phi}) = \frac{\frac{\partial}{\partial \phi} Y_{lm}(\theta, \phi)}{sin\theta} \tag{A.51}$$

[†]D.A.Varshalovich, A.N.Moskalev, and V.K.Khersonsk,*Quantum Theory of Angular Momentum, pp 146*, World Scientific:Singarpore, 1988

I again use a recursion relation to avoid the singularity trauma at θ=0: ‡

$$\frac{1}{sin\theta}\frac{\partial}{\partial\phi}Y_{nm} = \frac{i}{2}[e^{-i\phi}\sqrt{\frac{(2n+1)(n+m+1)(n+m+2)}{2n+3}}Y_{(n+1)(m+1)} + e^{i\phi}\sqrt{\frac{(2n+1)(n-m+1)(n-m+2)}{2n+3}}Y_{(n+1)(m-1)}] \tag{A.52}$$

The angular scattering field can be solved from Equations(A.48),(A.47),(A.50) and (A.52) into (A.34),. Figure A.3 plots the angular scattering intensity versus size parameter in both $\phi = 0$ and 90° plane.

A.5 Approaching multilayer concentric spheres

The same approach described for a single sphere can be applied to an x-layer spherical structure which involves $2(x-1)$ linear equations and $x-1$ unknowns. I use the matrix representation for systematic linear equations arising from boundary conditions. I then directly solve the $x-1$ unknowns using a matrix division.

I illustrate this method using a four-layer sphere. As shown in Figure A.4, each layer of the sphere is numerically labeled. For the TE mode, the E field in region 4 is described as:

$$\vec{E}_4 = \vec{M}_4^{(3)} + q_{nm}\vec{M}_4^{(1)} \tag{A.53}$$

where $M_4^{(3)}$ defines the singularity-free regular vector spherical wave functions at the origin. Again using the notation $M^{(1)}$ for the outgoing wave, $M^{(2)}$ for the incoming wave, and $M^{(3)}$ for waves that are finite at the origin, I write the TE mode E field in

‡Adapted from Timo Nieminen's code

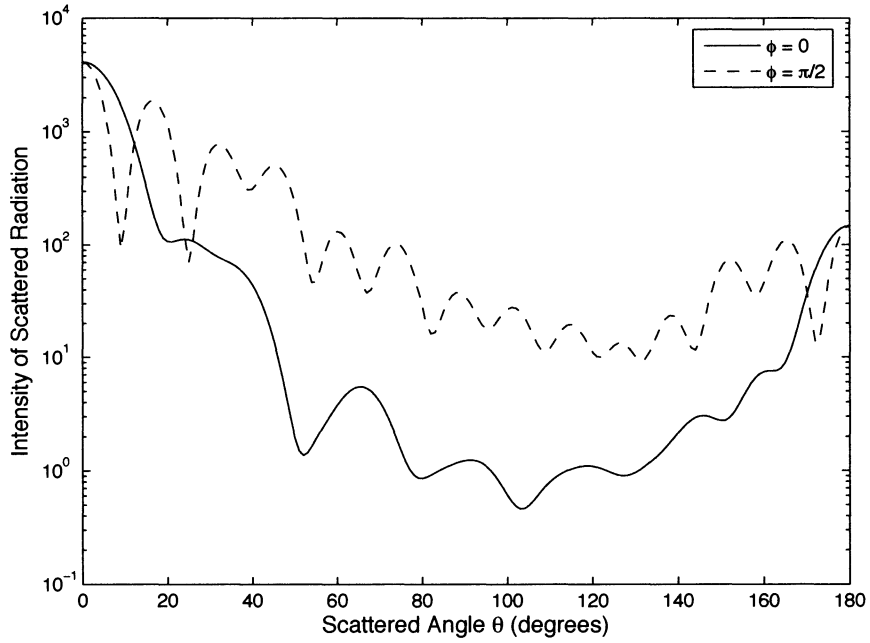

(a)

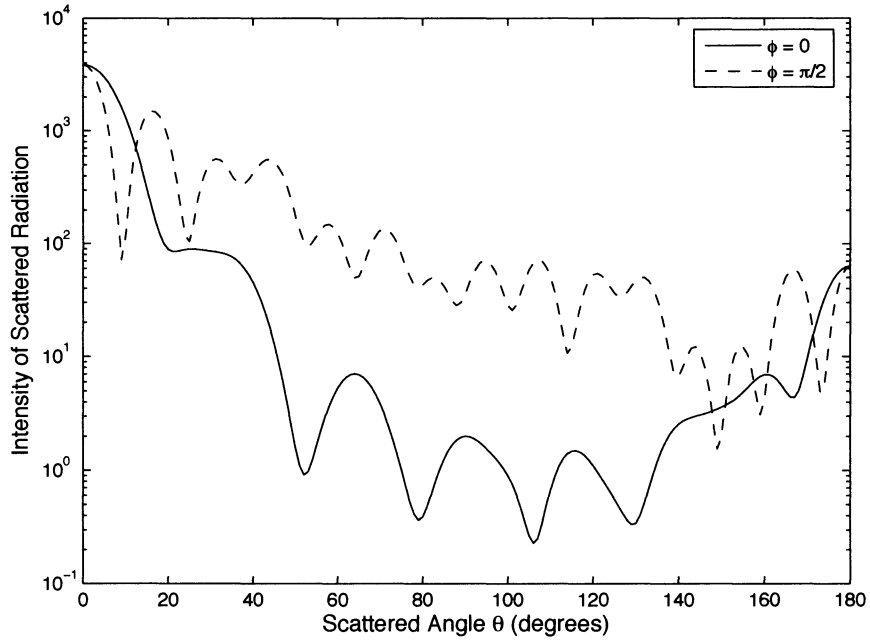

(b)

Figure A.3 : Intensity of scattered radiation vs scattered angle. (a)$\epsilon_i = 2.25$,$\epsilon_o = 1.00$, (b)$\epsilon_i = 1.00$,$\epsilon_o = 2.25$. Size parameter $x = \frac{2\pi R}{\lambda} = 15$.

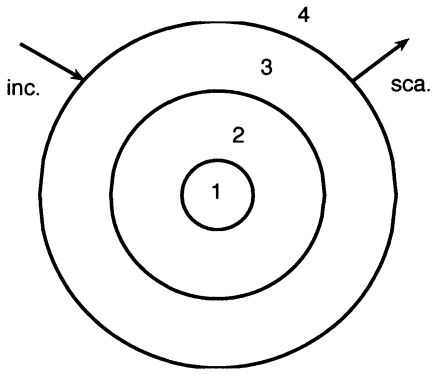

Figure A.4 : Four-layer spherical structure.

the rest of the regions as:

$$\vec{E}_3 = c_3\vec{M}_3^{(2)} + d_3\vec{M}_3^{(1)} \tag{A.54}$$

$$\vec{E}_2 = c_2\vec{M}_2^{(2)} + d_2\vec{M}_2^{(1)} \tag{A.55}$$

$$\text{and} \quad \vec{E}_1 = c_1\vec{M}_1^{(3)}. \tag{A.56}$$

The corresponding H field can be calculated as:

$$\vec{H}_4 = \frac{-i}{Z_4}[N_4^{(3)} + q_{nm}N_4^{(1)}] \tag{A.57}$$

$$\vec{H}_3 = \frac{-i}{Z_3}[c_3N_3^{(2)} + d_3N_3^{(1)}] \tag{A.58}$$

$$\vec{H}_2 = \frac{-i}{Z_2}[c_2N_2^{(2)} + d_2N_2^{(1)}] \tag{A.59}$$

$$\text{and} \quad \vec{H}_1 = \frac{-i}{Z_3}c_1N_3^{(1)}. \tag{A.60}$$

The boundary condition imposes the tangential E and H field to be continuous across the interfaces. By separating the radial and angular-dependents, I write the tangential

$\vec{M}$ and $\vec{N}$ as:

$$\vec{M}^{tan} = R(kr) \cdot A(\theta, \phi) \tag{A.61}$$

$$\vec{N}^{tan} = I(kr) \cdot B(\theta, \phi) \tag{A.62}$$

The angular component stays the same on both sides of the boundary as it is not a function of r. The remaining radial components can be obtained from equation(A.7) and (A.8):

$$R(kr) = N_n h_n^{(1,2)}(kr) \tag{A.63}$$

$$I(kr) = N_n [h_{n-1}^{(1,2)}(kr) - \frac{n h_n^{(1,2)}(kr)}{kr}] \tag{A.64}$$

The boundary conditions can be wriiten as:

$$\vec{E}_4^{tan} = \vec{E}_3^{tan} \Rightarrow R_4^{(3)} + q_4 R_4^{(1)} = c_3 R_3^{(2)} + d_3 R_3^{(1)} \tag{A.65}$$

$$\vec{H}_4^{tan} = \vec{H}_3^{tan} \Rightarrow \frac{1}{Z_4}[I_4^{(3)} + q_4 I_4^{(1)}] = \frac{1}{Z_3}[c_3 I_3^{(2)} + d_3 I_3^{(1)}] \tag{A.66}$$

$$\vec{E}_3^{tan} = \vec{E}_2^{tan} \Rightarrow c_3 R_3^{(2)} + d_3 R_3^{(1)} = c_2 R_2^{(2)} + d_2 R_2^{(1)} \tag{A.67}$$

$$\vec{H}_3^{tan} = \vec{H}_2^{tan} \Rightarrow \frac{1}{Z_3}[c_3 I_3^{(2)} + d_3 I_3^{(1)}] = \frac{1}{Z_2}[c_2 I_2^{(2)} + d_2 I_2^{(1)}] \tag{A.68}$$

$$\vec{E}_2^{tan} = \vec{E}_1^{tan} \Rightarrow c_2 R_2^{(2)} + d_2 R_2^{(1)} = c_1 R_1^{(3)} \tag{A.69}$$

$$\vec{H}_2^{tan} = \vec{H}_1^{tan} \Rightarrow \frac{1}{Z_2}[c_2 R_2^{(2)} + d_2 R_2^{(1)}] = \frac{1}{Z_1} c_1 R_1^{(3)}. \tag{A.70}$$

Because $R_4^{(3)}$ and $I_4^{(3)}$ are the only constant terms, I can write the equations above in a matrix form:

$$\begin{bmatrix} -R_4^{(1)} & R_3^{(2)} & R_3^{(1)} & 0 & 0 & 0 \\ -I_4^{(1)}/Z_4 & I_3^{(2)}/Z_3 & I_3^{(1)}/Z_3 & 0 & 0 & 0 \\ 0 & R_3^{(2)} & R_3^{(1)} & -R_2^{(2)} & -R_2^{(1)} & 0 \\ 0 & I_3^{(2)}/Z_3 & I_3^{(1)}/Z_3 & -I_2^{(2)}/Z_2 & -I_2^{(1)}/Z_2 & 0 \\ 0 & 0 & 0 & R_2^{(2)} & R_1^{(2)} & R_1^{(3)} \\ 0 & 0 & 0 & I_2^{(2)}/Z_2 & I_2^{(1)}/Z_2 & I_1^{(3)}/Z_1 \end{bmatrix} \begin{bmatrix} q_4 \\ c_3 \\ d_3 \\ c_2 \\ d_2 \\ c_1 \end{bmatrix} = \begin{bmatrix} R_4^{(3)} \\ I_4^{(3)}/Z_4 \\ 0 \\ 0 \\ 0 \\ 0 \end{bmatrix}$$

The six unknowns are q_4,c_3,d_3,c_2,d_2, and c_1. Because the magnitude of the incident wave $M_4^{(3)}$ in equation (A.53) is defined as unity, q_4 is in fact the ratio between the scattered and incident wave and therefore defines the Mie scattering coefficient for the TE mode. The other five parameters describe the scattering property of the internal layers. For the TM mode, I swap R and I in the matrices to obtain the corresponding scattering coefficients. For an x-layer sphere, the matrix on the left can be generalized into a $2(x-1) \times 2(x-1)$ square matrix and the calculation is cycled through each value of n in the spherical Hankel function till the upper limit is reached. Once the Mie coefficients are obtained, the extinction efficiency and the angular radiation intensity can be calculated by the same procedures described in sections A.3 and A.4.

Appendix B

Mie code for multilayer nanoshells in MATLAB

```
********Main Script*******
% MULTILAYER CODE FOR NANOSHELL CALCULATION
% V1.0
% COPYRIGHT 2007 RICE UNIVERSITY
% DEVELOPPED BY YING HU <HOOYING@RICE.EDU>

%%%%%%%%%%%%%%%%%%%%%%%%%%%%%%%%%%%%%%%%%%%%%%%%%%%%%%%%%%%%%%%%%%%%%%%%%%%%
% - WHAT DOES THIS CODE DO:
% IT CALCULATES THE EXTINCTION/ABSOPTION/SCATTERING EFFICIENCY OF A SINGLE GOLD
% NANOSHELL. IT IS BASED ON A MORE POWERFUL CODE THAT CALCULATES CONCENTRIC
% MULTILAYER SPHERES WITH ARBITRARY PROPERTIES.
%%%%%%%%%%%%%%%%%%%%%%%%%%%%%%%%%%%%%%%%%%%%%%%%%%%%%%%%%%%%%%%%%%%%%%%%%%%%
% - INPUT:
% A TEXT FILE NAMED 'mlayer_NS.txt' UNDER THE SAME DIRECTORY THIS PACKAGE
% IS RUNNING. THE INPUT FILE HAS THE FOLLOWING FORMAT:
% ROW 1: "NUMBER OF LAYERS" (3 FOR NANOSHELLS INCLUDING THE MEDIUM LAYER)
%        "START WAVELENGTH IN NM"
%        "END WAVELENGTH IN NM"
% ROW 2: "INNER RADIUS IN METERS"
%        "REAL PART OF THE CORE RELATIVE PERMITTIVITY"(~2.4 FOR SILICA)
%        "IMAGINARY PART OF CORE PERMITTIVITY" (0 FOR SILICA)
%        "REAL PART OF THE CORE RELATIVE PERMEABILITY"(1 FOR SILICA)
%        "IMAGINARY PART OF THE CORE RELATIVE PERMEABILITY"(0 FOR SILICA)
% ROW 3: "INNER RADIUS IN METERS"(SAME AS ROW 2)
%        "REAL PART OF THE SHELL RELATIVE PERMITTIVITY"(GOLD PROPERTY STARTS AT 400NM)
%        "IMAGINARY PART OF THE SHELL PERMITTIVITY" (0 FOR GOLD)
%        "REAL PART OF THE SHELL RELATIVE PERMEABILITY"(1 FOR GOLD)
%        "IMAGINARY PART OF THE SHELL RELATIVE PERMEABILITY"(0 FOR GOLD)
% ROW 4: "OUTER RADIUS IN METERS"
%        "REAL PART OF THE MEDIUM RELATIVE PERMITTIVITY"(1.7689 FOR WATER)
```

```
%        "IMAGINARY PART OF THE MEDIUM RELATIVE PERMITTIVITY" (0 FOR WATER)
%        "REAL PART OF THE MEDIUM RELATIVE PERMEABILITY"(1 FOR WATER)
%        "IMAGINARY PART OF THE MEDIUM RELATIVE PERMEABILITY"(0 FOR WATER)
%%%%%%%%%%%%%%%%%%%%%%%%%%%%%%%%%%%%%%%%%%%%%%%%%%%%%%%%%%%%%%%%%%%%%%%%%%%%
% - OUTPUT:
% DATA STORED IN Qext.TXT, Qabs.TXT AND Qsca.TXT ACCORDINGLY WITH THE FIRST
% COLUMN BEING THE WAVELENGTH. OPEN THESE FILES WITH WORDPAD OR IMPORT DATA
% TO EXCEL USING TAB AS THE DELIMITER Qext,Qabs AND Qsca ARE ALSO PLOTTED.
%%%%%%%%%%%%%%%%%%%%%%%%%%%%%%%%%%%%%%%%%%%%%%%%%%%%%%%%%%%%%%%%%%%%%%%%%%%%
% - CAUTION:
% ALL FILES IN THIS PACKAGE ARE REQUIRED FOR PROPER RUNNING.
%%%%%%%%%%%%%%%%%%%%%%%%%%%%%%%%%%%%%%%%%%%%%%%%%%%%%%%%%%%%%%%%%%%%%%%%%%%%
% - UPDATES IN THE NEXT VERSION
% ANGULAR RADIATION INTENSITY
% GAUSSIAN CORE DISTRIBUTION
%%%%%%%%%%%%%%%%%%%%%%%%%%%%%%%%%%%%%%%%%%%%%%%%%%%%%%%%%%%%%%%%%%%%%%%%%%%%



%%%%%%%%%%%%%%%%%%%%
% logs
%%%%%%%%%%%%%%%%%%%%
%11-16-07
%for gold-silica-gold NS
%11-16-07
% separated the main functions out
% added in the modification function for bulk gold properties
%11-7-07
% corrected for version 6.5
%8-28-07
% enabling exporting data to txt files
% use WORDPAD to open the file, delimiter = tab
% do NOT use NOTEPAD to open the data file or they will look clumsy

%8-23-07
% trying to finalize the program, add the functionality to allow user to
% input start/end wavelength
% separate gold property into gold.txt
```

```
%8-23-07
% updated graphics in plot

%8-18-07

%modifications:
% - Based on the previous working edition, this version adds the Qsca and
% Qabs based on formulas in Van De Hulst pp128

%8-13-07

%modifications:
% 1 -  mlayer.txt will contain the detailed gold properties in the latter
% portion of the file

% requirement:
% 1 - wavelength has to start from 400nm and end at 1400nm with 1nm increment

clear all, clc
warning off all
M = dlmread('mlayer_MlayerNS.txt');



uz = 4*pi*1e-7;
ez = 8.854e-12;

%read data
nlayer=M(1,1);
lambdastart = M(1,2);
lambdaend = M(1,3);
for ind=1:nlayer
    R(ind)=M((ind+1),1);
    e(ind)=M((ind+1),2)+i*M((ind+1),3);
    u(ind)=M((ind+1),4)+i*M((ind+1),5);
    rn(ind) = sqrt(e(ind)*u(ind));
    Z(ind)= sqrt(u(ind)*uz/(e(ind)*ez));
```

```
end


% located the start/end wavelength
golddata = dlmread('gold_prop_1941.txt','\t');
lambdata = golddata(:,1);
lenlambdata = length(lambdata);
for ind = 1:lenlambdata
    if lambdata(ind) == lambdastart
        flag1 = ind;
        break
    end
end
for ind = flag1:lenlambdata
    if lambdata(ind) == lambdaend
        flag2 = ind;
        break
    end
end

gold = golddata(flag1:flag2,:);

%%%%%%%%%%%%%%%%%%%%%%%%%%%%%%%%
mod = input('Whether want the bulk gold properties to be modified for nanoparticles? 1 for yes, 0 for no... \n');
% gold modification data

if mod ==1
    % should modify according to the core diameter
    gold1=goldmod_v1(lambdastart,lambdaend,(flag2-flag1+1), golddata(flag1:flag2,:), R(1)*2);
    gold3=goldmod_v1(lambdastart,lambdaend,(flag2-flag1+1), golddata(flag1:flag2,:), R(4)-R(3));
else
    gold1=gold;
    gold3=gold;
end

%%%%%%%%%%%%%%%%%%%%%%%%%%%%%%%%Lambda Sweep%%%%%%%%%%%%%%%%%%
sp=flag2 - flag1; %# of sample points
lambdavec = linspace(lambdastart,lambdaend,sp+1);
```

```
vec=lambdavec*1e-9;

for lambdaswp = 1:(sp+1)

    lambda = lambdavec(lambdaswp)*1e-9;
    for ind=1:nlayer
        k(ind)= 2*pi/(lambda/rn(ind));
    end
    %embed the wavelength-dependent gold proerty
    val = yhreturnind(vec,lambda);

    %layers 1 and 3 are gold
    if val~=0

        e(1)=gold1(val,2)+i*gold1(val,3);
        rn(1) = sqrt(e(1)*u(1));
        k(1)= 2*pi/(lambda/rn(1));
        Z(1)= sqrt(u(1)*uz/(e(1)*ez));

        e(3)=gold3(val,2)+i*gold3(val,3);
        rn(3) = sqrt(e(3)*u(3));
        k(3)= 2*pi/(lambda/rn(3));
        Z(3)= sqrt(u(3)*uz/(e(3)*ez));

%         e(5)=gold3(val,2)+i*gold3(val,3);
%         rn(5) = sqrt(e(5)*u(5));
%         k(5)= 2*pi/(lambda/rn(5));
%         Z(5)= sqrt(u(5)*uz/(e(5)*ez));

    end

    %%%%%%%%%%%%%%%%%%%%%%%%%%Lambda Sweep%%%%%%%%%%%%%%%%%%%%%%%%%%%%%%%%%%%%%%%%
    %keyboard

    [an,bn] = mlayermie(nlayer,lambda,R,k,Z);


    limit = k(nlayer).*R(nlayer)+3*(k(nlayer).*R(nlayer))^(1/3);
```

```
    limit=ceil(limit);

    sumext = 0;
    sumsca = 0;
    k = 2*pi/(lambda/rn(nlayer));
    for ind = 1:limit
        sumext = sumext + (2*ind+1)*real(an(ind)+bn(ind));
        sumsca = sumsca + (2*ind+1)*((abs(an(ind)))^2+(abs(bn(ind)))^2);
    end



    Qext(lambdaswp) = -2/(k*R(nlayer))^2*sumext;
    Qsca(lambdaswp) = 2/(k*R(nlayer))^2*sumsca;
    Qabs(lambdaswp) = Qext(lambdaswp) - Qsca(lambdaswp);


    %%%%%%%%%%%%%%%%%%%%%%%%%%%%Lambda Sweep%%%%%%%%%%%%%%%%%%%%%%%%
end


h=plot(lambdavec,Qext,'-k',lambdavec,Qsca,'--b',lambdavec,Qabs,'-.r');
legend('Q_{ext}','Q_{sca}','Q_{abs}');
ylabel('Extinction Efficiency, Q {ext}','fontsize',12)
xlabel('wavelength \lambda in nm','fontsize',12)
set(gca,'FontSize', 10)
set(h,'linewidth',2)



dataQext = [lambdavec',Qext'];
dataQabs = [lambdavec',Qabs'];
dataQsca = [lambdavec',Qsca'];
%
dlmwrite('Qext.txt',dataQext,'delimiter','\t','newline','pc')
dlmwrite('Qabs.txt',dataQabs,'delimiter','\t','newline','pc')
dlmwrite('Qsca.txt',dataQsca,'delimiter','\t','newline','pc')
```

```
%find Qext max
for ind=1:sp+1
    if Qext(ind)==max(Qext);
        lambdamax=lambdavec(ind)
    end
end
```

```
********************mlayer_MlayerNS.txt************************
4, 400, 1400
0.000000090, -1.649, 5.739, 1, 0
0.000000090, 2.04, 0, 1, 0
0.000000125, -1.649, 5.739, 1, 0
0.000000140, 1.7689, 0, 1, 0
```

```
*****************mlayermie.m******************
function [an,bn] = mlayermie(nlayer,lambda,R,k,Z)
% function "mlayermie" calculates the Mie coeff for multilayer concentric
% spheres
% INPUT: nlayer-total number of layers
% LAMBDA: wavelength in nm
% R: radii from inside out
% k: wave numbers from inside out
% Z: impedance from inside out

%take the outer ka as the limit
    limit = k(nlayer).*R(nlayer)+3*(k(nlayer).*R(nlayer))^(1/3);
    limit=ceil(limit);

    %%%%%%%%%%%%%%%%%%%%%%%%%%%%%%calculate TE mode%%%%%%%%%%%%%%%%%%%%%%%%
    %construct the RI-matrix
    RI=zeros(2*(nlayer-1),2*(nlayer-1),limit);
    qcd=zeros(2*(nlayer-1),1,limit);
    RIR=zeros(2*(nlayer-1),1,limit);
    for ind=1:limit %index for each n value

        if nlayer==2 %single sphere case needs to be considered separately because only two unknowns: q2 and c1
            R21 = 2*yhRn(ind,1,k(2),R(2));% factor of 2 for m=+-1
```

```
    R23 = 2*yhRn(ind,3,k(2),R(2));
    R13 = 2*yhRn(ind,3,k(1),R(2));
    I13 = 2*yhIn(ind,3,k(1),R(2))/Z(1);
    I23 = 2*yhIn(ind,3,k(2),R(2))/Z(2);
    I21 = 2*yhIn(ind,1,k(2),R(2))/Z(2);
    RI(:,:,ind) = [-R21,R13;-I21,I13];
    RIR(:,:,ind) = [R23;I23];
    qcd(:,:,ind) = inv(RI(:,:,ind))*RIR(:,:,ind); %only q2 and c1 are unknown here
    continue
end


% track has the opposite index order as the layer index
track = 1;
indl=nlayer;

while(indl>1) %interface between layer indl and indl-1

    Rn1=2*yhRn(ind,1,k(indl),R(indl));% factor of 2 for m=+-1
    Rn2=2*yhRn(ind,2,k(indl),R(indl));
    Rnm11=2*yhRn(ind,1,k(indl-1),R(indl));%R(n-1) type 1, same R, different k on each side
    Rnm12=2*yhRn(ind,2,k(indl-1),R(indl));

    In1=2*yhIn(ind,1,k(indl),R(indl))/Z(indl);
    In2=2*yhIn(ind,2,k(indl),R(indl))/Z(indl);
    Inm11=2*yhIn(ind,1,k(indl-1),R(indl))/Z(indl-1);
    Inm12=2*yhIn(ind,2,k(indl-1),R(indl))/Z(indl-1);


    % fill up the RI matrix
    if indl == nlayer % fill up the first block in the upper left corner
        RI(1:2,1:3,ind)=[-Rn1,Rnm12,Rnm11;-In1,Inm12,Inm11];
        track = track +1;
        indl = indl-1;
        continue
    end
    if (indl-1)==1 % fill up the last block in the lower right corner
        Rnm13 = 2*yhRn(ind,3,k(indl-1),R(indl));
```

```
            Inm13 = 2*yhIn(ind,3,k(indl-1),R(indl))/Z(indl-1);
            RI((2*nlayer-3):(2*nlayer-2),(2*nlayer-4):(2*nlayer-2),ind)=[Rn2,Rn1,Rnm13;In2,In1,Inm13];
            break
        end
        % fill up the second block in the upper right corner
        if  indl == nlayer-1
            RI(3:4,2:5,ind)=[Rn2,Rn1,-Rnm12,-Rnm11;In2,In1,-Inm12,-Inm11];
            track = track +1;
            indl = indl-1;
            continue
        end
        % fill up the rest of the blocks
        RI((2*track-1):(2*track),(2*track-2):(2*track+1),ind)=[Rn2,Rn1,-Rnm12,-Rnm11;In2,In1,-Inm12,-Inm11];

        track = track +1;
        indl = indl-1;
    end
    % single-column vector on the right of the equal sign
    Rn3 = 2*yhRn(ind,3,k(nlayer),R(nlayer));
    In3 = 2*yhIn(ind,3,k(nlayer),R(nlayer))/Z(nlayer);
    RIR(1:2,1,ind)=[Rn3;In3];
    qcd(:,:,ind)=inv(RI(:,:,ind))*RIR(:,:,ind);
end
TEcoeff=qcd; % TEcoeff stores the TE data
%%%%%%%%%%%%%%%%%%%%%%%%%%%%%%%%%%%%%%%%%%%%%%%%%%%%%%%%%%%%%%%%%%%%%%%%%%%
%%%%%%%%%%%%%%%%%%%%%%%%%%%%%calculate TM mode%%%%%%%%%%%%%%%%%%%%%%%%%%%%
%construct the RI-matrix
RI=zeros(2*(nlayer-1),2*(nlayer-1),limit);
qcd=zeros(2*(nlayer-1),1,limit);
RIR=zeros(2*(nlayer-1),1,limit);

for ind=1:limit %index for each n value

    if nlayer==2 %single sphere case needs to be considered separately because only two unknowns: q2 and c1
        R21 = 2*yhRn(ind,1,k(2),R(2))/Z(2);% factor of 2 for m=+-1
        R23 = 2*yhRn(ind,3,k(2),R(2))/Z(2);
        R13 = 2*yhRn(ind,3,k(1),R(2))/Z(1);
        I13 = 2*yhIn(ind,3,k(1),R(2));
```

```
    I23 = 2*yhIn(ind,3,k(2),R(2));
    I21 = 2*yhIn(ind,1,k(2),R(2));
    RI(:,:,ind) = [-I21,I13;-R21,R13];
    RIR(:,:,ind) = [I23;R23];
    qcd(:,:,ind) = inv(RI(:,:,ind))*RIR(:,:,ind); %only q2 and c1 are unknown here
    continue
end


% track has the opposite index order as the layer index
track = 1;
indl=nlayer;

while(indl>1) %interface between layer indl and indl-1

    Rn1=2*yhRn(ind,1,k(indl),R(indl))/Z(indl);% factor of 2 for m=+-1
    Rn2=2*yhRn(ind,2,k(indl),R(indl))/Z(indl);
    Rnm11=2*yhRn(ind,1,k(indl-1),R(indl))/Z(indl-1);%R(n-1) type 1, same R, different k on each side
    Rnm12=2*yhRn(ind,2,k(indl-1),R(indl))/Z(indl-1);

    In1=2*yhIn(ind,1,k(indl),R(indl));
    In2=2*yhIn(ind,2,k(indl),R(indl));
    Inm11=2*yhIn(ind,1,k(indl-1),R(indl));
    Inm12=2*yhIn(ind,2,k(indl-1),R(indl));


    % fill up the RI matrix
    if indl == nlayer % fill up the first block in the upper left corner
        RI(1:2,1:3,ind)=[-In1,Inm12,Inm11;-Rn1,Rnm12,Rnm11];
        track = track +1;
        indl = indl-1;
        continue
    end
    if (indl-1)==1 % fill up the last block in the lower right corner
        Rnm13 = 2*yhRn(ind,3,k(indl-1),R(indl))/Z(indl-1);
        Inm13 = 2*yhIn(ind,3,k(indl-1),R(indl));
        RI((2*nlayer-3):(2*nlayer-2),(2*nlayer-4):(2*nlayer-2),ind)=[In2,In1,Inm13;Rn2,Rn1,Rnm13];
        break
```

```
            end
            % fill up the second block in the upper right corner
            if  indl == nlayer-1
                RI(3:4,2:5,ind)=[In2,In1,-Inm12,-Inm11;Rn2,Rn1,-Rnm12,-Rnm11];
                track = track +1;
                indl = indl-1;
                continue
            end
            % fill up the rest of the blocks
            RI((2*track-1):(2*track),(2*track-2):(2*track+1),ind)= [In2,In1,-Inm12,-Inm11;Rn2,Rn1,-Rnm12,-Rnm11];;

            track = track +1;
            indl = indl-1;
        end
        % single-column vector on the right of the equation sign
        Rn3 = 2*yhRn(ind,3,k(nlayer),R(nlayer))/Z(nlayer);
        In3 = 2*yhIn(ind,3,k(nlayer),R(nlayer));
        RIR(1:2,1,ind)=[In3;Rn3];
        qcd(:,:,ind)=inv(RI(:,:,ind))*RIR(:,:,ind);
    end
    TMcoeff=qcd; %TMcoef stores TM data

   for ind=1:limit
        an(ind)=TEcoeff(1,1,ind);
        bn(ind)=TMcoeff(1,1,ind);
   end

   return

   ***************************yhRn.m************************
   function [val]=yhRn(n,htype,k,R)
% function yhRn calculates the radial dependant part of M: Rn(1,2)=Nn*hn(1,2)(kn*Rn)
% type = 1 2 or 3, see besselj function for more details
N=Nn(n);
kR=k.*R;
if htype==3
   val=N.*sbesselj(n,kR);
else
```

```
   val=N.*sbesselh(n,htype,kR);
end
return

**************************yhIn.m*****************
function [val]=yhIn(n,htype,k,R)
% function yhIn calculates the radial dependant part of N:
% Nn[h(n-1)(kR)-nhn(kR)/kR]
% htype = 1, 2 or 3
% see besselj function for more details
N=Nn(n);
kR=k.*R;
if htype==3
    hnm1=sbesselj(n-1,kR);
    hn=sbesselj(n,kR);
else
    hnm1=sbesselh(n-1,htype,kR);
    hn=sbesselh(n,htype,kR);
end
val=N*(hnm1-n*hn/(kR));
return

**************************sbesselj.m****************
function [jn,ierr] = sbesselj(n,kr)
% sbesselj - spherical bessel function jn(kr)
%
% jn(kr) = sqrt(pi/2kr) Jn+0.5(kr)
%
% See besselj for more details

[jn,ierr] = besselj(n+1/2,kr);
jn = sqrt(pi./(2*kr)) .* jn;

return

****************************sbesselh.m****************
function [hn,ierr] = sbesselh(n,htype,kr)
```

```
% sbesselh - spherical hankel function hn(kr)
% Usage:
% hn = sbesselh(n,htype,kr)
% hn(kr) = sqrt(pi/2kr) Hn+0.5(kr)
% See besselh for more details
[hn,ierr] = besselh(n+1/2,htype,kr);
hn = sqrt(pi./(2*kr)) .* hn;
return


**********Nn.m******************
function [val] = Nn (n)
% function Nn calculates the normalization factor as shown below:

val = 1/(sqrt(n*(n+1)));

return

**********yhreturnind.m*****************
function [val] = yhreturnind(vec,scalar)
% function returnind returns the row number where the code finds the
% matching wavelength

%input: vec - searching range
%       scalar - target

len = length(vec);
for ind=1:len
    if vec(ind) == scalar
        val = ind;
        return
    end
end
val = 0;
return
```

Appendix C

Modeling in COMSOL v3.5a

COMSOL Multiphysics is a finite-element based simulation environment that integrates geometry construction, meshing, physics definition, solving and visualization of post-processed results. Simulating optical properties of multilayer nanoshells is achieved by using the '*Scattered harmonic propagation*' mode in the '*RF Module*', shown in Fig. C.1. The following sections will go through necessary steps to simulate multilayer nanoshells in COMSOL.

C.1 Geometry definition

The simulation geometry is composed of six layers of half spherical domains, shown in Fig. C.2. The outmost perfect-matched layer (PML) absorbs waves that are scattered from the non-PML region and prevents the waves from reflecting back to the simulation space. The addition of a PML layer makes the finite simulation space equivalent to a free-space domain. Although not dramatically affecting the overall simulation results, PML effectively reduces the dimension of a simulation space in order to achieve desired accuracy. A far-field transferring (FFT) boundary surface is used to integrate the light scattered around the particle. A symmetry plane is defined in the $x-z$ plane (the cutout plane shown in Fig. C.2) for an excitation wave linearly polarized along x (perpendicular to the cutout plane). The symmetry plane halves the simulation space and reduces the problem size and overall computation time.

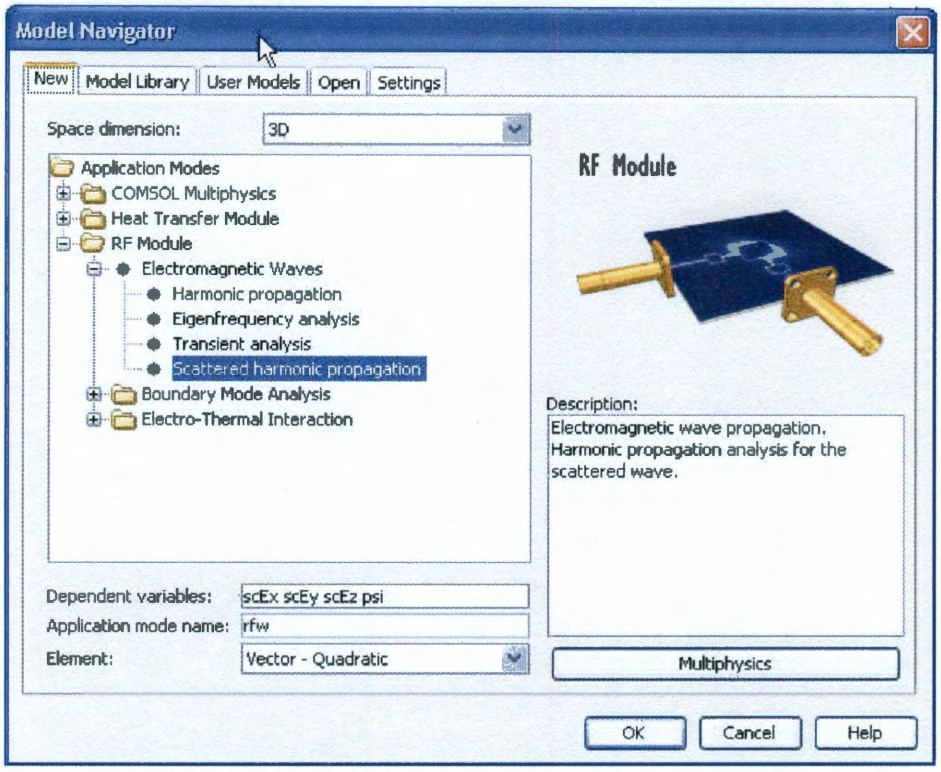

Figure C.1 :]
Radio frequency (RF) Module is used to simulate multilayer nanoshells.

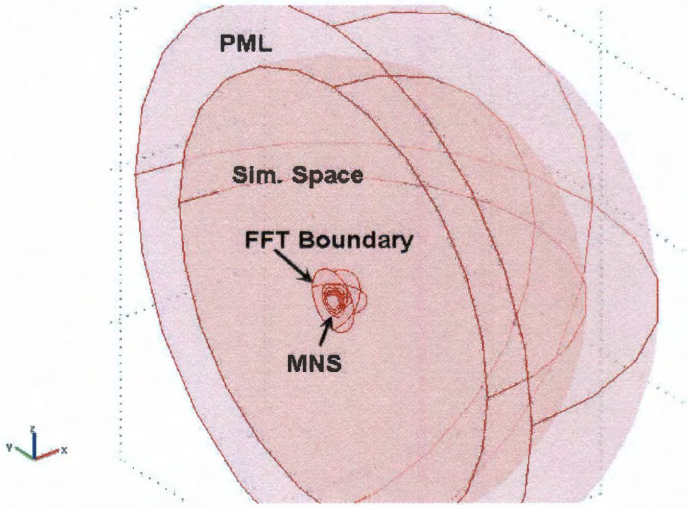

Figure C.2 : Simulation geometry

C.1.1 Boundary conditions

Boundary conditions govern how the electromagnetic wave changes its characteristic when entering one medium from another. Continuous boundary conditions (i.e., the tangential electric and magnetic field being continuous across the interface) are often imposed in source-free regions. In the COMSOL model, the outmost layer from PML needs to be terminated as a scattering boundary and far-field electric-field intensity E_{far} needs to be defined on the FFT boundary in order to facilitate the scattering calculation. In addition, symmetry planes need to be properly defined for the scattering calculation.

The boundary conditions can be set under '*Physics*'→'*Boundary Settings*', or by clicking the '$\partial\Omega$' icon in the toolbar. For the outer PML surface, once all contour surfaces are selected (control + click for multiple-surface selection), apply the following settings under the '*Conditions*' tab: boundary condition - scattering boundary condition; wave type - spherical wave; and $\mathbf{r_0}$ (source point) - (0,0,0). Similarly, for the symmetry plane at $x = 0$, set the boundary condition to perfect electric conductor (PEC). Conditions for rest of the layers are left at default settings (continuity).

For the FFT boundary, the far-field intensity E_{far} is defined under the '*Far-Field*' tab. Enter `Efar` into the name column and tab to automatically fill the '*Field*' and '*Normal derivative*' column. Since a symmetry plane is defined along $x = 0$, it is important check this symmetry in COMSOL in order to correctly account for the screening effect from charges on the opposite side of the hemisphere. To do this, under the '*Symmetry planes*', check '*x=0*' and select '*Symmetric H field (PEC)*'.

C.1.2 Subdomain settings

Subdomain settings specify the dielectric constant of the material in each region. Gold properties depend on the excitation energy and need to be imported into the material library in a tabulated form. For COMSOL v3.5a, an XML file is constructed in the following format:

```
<?xml version="1.0" encoding="UTF-8"?>
<lib type="class">
  <name>Johnson and Christy Gold Wavelength</name>
  <version type="class">
    <name>COMSOL 3.5</name>
    <ext>a</ext>
  </version>
  <mat type="array">
    <object type="class">
      <name>Gold Wvlength</name>
      <variables type="class">
        <sigma>2*pi*epsilon0_rfw*nu_rfw*jcEpsImag(nu_rfw)</sigma>
        <epsilonr>jcEpsReal(nu_rfw)</epsilonr>
      </variables>
      <functions type="array">
        <object type="class">
          <type>interp</type>
          <name>jcEpsReal</name>
          <method>linear</method>
          <extmethod>NaN</extmethod>
          <x type="stringarray">
->           {"1.4989623E+014","1.4997121E+014",...,"1.9853805E+015","1.9986164E+015"}
          </x>
          <data type="stringarray">
->            {"-201.8559","-201.6343",...,"6.9204","7.5489"}
          </data>
        </object>
        <object type="class">
          <type>interp</type>
          <name>jcEpsImag</name>
```

```
          <method>linear</method>
          <extmethod>NaN</extmethod>
          <x type="stringarray">
->            {"1.4989623E+014","1.4997121E+014",...,"1.9853805E+015","1.9986164E+015"}
          </x>
          <data type="stringarray">
->            {"28.7522","28.691",...,"25.8172","27.6258"}
          </data>
        </object>
      </functions>
    </object>
  </mat>
</lib>
```

The four lines noted by -> in the file with '...' are abbreviated from the full list of, in order, the excitation frequency in Hz, the corresponding real part of the dielectric constant, the excitation frequency in Hz (same as before), and the imaginary part of the corresponding dielectric constant. The dielectric constants of gold are first obtained from Johnson and Christy [Johnson & Christy, 1972] and then interpolated using cubic splines at finer intervals. To import the XML file, click '*Options*'→'*Materials/Coefficients Library*'. In the pop-up window, click '*Add libraries*', browse to the directory in which the XML file is stored and import the file. Now a new properties file named '*Johnson and Christy Gold Wavelength*' will appear in the materials library.

To define subdomain properties, click '*Physics*'→'*Subdomain Settings*'. Select subdomains in the left box of the prompted window and specify the dielectric constant (relative permitivity, ϵ_r) under the '*Physics*' tab on the right. For gold layers, import the library just created by clicking the '*Load*' button. Lastly, the subdomain that contains the PML layers needs to be set up under the '*PML*' tab. Select the outmost

subdomain, under the '*PML*' tab, set the '*Type of PML*' to spherical.

C.1.3 Scalar variables and Properties

The properties under '*Physics*'→'*Scalar Variables*' can generally be left unchanged except when the surrounding medium of the particle is non-air. For instance, to properly simulate multilayer nanoshells in water, the wave number needs to be scaled by the refractive index of water. To do this, modify the wave number `k` in the electric field expression `E = exp(-jkz)`. For an excitation wave linearly polarized along x and traveling in z in water, change the expression of `E0ix_rfw` to `exp(-j*k0_rfw*1.33*z)`.

Recall that the gold properties are tabulated with respect to excitation frequency. In order to simulate the geometry at different wavelength, one needs to set '*Specify wave using*' to '*freespace wavelength*' under '*Physics*'→'*Properties*'.

C.2 Meshing

C.2.1 Customized meshing

Quality of the mesh affects the convergence of iterative methods (it does not affect the solution when direct methods such as PARDISO are used). With multilayer nanoshells, areas where mesh quality can greatly influence simulation results are the metal-dielectric interfaces. Thus, it is recommended that the maximum meshing size on those surfaces to be relatively fine (i.e., smaller than 1/5 of the radius of the sphere).

Mesh quality is controlled under '*Mesh*'→'*Free Mesh Parameters*'. In the '*Global*' tab, check '*Custom mesh size*', and specify a '*Maximum element size*', typically 1/5 of the shortest simulation wavelength (i.e., `80 nm`). Then go to the '*Boundary*' tab, select

contour surfaces of each metal-dielectic interface, set a proper '*Maximum element size*' and growth factor (i.e., `1.3`). The growth factor determines the rate at which the mesh size changes from being coarse to fine. A higher growth factor will generate fewer meshes. In the '*Method*' box, pick either '*Triangle*' or '*Triangle(advancing front)*'. The latter method generates meshes from the boundary and progressively advances across the entire surface. This method often creates meshes of higher quality. For offset multilayer nanoshells, the meshes can be refined in the small gap along the offset direction. This is achieved by going to the '*Point*' tab and specify the maximum element size and growth rate for the two end points of the gap.

C.2.2 Mesh visualization

Mesh quality can be visualized under '*Mesh*'→'*Mesh Visualization Parameters*'. Make sure '*Subdomain elements*' is selected. Under '*Element color*', select '*Quality*'. Deselect '*Boundary elements*'. The '*Element selection*' allows one to visualize only part of the entire geometry (i.e., $z > 0$). Due to the large number of meshes generated, a better visualization is achieved by selectively display a fraction of all the meshes. This can be achieved by specifying '*Fraction of elements to plot*' under '*Element fraction*' (i.e., 0.01). Two types of useful '*Select elements*' to plot are elements '*With worst quality*' (Fig. C.3a) and '*Randomly*' (Fig. C.3b). Another useful tool is '*Mesh statistics*'; it displays the total number of elements and the minimum mesh quality. In general, the minimum quality should be above 0.1.

The quality of each tetrahedron is displayed by a parameter q that describes how regular the shape of the tetrahedron is:

$$q = \frac{72\sqrt{3}V}{(h_1^2 + h_2^2 + h_3^2 + h_4^2 + h_5^2 + h_6^2)^{3/2}} \tag{C.1}$$

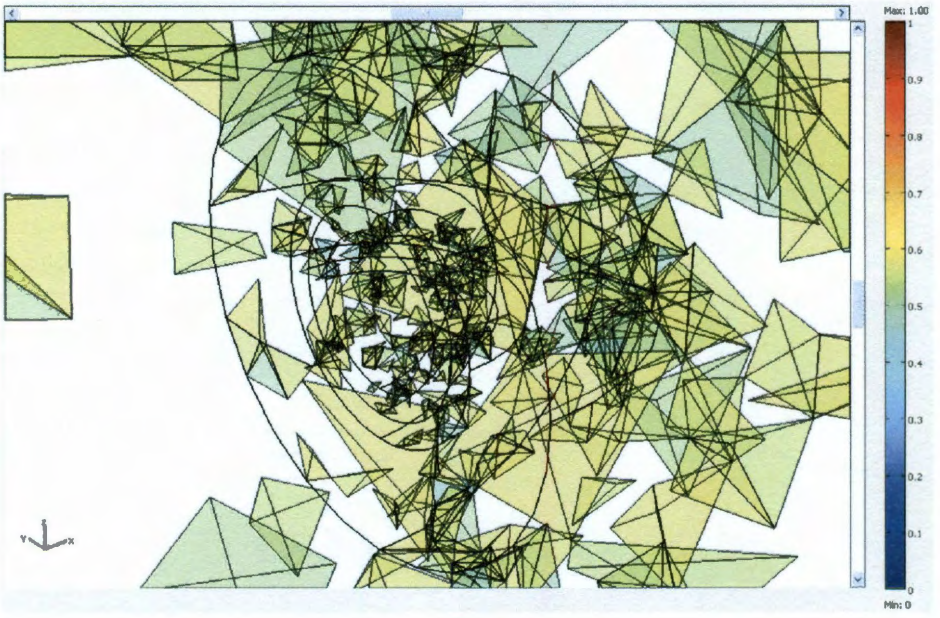

(a) Elements with worst quality

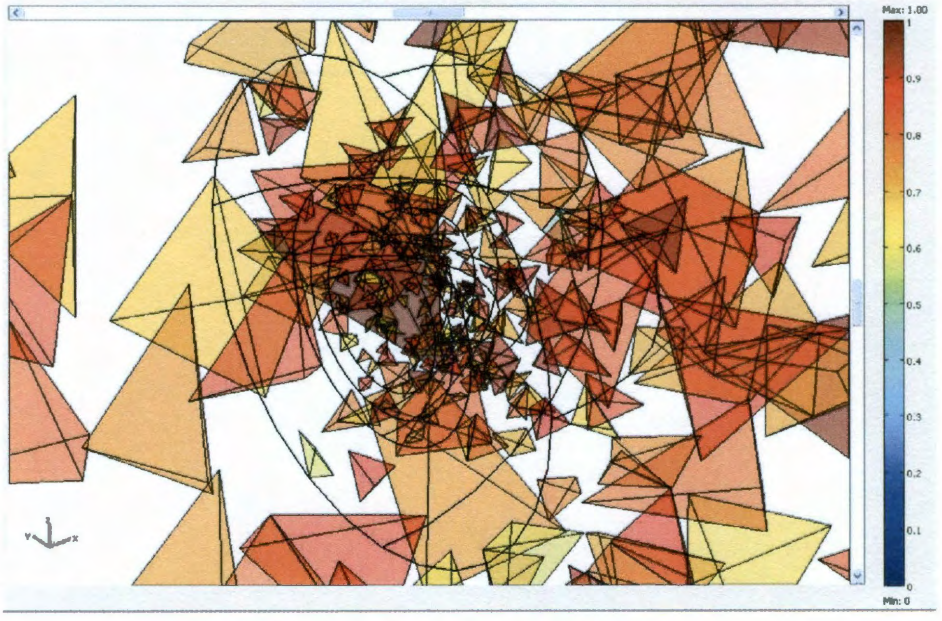

(b) Randomly displayed mesh quality

Figure C.3 : Visualization of mesh quality in and around a multilayer nanoshell. Red is better. 1.5% of all the meshes displayed.

where V is the volume of the tetrahedron and h's are the associated edge lengths. For a regular tetrahedron, $q = 1$ (i.e., the maximum value on the scale bars in Fig. C.3). Poorly shaped tetrahedra (i.e., with $q < 0.1$) will slow down the convergence or cause the convergence to fail. Fig. C.3)a demonstrates that the meshes of poorest quality in the region of interest have q values greater than 0.4; and Fig. C.3)b confirms that good mesh quality is achieved. In general, the lowest mesh quality should stay above 0.2 and arbitrarily refining meshes does not necessarily result in improvement in mesh quality.

C.3 Solving

C.3.1 Solver parameters

It is often desirable to perform a series of simulations of the same geometry at different excitation wavelengths. COMSOL v3.5 provides a parametric solving feature that can be accessed under '*Solve*'→'*Solver Parameters*'→'*Parametric*'(in the left box). Under the '*General*' tab, type `lambda0_rfw` in the '*Parameter name*' box. For a simulation at wavelengths from 500 to 900 nm with a 10 nm increment, for instance, enter `range(5.0e-7,1.0e-8,9.0e-7)` into the '*Parameter values*' box.

C.3.2 Solver methods

Two common linear system solvers of choice are Direct(PARDISO) and GMRES(with geometric multigrid preconditioner). PARDISO enjoys the advantage of being a direct solver. It is often the quickest as PARDISO does not have convergence issues as in iterative methods, such as GMRES. The drawback is that PARDISO demands large physical memories for large-scale matrix operations. The solver is best suited for

small geometries with fewer than 10k degrees of freedom. For intermediate and large geometries, however, the solver fails when the system runs out of memory. This can be circumvented by running COMSOL geometry files in batch mode on large computing clusters with distributed memory. GMRES, in contrary, is more memory efficient. The method iterates till a desired convergence criterion is achieved. The rate at which the results converge is greatly affected by the mesh quality as previously described.

C.3.3 Absorption and scattering calculation

Calculating scattering and absorption of the multilayer nanoshell requires defining two integration variables prior to solving the problem. For scattering efficiency calculation, go to '*Options*'→ '*Integration Coupling Variables*' →'*Boundary Variables*', select all contour surfaces on the FFT surface, type `sca` in the '*Name*' box and enter into the '*Expression*' box: `2*normEfar^2/ (x^2+y^2+z^2)/(pi*(r^2))`, where `r` is the outer radius of the nanoshells, in the unit of m. A factor of `2` is added to take into account scattering from the other half of the sphere.

For absorption efficiency, go to '*Options*'→ '*Integration Coupling Variables*' → '*Subdomain Variables*', select the gold core and gold shell, type `abs` in the '*Name*' box and `2*Qav_rfw*2*sqrt(mu0_rfw/epsilon0_rfw)/(rn*pi*(50e-9)^2)` in the '*Expression*' box, in which `rn` should be replaced by the refractive index of the surrounding medium (i.e., 1.33 for water). After all parameters have been properly defined, select '*Solve*'→'*Solve Problems*' or click the '=' sign on the toolbar to start the simulation.

C.3.4 Runing COMSOL in batch mode on Unix

To run COMSOL in batch mode on Unix, generate a file named 'script.sh':

```
#!/bin/bash
#PBS -l nodes=1:ppn=8
#PBS -l walltime=23:59:59
#PBS -j oe
#PBS -o /shared.scratch/yh4/
#PBS -M yh4@rice.edu
#PBS -m bae
#PBS -V
#PBS -e /shared.scratch/yh4

/opt/apps/comsol/3.5a/bin/comsol -np 8 -64 batch  -input /shared.scratch/yh4/file.mph
> /shared.scratch/yh4/file.mph.status
```

In this file, a wall time of 23 hrs 59 mins and 59 secs is requested for one computing node with eight processors. On the *SUGAR* cluster at Rice Shared Computing Grid, this command allocates two quad-core Intel Xeon processors running at 2.83GHz with a total of 32 GB RAM. The output file is stored under a user direction (yh4) on a scratch patch. The last two lines instruct the system to run COMSOL in the 64-bit batch mode. The geometry file 'file.mph' will be 'filled' with results once the simulation is done. The status of the simulation is stored in file.mph.status and it can be viewed by issuing the *vi* command:

```
vi file.mph.status
```

To submit the job, simply type:

```
qsub file.mph
```

To monitor if the job has been successfully submitted, inquire with

```
qstat -u username
```

In case error occurs, the error file (.EO file) can be found in the same direction the geometry file is stored. To run a short task is a higher-priority interactive mode, add to the file:

```
#PBS -q interactive
```

The wall time needs to be adjusted to 29 mins 59 secs as this mode is intended for debugging and does not allow execution time longer than half an hour. In most cases, PARDISO can simulate one multilayer nanoshell geometry at one wavelength for less than two minutes.

C.4 Post processing

Post-processing feature in COMSOL provides a powerful visualization tool to display various parameters in different plotting formats. The plotting functions can be accessed under '*Postprocessing*'→'*Plot Parameters*'.

C.4.1 Slice plot

A slice plot displays a specified parameter on a pre-defined cross section. To plot the normalized electric field on an $x-y$ plane, go to the '*Slice*' tab, choose `Electric field, norm` in the '*Predefined quantities*' box, then specify the slice position to be `0` level in x, and y, and `1` level in z. By default, the plane will be positioned at $z = 0$. To move this plane up and down, type in the '*Vector with coordinates*' box the expression for the new location. In Fig C.4, the plane is placed at $z = 10nm$. The range of the electric field plot can be set by clicking the '*Range...*' button. Click '*OK*' to display the image.

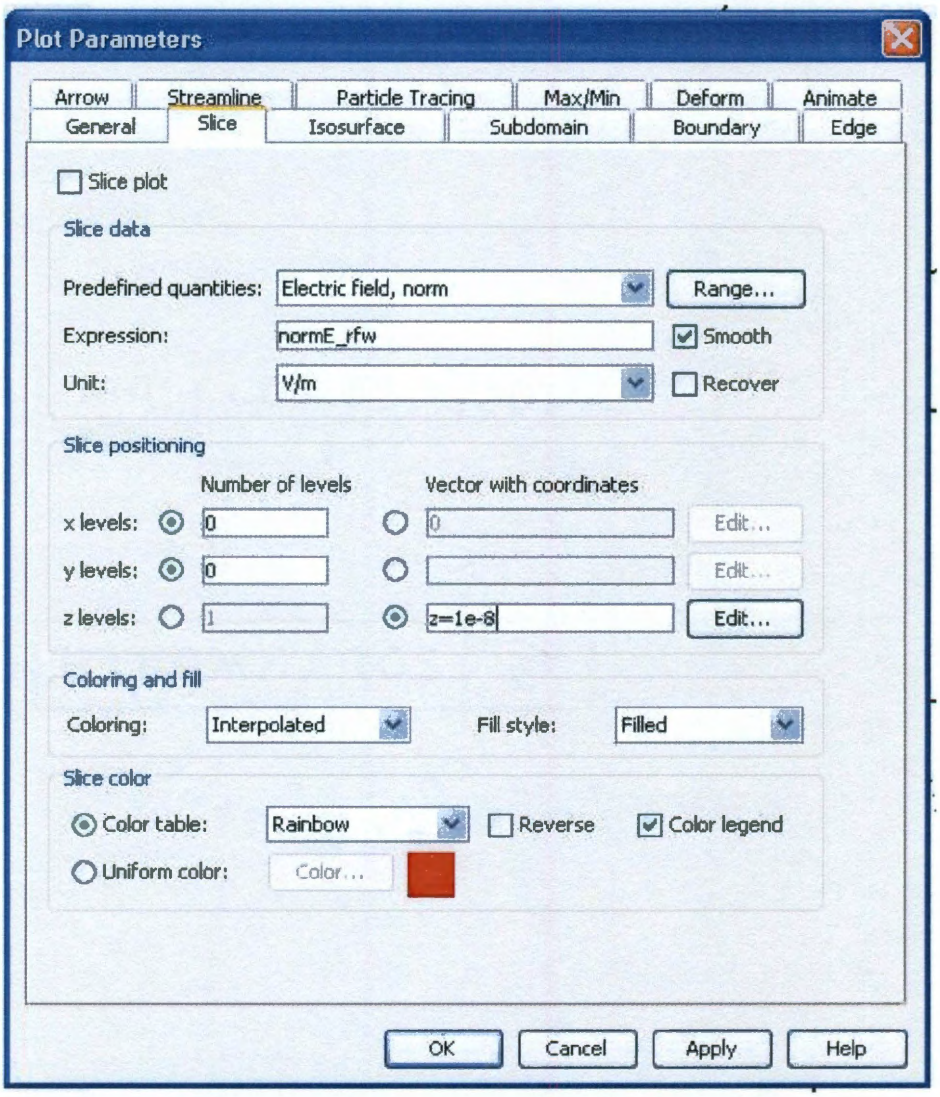

Figure C.4 : Slice plot settings.

C.4.2 Absorption and scattering efficiency plot

The absorption and scattering efficiencies have been defined in terms of global variables `abs` and `sca`, thus the calculation can be carried out by going to the '*Postprocessing*'→'*Global Variables Plot...*'. Type in the '*Expression*' box `abs`, then click > to the right of the box to add it to the '*Quantities to plot*' box. Repeat for `sca`, and use `abs+sca` for the extinction calculation. Select the wavelengths at which the results are to be plotted, the click '*OK*'. Results from the plot can be exported to an ascii file by clicking the $\frac{ASC}{||}$ icon on the toolbar of the plot.

C.4.3 Surface charge distribution

The surface charge σ is related to the electric field E by Gauss's law:

$$\epsilon_0 \iint \vec{E} \cdot \vec{n} dS = \iint \sigma dS \tag{C.2}$$

where $\vec{n}$ is the unit vector normal to an enclosed surface S. Surface charge distributions can be visualized by using the boundary plot. To plot surface charges on a particular metal-dielectric surface, first suppress all outer surfaces (i.e., scattering/PML surface, FFT boundary surface *etc.*). Go to '*Options*'→'*Suppress*'→'*Suppress Boundaries...*'. Select surfaces to be suppressed and click '*OK*'. Next, go to '*Postprocessing*'→' *Plot Parameters...*'→'*Boundary.* The divergence operation in Equation (C.2) is achieved by using the *up* and *down* operators in COMSOL. Type in the '*Expression*' box `(up(Ex)-down(Ex))*nx+(up(Ey)-down(Ey))*ny+(up(Ez)-down(Ez))*nz`.

Go to the '*General*' tab, , check the '*Boundary plot*' box and uncheck the '*Slice plot* box. Sweep the solution phase in the '*Solution at angle(phase)*' box till the magnitude of surface charges reaches its maximum (usually 90^o).

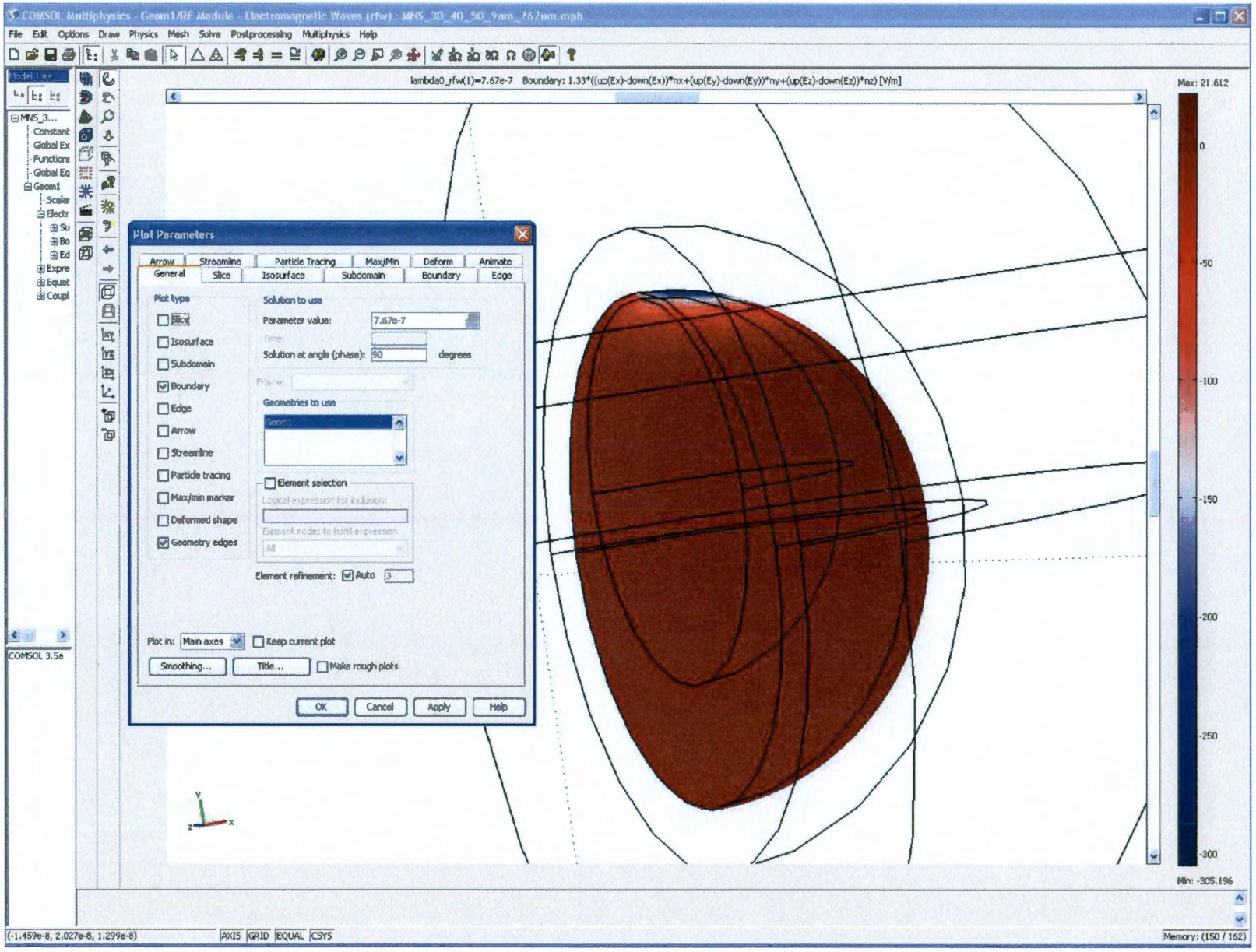

Figure C.5 : Surface charge distribution plot.

Bibliography

[Agrawal et al., 2006] Agrawal, A., Huang, S., Lin, A. W. H., Lee, M.-H., Barton, J. K., Drezek, R. A. & Pfefer, T. J. (2006). Journal of Biomedical Optics 11, 041121.

[Albert & Creighton, 1977] Albert, M. & Creighton, J. (1977). Journal of the American Chemical Society 99, 5215–5217.

[Ashkin et al., 1986] Ashkin, A., Dziedzic, J., Bjorkholm, J. & Chu, S. (1986). Optics Letters 11, 288–290.

[Averitt et al., 1997] Averitt, R., Sarkar, D. & Halas, N. (1997). Physical Review Letters 78, 4217–4220.

[Averitt et al., 1999] Averitt, R., Westcott, S. & Halas, N. (1999). Journal of the Optical Society of America B-Optical Physics 16, 1824–1832.

[Bao et al., 2008] Bao, F., Li, J.-F., Ren, B., Yao, J.-L., Gu, R.-A. & Tian, Z.-Q. (2008). Journal of Physical Chemistry C 112, 345–350.

[Bardhan et al., 2010] Bardhan, R., Mukherjee, S., Mirin, N. A., Levit, S. D., Nordlander, P. & Halas, N. J. (2010). Journal of Physical Chemistry C 114, 7378–7383.

[Berciaud et al., 2005a] Berciaud, S., Cognet, L., Tamarat, P. & Lounis, B. (2005a). Nano Letters 5, 515–518.

[Berciaud et al., 2005b] Berciaud, S., Cognet, L., Tamarat, P. & Lounis, B. (2005b). Nano Letters 5, 515–518.

[Bickford et al., 2008a] Bickford, L., Sun, J., Fu, K., Lewinski, N., Nammalvar, V., Chang, J. & Drezek, R. (2008a). Nanotechnology 19, 315102.

[Bickford et al., 2008b] Bickford, L. R., Chang, J., Fu, K., Sun, J., Hu, Y., Gobin, A., Yu, T.-K. & Drezek, R. A. (2008b). J. Nanobiotechnol. 4, 1–8.

[Bikram et al., 2007] Bikram, M., Gobin, A. M., Whitmire, R. E. & West, J. L. (2007). Journal of Controlled Release 123, 219–227.

[Bohren & Huffman, 1983] Bohren, C. F. & Huffman, D. R. (1983). Absorption and Scattering of Light by Small Particles. John Wiley and Sons : New York.

[Bora et al., 2010] Bora, M., Fasenfest, B. J., Behymer, E. M., Chang, A. S.-P., Nguyen, H. T., Britten, J. A., Larson, C. C., Chan, J. W., Miles, R. R. & Bond, T. C. (2010). Nano Letters 10, 2832–2837.

[Brandl et al., 2006] Brandl, D., Mirin, N. & Nordlander, P. (2006). Journal of Physical Chemistry B 110, 12302–12310.

[Brolo et al., 2004] Brolo, A., Arctander, E., Gordon, R., Leathem, B. & Kavanagh, K. (2004). Nano Letters 4, 2015–2018.

[Brousseau et al., 1999] Brousseau, L., Novak, J., Marinakos, S. & Feldheim, D. (1999). Advanced Materials 11, 447–449.

[C. V. Raman, 1928] C. V. Raman, K. S. K. (1928). Nature (London) 122.

[Cang et al., 2005] Cang, H., Sun, T., Li, Z., Chen, J., Wiley, B., Xia, Y. & Li, X. (2005). Optics Letters 30, 3048–3050.

[Chan et al., 2003] Chan, S., Kwon, S., Koo, T., Lee, L. & Berlin, A. (2003). Advanced Materials 15, 1595–1598.

[Chaney et al., 2005] Chaney, S., Shanmukh, S., Dluhy, R. & Zhao, Y. (2005). Applied Physics Letters 87, 031908.

[Chen et al., 2005a] Chen, K., Liu, Y., Ameer, G. & Backman, V. (2005a). Journal of Biomedical Optics 10.

[Chen et al., 2005b] Chen, K., Liu, Y., Ameer, G. & Backman, V. (2005b). J. Biomed. Opt. 10, 024005.

[Chen & Lazarides, 2009] Chen, S.-Y. & Lazarides, A. A. (2009). Journal of Physical Chemistry C 113, 12167–12175.

[Duan et al., 2006] Duan, G., Cai, W., Luo, Y., Li, Z. & Li, Y. (2006). Applied Physics Letters 89, 211905.

[Esenturk & Walker, 2009] Esenturk, E. N. & Walker, A. R. H. (2009). Journal of Raman Spectroscopy 40, 86–91.

[Fan & Zhao, 2008] Fan, J. G. & Zhao, Y. P. (2008). Langmuir 24, 14172–14175.

[Farsund & Felderhof, 1996] Farsund, O. & Felderhof, B. (1996). Physica a 227, 108–130.

[Fleischmann et al., 1974] Fleischmann, M., Hendra, P. & AJ, M. (1974). Chemical Physics Letters 26, 163–166.

[Frens, 1973] Frens, G. (1973). Nature Physical Science 241, 20–22.

[Fu et al., 2007] Fu, K., Sun, J., Lin, A. W. H., Wang, H., Halas, N. J. & Drezek, R. A. (2007). Current Nanoscience 3, 167–170.

[Galneder et al., 2001] Galneder, R., Kahl, V., Arbuzova, A., Rebecchi, M., Radler, J. & McLaughlin, S. (2001). Biophysical Journal 80, 2298–2309.

[Geissler et al., 2009] Geissler, M., Li, K., Cui, B., Clime, L. & Veres, T. (2009). Journal of Physical Chemistry C 113, 17296–17300.

[Gobin et al., 2007] Gobin, A. M., Lee, M. H., Halas, N. J., James, W. D., Drezek, R. A. & West, J. L. (2007). Nano Letters 7, 1929–1934.

[Gopinath et al., 2009a] Gopinath, A., Boriskina, S. V., Premasiri, W. R., Ziegler, L., Reinhard, B. M. & Dal Negro, L. (2009a). Nano Letters 9, 3922–3929.

[Gopinath et al., 2009b] Gopinath, A., Boriskina, S. V., Reinhard, B. M. & Dal Negro, L. (2009b). Optics Express 17, 3741–3753.

[Gouesbet & Grehan, 1982] Gouesbet, G. & Grehan, G. (1982). Journal of Optics-Nouvelle Revue D Optique 13, 97–103.

[Graf et al., 2003] Graf, C., Vossen, D., Imhof, A. & van Blaaderen, A. (2003). Langmuir 19, 6693–6700.

[Gulati et al., 2006] Gulati, A., Liao, H. & Hafner, J. H. (2006). Journal of Physical Chemistry B 110, 22323–22327.

[Gunawidjaja et al., 2009] Gunawidjaja, R., Kharlampieva, E., Choi, I. & Tsukruk, V. V. (2009). Small 5, 2460–2466.

[Gunawidjaja et al., 2008] Gunawidjaja, R., Peleshanko, S., Ko, H. & Tsukruk, V. V. (2008). Advanced Materials 20, 1544–1549.

[Han et al., 2008] Han, Y., Jiang, J., Lee, S. S. & Ying, J. Y. (2008). Langmuir 24, 5842–5848.

[Hao et al., 2007] Hao, F., Nehl, C. L., Hafner, J. H. & Nordlander, P. (2007). Nano Letters 7, 729–732.

[Hao & Nordlander, 2007] Hao, F. & Nordlander, P. (2007). Chemical Physics Letters 446, 115–118.

[Hao et al., 2009] Hao, F., Nordlander, P., Sonnefraud, Y., Van Dorpe, P. & Maier, S. A. (2009). ACS Nano 3, 643–652.

[Hao et al., 2008] Hao, F., Sonnefraud, Y., Van Dorpe, P., Maier, S. A., Halas, N. J. & Nordlander, P. (2008). Nano Letters 8, 3983–3988.

[Hirsch et al., 2006] Hirsch, L., Gobin, A., Lowery, A., Tam, F., Drezek, R., Halas, N. & West, J. (2006). Annals of Biomedical Engineering 34, 15–22.

[Hleb et al., 2008] Hleb, E. Y., Hu, Y., Drezek, R. A., Hafner, J. H. & Lapotko, D. O. (2008). Nanomedicine 3, 797–812.

[Hu et al., 2007] Hu, J.-W., Li, J.-F., Ren, B., Wu, D.-Y., Sun, S.-G. & Tian, Z.-Q. (2007). Journal of Physical Chemistry C 111, 1105–1112.

[Hu et al., 2008a] Hu, Y., Fleming, R. C. & Drezek, R. A. (2008a). Optics Express 16, 19579–19591.

[Hu et al., 2008b] Hu, Y., Nieminen, T. A., Bickford, L. R. & Drezek, R. A. (2008b). In OSA Biomedical Optics Topical Meeting.

[Hu et al., 2008c] Hu, Y., Nieminen, T. A., Heckenberg, N. R. & Rubinsztein-Dunlop, H. (2008c). J. Appl. Phys. 103, 093119.

[Hu et al., 2010] Hu, Y., Noelck, S. J. & Drezek, R. A. (2010). ACS Nano 4, 1521–1528.

[Hulteen et al., 1999] Hulteen, J., Treichel, D., Smith, M., Duval, M., Jensen, T. & Van Duyne, R. (1999). Journal of Physical Chemistry B 103, 3854–3863.

[Jackson & Halas, 2004] Jackson, J. & Halas, N. (2004). Proceedings of the National Academy of Sciences of the United States of America 101, 17930–17935.

[Jain & El-Sayed, 2007] Jain, P. K. & El-Sayed, M. A. (2007). Nano Letters 7, 2854–2858.

[Jain & El-Sayed, 2008] Jain, P. K. & El-Sayed, M. A. (2008). Journal of Physical Chemistry C 112, 4954–4960.

[Jain et al., 2007] Jain, P. K., Huang, W. & El-Sayed, M. A. (2007). Nano Letters 7, 2080–2088.

[Jain et al., 2006] Jain, P. K., Lee, K. S., El-Sayed, I. H. & El-Sayed, M. A. (2006). J. Phys. Chem. B 110, 7238–7248.

[Jeanmaire & Vanduyne, 1977] Jeanmaire, D. & Vanduyne, R. (1977). Journal of Electroanalytical Chemistry 84, 1–20.

[Johnson & Christy, 1972] Johnson, P. B. & Christy, R. W. (1972). Phys. Rev. B 6, 4370–4379.

[Jones et al., 2007] Jones, P. H., Marago, O. M. & Stride, E. P. J. (2007). Journal of Optics A-Pure and Applied Optics 9, S278–S283.

[Jordan et al., 2004] Jordan, P., Cooper, J., McNay, G., Docherty, F., Smith, W., Sinclair, G. & Padgett, M. (2004). Optics Letters 29, 2488–2490.

[Khlebtsov & Khlebtsov, 2006] Khlebtsov, B. & Khlebtsov, N. (2006). Journal of Biomedical Optics 11.

[Khlebtsov et al., 2007] Khlebtsov, B. N., Bogatyrev, V. A., Dykman, L. A. & Khlebtsov, N. G. (2007). Optics and Spectroscopy 102, 233–241.

[Khoury et al., 2009] Khoury, C. G., Norton, S. J. & Vo-Dinh, T. (2009). ACS Nano 3, 2776–2788.

[Khoury & Vo-Dinh, 2008] Khoury, C. G. & Vo-Dinh, T. (2008). Journal of Physical Chemistry C 112, 18849–18859.

[Kim et al., 2008] Kim, K., Lee, H. B., Lee, J. W., Park, H. K. & Shin, K. S. (2008). Langmuir 24, 7178–7183.

[Knight & Halas, 2008] Knight, M. W. & Halas, N. J. (2008). New Journal of Physics 10.

[Ko et al., 2008] Ko, H., Singamaneni, S. & Tsukruk, V. V. (2008). Small 4, 1576–1599.

[Ko & Tsukruk, 2008] Ko, H. & Tsukruk, V. V. (2008). Small 4, 1980–1984.

[Kobayashi et al., 2005] Kobayashi, Y., Katakami, H., Mine, E., Nagao, D., Konno, M. & Liz-Marzan, L. (2005). Journal of Colloid and Interface Science 283, 392–396.

[Kondo et al., 2009] Kondo, T., Nishio, K. & Masuda, H. (2009). Applied Physics Express 2.

[Kreibig & Vollmer, 1995] Kreibig, U. & Vollmer, M. (1995). Optical Properties of Metal Clusters. Springer.

[Landsman et al., 1976] Landsman, M., Kwant, G., Mook, G. & Zijlstra, W. (1976). Journal of Applied Physiology 40, 575–583.

[Lankers et al., 1997] Lankers, M., Khaled, E., Popp, J., Rossling, G., Stahl, H. & Kiefer, W. (1997). Applied Optics 36, 1638–1643.

[Larsson et al., 2007] Larsson, E. M., Alegret, J., Kall, M. & Sutherland, D. S. (2007). Nano Letters 7, 1256–1263.

[Lassiter et al., 2008a] Lassiter, J. B., Aizpurua, J., Hernandez, L. I., Brandl, D. W., Romero, I., Lal, S., Hafner, J. H., Nordlander, P. & Halas, N. J. (2008a). Nano Letters 8, 1212–1218.

[Lassiter et al., 2008b] Lassiter, J. B., Aizpurua, J., Hernandez, L. I., Brandl, D. W., Romero, I., Lal, S., Hafner, J. H., Nordlander, P. & Halas, N. J. (2008b). Nano Letters 8, 1212–1218.

[Lassiter et al., 2009] Lassiter, J. B., Knight, M. W., Mirin, N. A. & Halas, N. J. (2009). Nano Letters 9, 4326–4332.

[Lassiter et al., 2010] Lassiter, J. B., Sobhani, H., Fan, J. A., Kundu, J., Capasso, F., Nordander, P. & Halas, N. J. (2010). Nano Letters 10, 3184–3189.

[Le et al., 2005] Le, F., Lwin, N., Steele, J., Kall, M., Halas, N. & Nordlander, P. (2005). Nano Letters 5, 2009–2013.

[Le et al., 2007] Le, F., Lwin, N. Z., Halas, N. J. & Nordlander, P. (2007). Physical Review B 76.

[Lee et al., 2006] Lee, H. B., Yoo, Y. M. & Han, Y.-H. (2006). Scripta Materialia 55, 1127–1129.

[Lee et al., 2009] Lee, S., Mayer, K. M. & Hafner, J. H. (2009). Analytical Chemistry 81, 4450–4455.

[Liao et al., 2006] Liao, J., Bernard, L., Langer, M., Schonenberger, C. & Calame, M. (2006). Advanced Materials 18, 2444–2447.

[Lin et al., 2005a] Lin, A., Lewinski, N., West, J., Halas, N. & Drezek, R. (2005a). Journal of Biomedical Optics 10, 064035.

[Lin et al., 2005b] Lin, S., Li, M., Dujardin, E., Girard, C. & Mann, S. (2005b). Advanced Materials 17, 2553–2559.

[Linn et al., 2009] Linn, N. C., Sun, C.-H., Arya, A., Jiang, P. & Jiang, B. (2009). Nanotechnology 20.

[Liu et al., 2009] Liu, N., Langguth, L., Weiss, T., Kaestel, J., Fleischhauer, M., Pfau, T. & Giessen, H. (2009). Nature Materials 8, 758–762.

[Liu et al., 2010] Liu, N., Weiss, T., Mesch, M., Langguth, L., Eigenthaler, U., Hirscher, M., Sönnichsen, C. & Geissen, H. (2010). Nano Letters 10, 1103–1107.

[LizMarzan et al., 1996] LizMarzan, L., Giersig, M. & Mulvaney, P. (1996). Langmuir 12, 4329–4335.

[Lock, 2004a] Lock, J. (2004a). Applied Optics 43, 2532–2544.

[Lock, 2004b] Lock, J. (2004b). Applied Optics 43, 2545–2554.

[Lock et al., 2006] Lock, J., Wrbanek, S. & Weiland, K. (2006). Applied Optics 45, 3634–3645.

[Loo et al., 2005] Loo, C., Hirsch, L., Lee, M.-H., Chang, E., West, J., Halas, N. & Drezek, R. (2005). Opt Lett 30, 1012–1014.

[Lowery et al., 2006a] Lowery, A. R., Gobin, A. M., Day, E. S., Halas, N. J. & West, J. L. (2006a). International Journal of Nanomedicine 1, 149–154.

[Lowery et al., 2006b] Lowery, A. R., Gobin, A. M., Day, E. S., Halas, N. J. & West, J. L. (2006b). International Journal of Nanomedicine 1, 149–154.

[Lukianova-Hleb et al., 2010] Lukianova-Hleb, E., Hu, Y., Latterini, L., Tarpani, L., Lee, S., Drezek, R. A., Hafner, J. H. & Lapotko, D. O. (2010). ACS Nano 4, 2109–2123.

[Lukianova-Hleb & Lapotko, 2009] Lukianova-Hleb, E. Y. & Lapotko, D. O. (2009). Nano Letters 9, 2160–2166.

[Lynch & Hunter, 1985] Lynch, D. W. & Hunter, W. R. (1985). Comments on the Optical Constants of Metals and an Introduction to the Data for Several Metals: Handbook of Optical Constants of Solids. Academic Press.

[Mahan, 1990] Mahan, G. D. (1990). Many-Particle Physics. Springer: New York.

[Maheu et al., 1988] Maheu, B., Gouesbet, G. & Grehan, G. (1988). Journal of Optics-Nouvelle Revue D Optique 19, 59–67.

[Mazolli et al., 2003] Mazolli, A., Neto, P. & Nussenzveig, H. (2003). Proceedings of the Royal Society of London Series A-Mathematical Physical and Engineering Sciences 459, 3021–3041.

[Mie, 1908] Mie, G. (1908). Ann. d. Physik 25, 377–442.

[Moroz, 2008] Moroz, A. (2008). Journal of Physical Chemistry C 112, 10641–10652.

[Mukherjee et al., 2010] Mukherjee, S., Sobhani, H., Lassiter, J. B., Bardhan, R., Nordlander, P. & Halas, N. J. (2010). Nano Letters 10, 2694–2701.

[Nammalvar et al., 2007] Nammalvar, V., Wang, A. & Drezek, R. (2007). In Nanoscale imaging, spectroscopy, sensing and actuation for biomedical applications IV, Proceedings of SPIE, (Cartwright, A. N. & Nicolau, D. V., eds),.

[Nehl et al., 2004] Nehl, C., Grady, N., Goodrich, G., Tam, F., Halas, N. & Hafner, J. (2004). Nano Letters 4, 2355–2359.

[Nehl et al., 2006] Nehl, C., Liao, H. & Hafner, J. (2006). Nano Letters 6, 683–688.

[Nehl et al., 2004] Nehl, C. L., Grady, N. K., Goodrich, G. P., Tam, F., Halas, N. J. & Hafner, J. H. (2004). Nano Letters 4, 2355–2359.

[Neto & Nussenzveig, 2000] Neto, P. & Nussenzveig, H. (2000). Europhysics Letters 50, 702–708.

[Neves et al., 2006] Neves, A. A. R., Fontes, A., Pozzo, L. d. Y., de Thomaz, A. A., Chillce, E., Rodriguez, E., Barbosa, L. C. & Cesar, C. L. (2006). Optics Express 14, 13101–13106.

[Nie & Emery, 1997] Nie, S. & Emery, S. (1997). Science 275, 1102–1106.

[Nieminen et al., 2007] Nieminen, T. A., Loke, V. L. Y., Stilgoe, A. B., Knoener, G., Branczyk, A. M., Heckenberg, N. R. & Rubinsztein-Dunlop, H. (2007). Journal of Optics A-Pure and Applied Optics 9, S196–S203.

[Nordlander & Le, 2006] Nordlander, P. & Le, F. (2006). Applied Physics B-Lasers and Optics 84, 35–41.

[Nordlander et al., 2004] Nordlander, P., Oubre, C., Prodan, E., Li, K. & Stockman, M. (2004). Nano Letters 4, 899–903.

[Noziers & Pines, 1958] Noziers, P. & Pines, D. (1958). Physical Review 109, 741–761.

[Oldenburg et al., 1998] Oldenburg, S., Averitt, R., Westcott, S. & Halas, N. (1998). Chemical Physics Letters 288, 243–247.

[Oldenburg et al., 1999] Oldenburg, S., Jackson, J., Westcott, S. & Halas, N. (1999). Applied Physics Letters 75, 2897–2899.

[Pande et al., 2007] Pande, S., Ghosh, S. K., Praharaj, S., Panigrahi, S., Basu, S., Jana, S., Pal, A., Tsukuda, T. & Pal, T. (2007). Journal of Physical Chemistry C 111, 10806–10813.

[Park et al., 2008] Park, J., Estrada, A., Sharp, K., Sang, K., Schwartz, J. A., Smith, D. K., Coleman, C., Payne, J. D., Korgel, B. A., Dunn, A. K. & Tunnell, J. W. (2008). Optics Express 16, 1590–1599.

[Perner et al., 1997] Perner, M., Bost, P., Lemmer, U., vonPlessen, G., Feldmann, J., Becker, U., Mennig, M., Schmitt, M. & Schmidt, H. (1997). Physical Review Letters 78, 2192–2195.

[Pinchuk et al., 2004] Pinchuk, A., Kreibig, U. & Hilger, A. (2004). Surface Science 557, 269–280.

[Polavarapu & Xu, 2008] Polavarapu, L. & Xu, Q.-H. (2008). Langmuir 24, 10608–10611.

[Prodan & Nordlander, 2003] Prodan, E. & Nordlander, P. (2003). Nano Letters 3, 543–547.

[Prodan et al., 2003a] Prodan, E., Radloff, C., Halas, N. & Nordlander, P. (2003a). Science 302, 419–422.

[Prodan et al., 2003b] Prodan, E., Radloff, C., Halas, N. J. & Nordlander, P. (2003b). Science 302, 419–422.

[Qin et al., 2007] Qin, L., Banholzer, M. J., Millstone, J. E. & Mirkin, C. A. (2007). Nano Letters 7, 3849–3853.

[Qin et al., 2006] Qin, L., Zou, S., Xue, C., Atkinson, A., Schatz, G. C. & Mirkin, C. A. (2006). Proceedings of the National Academy of Sciences of the United States of America 103, 13300–13303.

[Radloff & Halas, 2004] Radloff, C. & Halas, N. (2004). Nano Letters 4, 1323–1327.

[Radloff, 2003] Radloff, C. J. (2003). Concentric nanoshells and plasmon hybridization. PhD thesis, Rice University.

[Reilly et al., 2007] Reilly, T. H., Chang, S.-H., Corbman, J. D., Schatz, G. C. & Rowlen, K. L. (2007). Journal of Physical Chemistry C 111, 1689–1694.

[Ren et al., 1996] Ren, K., Grehan, G. & Gouesbet, G. (1996). Applied Optics 35, 2702–2710.

[Ricardez-Vargas et al., 2005] Ricardez-Vargas, I., Iturbe-Castillo, M., Ramos-Garcia, R., Volke-Sepulveda, K. & Ruiz-Cortes, V. (2005). Optics Express 13, 968–976.

[Rivas et al., 2000] Rivas, L., Sanchez-Cortes, S., Garcia-Ramos, J. & Morcillo, G. (2000). Langmuir 16, 9722–9728.

[Ruan et al., 2007] Ruan, C., Eres, G., Wang, W., Zhang, Z. & Gu, B. (2007). Langmuir 23, 5757–5760.

[Rycenga et al., 2009] Rycenga, M., Hou, K. K., Cobley, C. M., Schwartz, A. G., Camargo, P. H. C. & Xia, Y. (2009). Physical Chemistry Chemical Physics 11, 5903–5908.

[Sealy, 2006] Sealy, C. (2006). Nano Today 1, 13.

[Shamsaie et al., 2007] Shamsaie, A., Jonczyk, M., Sturgis, J., Robinson, J. P. & Irudayaraj, J. (2007). Journal of Biomedical Optics 12.

[Smythe et al., 2009] Smythe, E. J., Dickey, M. D., Bao, J., Whitesides, G. M. & Capasso, F. (2009). Nano Letters 9, 1132–1138.

[Srivastava & Lee, 2006] Srivastava, D. & Lee, I. (2006). Advanced Materials 18, 2471–2475.

[T. A. Nieminen & Rubinsztein-Dunlop, 2007] T. A. Nieminen, G. Knöner, N. R. H. & Rubinsztein-Dunlop, H. (2007). aser Manipulation of Cells and Tissues, Methods in Cell Biology, vol. 82,. Elsevier: New York.

[Tessier et al., 2000] Tessier, P., Velev, O., Kalambur, A., Rabolt, J., Lenhoff, A. & Kaler, E. (2000). Journal of the American Chemical Society 122, 9554–9555.

[Tsukruk et al., 1997] Tsukruk, V., Bliznyuk, V., Visser, D., Campbell, A., Bunning, T. & Adams, W. (1997). Macromolecules 30, 6615–6625.

[van de Hulst, 1981] van de Hulst, H. C. (1981). Light Scattering by Small Particles. Dover Publications.

[van Dijk et al., 2006] van Dijk, M. A., Tchebotareva, A. L., Orrit, M., Lippitz, M., Berciaud, S., Lasne, D., Cognet, L. & Lounis, B. (2006). Physical Chemistry Chemical Physics 8, 3486–3495.

[Voarino et al., 2006] Voarino, P., Zerrad, M., Deumie, C. & Amra, C. (2006). Applied Optics 45, 1469–1477.

[Wang et al., 2006a] Wang, H., Brandl, D., Le, F., Nordlander, P. & Halas, N. (2006a). Nano Letters 6, 827–832.

[Wang et al., 2006b] Wang, H., Brandl, D., Le, F., Nordlander, P. & Halas, N. (2006b). Nano Letters 6, 827–832.

[Wang et al., 2006c] Wang, H., Fu, K., Drezek, R. A. & Halas, N. J. (2006c). Applied Physics B-Lasers and Optics 84, 191–195.

[Wang & Halas, 2008] Wang, H. & Halas, N. J. (2008). Advanced Materials 20, 820–825.

[Wang et al., 2005] Wang, H., Levin, C. & Halas, N. (2005). Journal of the American Chemical Society 127, 14992–14993.

[Wang et al., 2006] Wang, H., Wu, Y., Lassiter, B., Nehl, C. L., Hafner, J. H., Nordlander, P. & Halas, N. J. (2006). Proceedings of the National Academy of Sciences of the United States of America 103, 10856–10860.

[Wang et al., 2005] Wang, S., Yan, J. & Chen, L. (2005). Materials Letters 59, 1383–1386.

[Wang et al., 2008] Wang, Y., Qian, W., Tan, Y. & Ding, S. (2008). Biosens Bioelectron 23, 1166–1170.

[Weissleder, 2001] Weissleder, R. (2001). Nature Biotechnology 19, 316–317.

[Westcott et al., 1998] Westcott, S., Oldenburg, S., Lee, T. & Halas, N. (1998). Langmuir 14, 5396–5401.

[Wiley et al., 2007] Wiley, B. J., Chen, Y., McLellan, J. M., Xiong, Y., Li, Z.-Y., Ginger, D. & Xia, Y. (2007). Nano Letters 7, 1032–1036.

[Wu & Liu, 2009] Wu, D. J. & Liu, X. J. (2009). Applied Physics B-Lasers and Optics 97, 193–197.

[Wu & Nordlander, 2006] Wu, Y. & Nordlander, P. (2006). Journal of Chemical Physics 125.

[Xia et al., 2006] Xia, X., Liu, Y., Backman, V. & Ameer, G. A. (2006). Nanotechnology 17, 5435–5440.

[Yan et al., 2009] Yan, B., Thubagere, A., Premasiri, W. R., Ziegler, L. D., Dal Negro, L. & Reinhard, B. M. (2009). ACS Nano 3, 1190–1202.

[Yang et al., 2007] Yang, Y., Shi, J., Tanaka, T. & Nogami, M. (2007). Langmuir 23, 12042–12047.

[Zeman et al., 1987] Zeman, E., Carron, K., Schatz, G. & Van Duyne, R. (1987). Journal of Chemical Physics 87, 4189–4200.

[Zeng et al., 2007] Zeng, J., Huang, J., Lu, W., Wang, X., Wang, B., Zhang, S. & Hou, J. (2007). Advanced Materials 19, 2172–2176.

[Zhang et al., 2009] Zhang, Z., Weber-Bargioni, A., Wu, S. W., Dhuey, S., Cabrini, S. & Schuck, P. J. (2009). Nano Letters 9, 4505–4509.

[Zuloaga et al., 2010] Zuloaga, J., Prodan, E. & Nordlander, P. (2010). ACS Nano 4, 5269–5276.